

Shear Rheology of Nanoconfined Liquids

A Thesis

Submitted in partial fulfillment of the requirements for

the degree of

Doctor of Philosophy

by

Amandeep

20123227



Indian Institute of Science Education and Research

Pune - 411 008

2018

Certificate

Certified that the work incorporated in this thesis entitled **Shear Rheology of Nanoconfined Liquids** submitted by **Amandeep**, was carried out by the candidate, under my supervision. The work presented here or any part of it has not been included in any other thesis submitted previously for the award of any degree or diploma from any other University or institution.

Date : 11/05/2018

Dr. Shivprasad Patil

Thesis Supervisor

Indian Institute of Science Education and Research,

Pune, Maharashtra

Declaration

I declare that this thesis is a presentation of my original research work. Wherever contributions of others are involved, every effort is made to indicate this clearly, with due reference to the literature, and acknowledgment of collaborative research and discussions. I also declare that I have adhered to all principles of academic honesty and integrity and have not misrepresented or fabricated or falsified any idea/data/fact/source in my submission. I understand that violation of the above will be cause for disciplinary action by the Institute and can also evoke penal action from the sources which have thus not been properly cited or from whom proper permission has not been taken when needed.

Amandeep

Date : 11/05/2018

Roll No. 20123227

To,
Dad and Mom

Abstract

Flow properties of confined liquids play crucial roles in a wide range of areas from biology to nanofluidics. Liquids, when confined between two surfaces that are tens of nanometers apart, exhibit unique structural, dynamic, and mechanical properties, which are significantly different from those observed in bulk. In the past, shear measurement of confined liquids by different techniques are made up to shear rates $\leq 10^5 \text{ s}^{-1}$. We have developed an experimental scheme, which has two key advantages over previous techniques used to measure shear-viscosity for liquid films with thickness of few nanometers; (i) the spring measuring the viscous drag has very high stiffness (55000 N/m), and yet force sensitivity of few nN, thus reducing the thermal noise in our measurement. (ii) the force sensing spring stays out of the liquid, and hence has a high resonance frequency and quality factor, allowing us to perform off-resonance measurements with high shear frequency (5-20 kHz) and shear rates $\geq 10^5 \text{ s}^{-1}$. Using this novel shear rheometer, we investigated the role of confinement and substrate wettability on flow properties of polar (water) and non-polar (organic) liquids on several surfaces. We observed reduction in dissipation coefficient under confinement; which is modeled with Carreau-Yasuda model of shear thinning including finite slippage. We found that for purely wetting substrate the nonlinear rheological response solely originates due to nano-confinement, whereas both wettability and confinement play crucial role in case of non-wetting substrates. Finite Element Method (FEM) simulations were performed to understand the behavior of two prongs of our force sensor (tuning fork) at off resonance frequency in air and in liquid medium. Our study helps to separate out the effects of substrate wettability and confinement on shear resistance experienced by liquids at nano-confinement. The rheological response of nano-confined liquids is intriguing and we propose that it is result of criticality with respect to degree of confinement.

Acknowledgments

First of all, I would like to especially thank my Supervisor Dr. Shivprasad Patil for his patience and liberal nature which helped me in learning and doing instrumentation. I also would like to thank him for the freedom and independence that he provided in the lab and work. I also highly appreciate the IISER environment, which is quite vibrant. It not only helped academically but socially in growing my personality.

I would like to thank my Research committee members Dr. Arijit Bhattacharyay and Dr. Umakant Rapol for their critical input which helped in deeply analyzing and improving the quality of research work.

Reaching to the results, interpretations, and conclusions that culminated into this 'FAT Document' would not have been possible without the help and a great amount of environmental support from my lab mates, friends and family. The present and past members of the group have contributed immensely to my personal and professional time. I express my gratitude to Dr. AVR Murthy my P.hD senior in the lab who introduced or explained me about almost all instruments in a lab. I enjoyed working with him and liked his way of explanation by stating examples. Special thanks go to Ajith who helped me with electronic circuits, and LabVIEW programming for my home built experimental setup. I thoroughly enjoyed the camaraderie of my other labmates; Shatruhan, Surya, Saurabh Talele, Dr. Arpita Roychoudhary, Dr. Monica Raina, Vikhyat, Jyoti, Mayank and Umashankar for keeping the lab jolly and lively.

This thesis would not have come up to a happy ending without their support and enjoyment. I really enjoyed every moment spent with them. I miss cooking parties at NCRA with Naren and co. and at IUCAA with Mayukh in the company of my special friend Sayan. I enjoyed and missed the aerobic classes, jogging endeavor in the early morning, swimming and evenings spent at the IISER gym with my good friends Himani, Gunjan, Nishtha, and Jyoti. I gratefully acknowledge enthusiasm of Sayan, Naren, Doda, Prasun Da, Gunjan for making our many trekking experiences memorable. I am at a loss for words to express my gratitude to Sayan for all his support through thick and thin. I always enjoyed having an extensive discussion with him about the scientific problem, and it also helped me to be

always motivated for doing science. I would like to thank all staffs of academic, non-academic and technical departments at IISER Pune for their support.

Lastly, I want to thank my parents for their unconditional love, encouragement and most importantly patience during all these years. Without their relentless effort in raising me and supporting me in choosing science as a career, this thesis would not have been possible.

Amandeep

IISER Pune

Contents

Contents.....	vii
Acronyms and Abbreviations.....	x
Synopsis	1
Introduction	1
Motivation and Specific Goals	1
Conclusions and Future Prospective.....	4
Chapter 1	6
1.1 Water	8
1.1.1 Structure of water.....	8
1.1.2 Properties of water	8
1.1.3 Phase diagram.....	9
1.2 Interfacial and confined water.....	9
1.2.1 Presence of confined water in various areas.....	10
1.3 Organic Liquids.....	12
1.3.1 Enhanced Oil Recovery	12
1.3.2 Lubricants.....	13
1.4 Techniques to Measure flow Properties at Nanoscale	13
1.4.1 Flow at nanoscale.....	13
1.4.2 Stress-Strain nanoscale	14
1.4.3 Our Home- built Instrument	19
Chapter 2	7
2.1 Details of Instrument	28
2.1.1 Tuning fork, the Force Sensor	28
2.1.2 Fibre Tip	29
2.1.3 Mechanical Excitation of the Tuning fork	29
2.1.4 Electrical Circuit of Tuning fork.....	30
2.1.5 Calibration of oscillation amplitudes	31
2.1.6 X-Y-Z Positioner	32
2.2 Electronics.....	33
2.2.1 Electronics Circuits	33
2.2.2 Pre-amplifier	34
2.2.3 High Voltage operational amplifier.....	34

2.2.4 Proportional Integrator (PI) Feedback	35
2.2.5 Data Acquisition card (DAQ (6259))	36
2.2.6 Lock-in Amplifier	37
2.3 Operational details of Instrument	37
2.3.1 Automation using LabVIEW	38
2.4 Measurement Methodology	39
2.4.1 Determination of oscillation amplitude from a current value	40
2.4.2 Determination of dissipation coefficient from amplitude and phase	41
2.4.3 Relative change in dissipation coefficient	43
2.5 Validity of Measurement Methodology	44
Chapter 3	47
3.1 Introduction	47
3.2 Method	49
3.2.1 The instrument	49
3.2.2 Models	50
3.2.3 Sample preparation	51
3.3 Results	52
3.4 Discussions	55
3.5 Conclusions	57
Chapter 4	47
4.1 Introduction	60
4.2 Materials and Methods	61
4.3 Models	63
4.3.1 Finite slippage	63
4.3.2 Carreau-Yasuda Shear thinning model	63
4.3.2 Combined shear thinning with finite slippage	64
4.4 Results	64
4.5 Discussion	67
Chapter 5	74
5.1 Introduction	74
5.2 Theory	75
5.2.1 Piezoelectric module	75
5.2.2 Acoustic-piezoelectric interaction module	77
5.3 Results	77

5.3.1 Diether Piezo.....	77
5.3.2 Tuning fork with diether piezo.....	78
5.3.3 Optical fiber attached to tuning fork assembly	80
5.3.4 Simulation of a probe assembly in liquid.....	82
5.4 Conclusion.....	85
Chapter 6	89
6.1 Conclusions	89
6.2 Future Outlook.....	90
6.2.1 Integration with Fluorescence correlation spectroscopy	91
6.2.2 Integration with Raman spectroscopy	91

Acronyms and Abbreviations

SA_AFM	-	Small amplitude atomic force microscopy
SFA	-	Surface force apparatus
AFM	-	Atomic force microscope
TFM	-	Transverse force microscope
Tf- SFM	-	Tuning fork based shear force microscope
FCS	-	Fluorescence correlation spectroscopy
FM-AFM	-	Frequency modulation atomic force microscopy
PSD	-	Phase sensitive detector
EOR	-	Enhanced oil recovery
OMCTS	-	Octamethylcyclotetrasiloxane
TEHOS	-	Tetrakis (2-ethylhexoxyl) silane
FEM	-	Finite element method
SiC	-	Silicon carbide
Al ₂ O ₃	-	Aluminium oxide
LaO	-	Lanthanum oxide
SiH	-	Hydrogen terminated silicon
nm	-	nanometers
Mpa	-	Megapascals
D _a	-	Axial diffusion
W _A	-	Liquid substrate adhesion energy
X ₀	-	Drive amplitude
ω	-	Oscillation frequency
α	-	Piezoelectric coupling coefficient
τ	-	Relaxation time

Synopsis

Introduction

As far as we know, the existence of life on earth planet is not possible without water, the molecule of life. One of NASA guiding policies for the presence of life on any planet is to “follow the water”¹. Water is a V-shaped molecule, composed of two hydrogen atoms and one oxygen atom. The permanent dipole moment of water molecule plays a crucial role in its unique properties such as; high boiling and freezing point, and a large number of critical points in the phase diagram. High freezing and boiling temperature make it an ideal liquid for the existence of ecosystem. On the other side, the presence of many critical points reveals the complex nature of the simplest triatomic molecule in nature. At a fundamental level, the existence of any form of life is all about the molecular processes such as DNA replication, transcription into mRNA, and finally translation into specific proteins that happen inside the live cell. All these chemical reactions are facilitated by water molecules that are confined within few tens of nanometres. There exist fundamental questions regarding the nature and dynamics of water confined in live cells and similar small dimension. (i) Does intracellular water behave more or less like bulk water or not? (ii) How does dynamic nature of these water molecules help biomolecules (DNA, RNA, and proteins) to attain particular structure in fractions of a second, in spite of the presence of a considerable number of degrees of freedoms? Other than interfacial water, extraction of natural oils is another critical area where the flow of nanoconfined liquids gains significance.

In the oil industry, understanding of dynamics at nano-confinement plays a crucial role while extracting natural gas and oil from sub-surface. At present, recovery rates for oil extraction lie, at best, in the range of 30-45 % after application of primary and secondary extraction techniques. Thus, there is a requirement for further development in technology to elevate the existing recovery rates of natural oil^{2,3}. At the bottom of this technological problem is a sound understanding of flow response of oil molecules in porous and confined geometry in comparison to bulk.

Motivation and Specific Goals

Flow properties of confined liquids are traditionally measured by employing two methods; (i) flow measurement through nanochannels, and (ii) performing the shear measurement.

Measuring flow through hydrophobic nanochannels, researchers have reported enhancement in the outward flux of liquid by orders of magnitude higher than predicted according to fluid flow theory⁴. It has been reported that the viscosity of liquid flowing through the hydrophilic channel is 30% larger than that of bulk water⁵. On the other hand, measurement of the shear response of confined polar and non-polar liquids using surface force apparatus (SFA) and atomic force microscope (AFM) has led to contradictory findings⁶⁻¹⁰. SFA measurements have reported that a hydrogen-bonded liquid like water shows no appreciable change in viscosity upon confinement down to 4 nm and below^{7,10}. However, several other reports about the shear viscosity of nanoconfined water using SFA and AFM have reported an increase in viscosity by orders of magnitude at nano-confinement^{11,12}.

Nanoconfined thin films of non-associative fluids such as Octamethylcyclotetrasiloxane (OMCTS) exhibit significant nonlinear effects in their viscosity measurements¹¹. The normal stiffness measurement of both water and OMCTS layers under confinement show a speed dependent dynamic solidification^{13,14}. According to these measurements, the relaxation time of ordered liquid layers is 6-7 orders of magnitude higher than that of bulk liquid. Shear measurements using AFM have claimed that confined water shows nonlinear viscoelasticity. In both SFA and AFM experiments the shear frequency is limited from a few Hz to 1 kHz. To measure the change in relaxation time at confinement, we need a broader range of applied shear frequencies, typically larger than the inverse of the system's relaxation time. Also, jump-to-contact instability of the confining surfaces is a severe issue of controlling the film thickness while applying shear strain on these films. There is a need for developing new techniques employing force sensor which have large normal stiffness to avoid the snap-in contact instability and can perform measurements in the broader shear frequency range with force sensitivity of the order of nN.

In chapter 2, we have built tuning fork based shear rheometer, where tuning fork acts as a force sensor. It is made up of quartz which is piezoelectric and has a high stiffness (10^5 N/m). Its piezoelectric nature enables us to have optical free detection for shear force sensor to measure the viscous drag of liquid. Current signal generated in tuning fork for mechanical deflection is measured using pre-amplifier and a lock-in amplifier. Measurement methodology was developed to estimate the change in oscillation amplitude of prong from the measured current signal. Dissipation coefficient was estimated from amplitude and a phase signal of tuning fork prong. Measurement methodology for evaluating dissipation

coefficient was validated by measuring the ratio of E_{loss} in two liquids of known viscosity value.

In chapter 3, with the help of our tuning fork based shear rheometer, we have performed dynamic shear measurement on water confined between a sharp tip and substrates of different wettability. We explain the experimental observation of a reduction in dissipation under confinement with the help of Carreau–Yasuda model of shear thinning and finite slippage at the boundary¹⁵. We found clear evidence for shear thinning along with finite slippage for both wetting as well as non-wetting substrates¹⁵. We have found that slip length increases for non-wetting substrates progressively with increase in contact angle (a measure of wettability). In contrast, the shear thinning time scale does not vary appreciably over five substrates with different degree of wettability. The developed method allows us to separate contributions arising out of surface wettability, and slowing down of molecular dynamics. These findings have relevance in understanding the flow in nanofluidics and explaining rapid transit of water through carbon nanotubes reported earlier^{4,16}.

In chapter 4, we measure the shear response of non-polar liquids such as OMCTS and TEHOS and compare it with that of polar liquid water under high shear rates (10^6 s^{-1}) by employing large shear frequencies within 10 kHz to 15 kHz, and small oscillation amplitude within 1 to 3 nm. To understand the effect of wettability of the substrate, liquids were chosen having different contact angle on a mica substrate. OMCTS has a contact angle 25° whereas TEHOS has a contact angle 35° . We estimated dissipation coefficient for these liquids under confinement from measured amplitude and phase signal. We observed that dissipation coefficient decreases for both polar and non-polar types of fluids. Again fitting with shear thinning including finite slippage could explain the dynamics found by fluids under confinement. In short, we proposed a model which could separate out the effect of substrate and confinement from the rheological response exhibited by fluid under confinement. We claim that if shear rates are larger than the inverse of the relaxation time of fluid under confinement with known wettability, our proposed model would be able to explain the dynamics of liquid irrespective of their chemical nature.

In chapter 5, Finite element method (FEM) or finite element analysis (FEA) is a numerical method to solve the general equation of motion required to understand the dynamics of any system in various areas, such as structural analysis, heat transfer analysis, and fluid dynamics. To analyze a system using FEM, it is subdivided into smaller simpler

parts, called finite elements. The simple equations that model these finite elements are then assembled into a larger system of equations that shapes the entire problem. FEM uses variational methods to approximate a solution by employing boundary conditions and also by minimizing an associated error function. In our study, FEM simulations were performed to understand the dynamics of our force sensor, tuning fork in different surrounding medium (air, water and organic liquid, such as paraffin oil). Frequency domain analyses were employed to probe the on-resonance and off-resonance response of the force sensor. We could find how the oscillation amplitude of our sensor and probe assembly, *i.e.* the tuning fork with a fiber tip attached to diether piezo varies with surrounding medium. These results directly support our measurement methodology developed to understand the experimental results on the viscous drag of confined liquids.

Conclusions and Future Prospective

In this work, we have developed independent measurement methodology, and built indigenously designed force sensor to measure drag force of the confined liquid at the off-resonance frequency. Using our home-built tuning fork based oscillatory shear Rheometer, we have measured dynamic properties of confined fluid, *i.e.*, dissipation coefficient. Very low drive amplitude ($< 1\text{nm}$) make our measurement to be in the linear regime, and high shear rate up to 10^4 - 10^6 s^{-1} ensures that our results capture non-Newtonian behaviour. Analysis of our experimental results with different shear-thinning models helped us to distinguish between the effect of confinement and that of substrate wettability on the rheological response exhibited by confined liquids.

In present work, the mechanical response of nanoconfined liquid was measured using a home-built dynamic shear-rheometer. To get direct information about the processes, which are responsible for showing non-Newtonian behavior for confined fluid at the nanoscale, the system needs to be probed optically along with mechanical measurement. There are various possible ways to implement optical access by integrating mechanical analysis with (i) Fluorescence correlation spectroscopy (ii) Raman spectroscopy. FCS is useful for measuring the diffusion coefficient of probe molecules immersed in a liquid of interest at nano-confinement. Raman spectroscopy is a valuable tool to probe the structural changes taking place at a molecular level giving rise to non-Newtonian behavior.

References

- (1) Ball, P. Life's Matrix: A Biography of Water. In *Life's Matrix: A Biography of Water*.
- (2) Thomas, S. Enhanced Oil Recovery - An Overview. *Oil Gas Sci. Technol. - Rev. l'IFP* **2008**, *63*, 9–19.
- (3) Lake, L. W. Enhanced Oil Recovery. In *Enhanced Oil Recovery*; Society of Petroleum Engineers, 2010; p 550.
- (4) Majumder, M.; Chopra, N.; Andrews, R.; Hinds, B. Enhanced Flow in Carbon Nanotubes. *Nature* **2005**, *438*, 44.
- (5) Tas, N. R.; Haneveld, J.; Jansen, H. V.; Elwenspoek, M.; van den Berg, A. Capillary Filling Speed of Water in Nanochannels. *Appl. Phys. Lett.* **2004**, *85*, 3274–3276.
- (6) Zhu, Y.; Granick, S. Rate-Dependent Slip of Newtonian Liquid at Smooth Surfaces. *Phys. Rev. Lett.* **2001**, *87*, 096105.
- (7) Raviv, U.; Laurat, P.; Klein, J. Fluidity of Water Confined to Subnanometre Films. *Nature* **2001**, *413*, 51–54.
- (8) Derjaguin, B. V.; Churaev, N. V. Structure of Water in Thin Layers. *Prog. Surf. Sci.* **1992**, *40*, 422–428.
- (9) Israelachvili, J. N. Measurement of the Viscosity of Liquids in Very Thin-Films. *J. Colloid Interf. Sci.* **1986**, *110*, 263–271.
- (10) Raviv, U.; Klein, J. Fluidity of Bound Hydration Layers. *Science* **2002**, *297*, 1540–1543.
- (11) Granick, S. Motions and Relaxations of Confined Liquids. *Science* **1991**, *253*, 1374–1379.
- (12) Li, T.-D.; Gao, J.; Szoszkiewicz, R.; Landman, U.; Riedo, E. Structured and Viscous Water in Subnanometer Gaps. *Phys. Rev. B* **2007**, *75*, 115415.
- (13) Patil, S.; Matei, G.; Oral, A.; Hoffmann, P. M. Solid or Liquid? Solidification of a Nanoconfined Liquid under Nonequilibrium Conditions. *Langmuir* **2006**, *22*, 6485–6488.
- (14) Khan, S. H.; Matei, G.; Patil, S.; Hoffmann, P. M. Dynamic Solidification in Nanoconfined Water Films. *Phys. Rev. Lett.* **2010**, *105*, 106101.
- (15) Sekhon, A.; Ajith, V. J.; Patil, S. The Effect of Boundary Slippage and Nonlinear Rheological Response on Flow of Nanoconfined Water. *J. Phys. Condens. Matter* **2017**, *29*, 205101.

- (16) Lee, B.; Baek, Y.; Lee, M.; Jeong, D. H.; Lee, H. H.; Yoon, J.; Kim, Y. H. A Carbon Nanotube Wall Membrane for Water Treatment. *Nat. Commun.* **2015**, *6*, 7109.

Chapter 1

Introduction

The existence of life is not possible without water. One of NASA guiding policies for the existence of life on any planet is to “follow the water”¹. At a fundamental level, survival of any form of life is all about the molecular processes such as DNA replication, transcription, and translation. Intracellular water molecules facilitate all these three chemical reactions. One of the prominent questions about the nature of water is does it behave more or less like bulk water or not at the confined space in a live cell.

Resources of energy are other crucial factors for sustaining life on earth. Other than, recently developed alternative energy sources, a majority of consumed energy by humankind is coming from naturally produced and stored coal and oil across the globe. Post World War II, the world economy was reorganized based on the discovery of vast amounts of crude oil reserve around the world, particularly in the Middle East². The critical process in an oil-dependent economy is the extraction of oil from micro-porous rocks in a cost-effective way. Crude oil is extracted from the ground. Then it is converted to diesel, ethane, fuel oils, gasoline, jet fuel, kerosene, benzene, and liquefied petroleum gas. At present, recovery rates lie, at best, in the range of 30-45 % after application of primary and secondary extraction techniques. The achievement of higher recovery fractions could ensure energy production for at least the upcoming decades even under the assumption of fast economic growth scenarios^{3,4}. Thus, understanding the flow properties of the liquid such as viscosity, diffusion at confinement is vital to answer some of the intriguing questions about the interaction between biological macromolecules inside a cell and for improving the technology of oil extraction.

In the present thesis, the flow properties of water and organic liquids (similar to oil) are studied in confined geometry. It is essential for developing empirical laws about the behaviour of fluid under nanoscale confinement and will be helpful in dictating how the dynamics of these liquids behave from that in bulk form.

1.1 Water

Water is known as a solvent for the existence of life. Cavendish and Lavoisier discovered its composition in 1781⁵. Later, this composition was confirmed in 1800 by John Ritter by producing hydrogen and oxygen from electrolysis of water. Brief details about the structure and properties of water are outlined below

1.1.1 Structure of water

Water is V-shaped molecule composed of two hydrogen atoms and one oxygen atom. Fig. 1.1 shows the structure of water molecule. Water has net dipole moment due to electronegative nature of oxygen atom. The electronegativity of oxygen is responsible for the hydrogen bonding network between water molecules. The existence of hydrogen bonding was first suggested by Wendell Latimer and Worth Rodebush in 1920^{6,7}. Hydrogen bonding is responsible for many of anomalies in the behaviour of water.

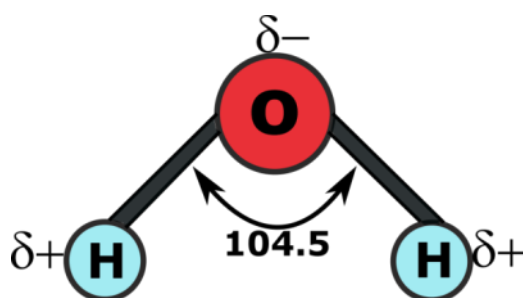


Fig. 1.1 Structure of water molecule

1.1.2 Properties of water

High boiling and freezing temperature: Water is a molecule with small molecular weight. Despite its small molecular weight, water has an incredibly high boiling temperature. The reason behind it is the network of hydrogen-bonded structure (intermolecular interaction). Breakage of hydrogen bonds requires higher energy, which in turn gives rise to high boiling temperature. One of the possible reasons for the existence of ecosystems in water is due to its high boiling and freezing temperature.

Water acts as a universal solvent: It can dissolve almost all substances as compared to other liquids, so it is known as universal solvent. The electronegative oxygen attracts the slightly positive charge of the substance, and electropositive hydrogen pulls the slightly negative charge in the compound. This phenomenon helps in dissociating of most of the substances in water.

Density of water: In general, the solid phase of any substance has a higher density than its liquid phase. But, in case of water, ice being the solid phase of water has a lower density than liquid form. This is possible, as hydrogen bonding poses a tetrahedral arrangement of water molecules in ice crystal which is less dense than random arrangement of water molecules in liquid phase.

1.1.3 Phase diagram

A phase diagram is a diagram for representation of physical states exhibited by substances at different values of temperature and pressure. Fig. 1.2 shows phase diagram of water. It shows that bulk water has many critical points. The critical point is a point in phase diagram corresponds to the existence of two phases at a particular value of temperature and pressure. It has minimum nine critical points^{8,9}. That is an indication of the complex nature of one of the simplest triatomic molecule in nature. Fig. 1.2 also shows the comparison of experimental phase diagram (panel a) of real bulk water, and theoretical predicted phase diagram (panel b) according to its low molecular weight.

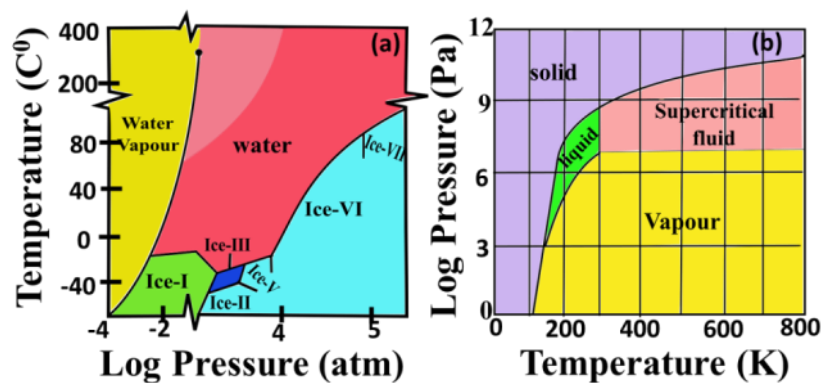


Fig. 1.2 (a) Phase diagram of bulk water showing minimum nine critical points with the representation of different phases of water, (b) theoretical predicted phase diagram of water. This figure is adapted with permission from Ref 9 copyright (2010), Springer Nature.

1.2 Interfacial and confined water

Surface boundaries and interfaces play a crucial role in determining the properties of liquid molecules. Water present near these surface boundaries and interfaces is known as interfacial water. One of the examples is that phase diagram of any liquid including water becomes complicated near any boundary¹⁰. The dynamics of fluid get dominant by its local properties due to the presence of interface or boundary around them¹⁰. To understand the interfacial

behavior of water or any other system, there is need to characterize these properties near surfaces as well in porous geometry. Flow properties such as viscosity and diffusion depend on various factors, such as; nature of the liquid-surface interaction, a roughness of wall, and shape and size of the pores. A possible way to get knowledge about these is to understand water density distribution near the surfaces or in micro-nano pores, which is crucial for their altered structural and flow response.

1.2.1 Presence of confined water in various areas

Water molecules, confined in tens of nanometers space is present very diverse areas from biology to nanofluidics. Understanding the flow properties at these nano-pores is highly relevant for the technological and biological field. Few of these areas are listed below:

Water Filtration

For water filtration, many processes take place which are disinfection, decontamination, desalination. All the methods require the removal of unnecessary by-products or pollutants¹¹. There is a requirement of membranes made up of material which are quite selective and efficient for the recovery of clean water. It has already been reported in literature¹²⁻¹⁵ that the carbon nanotubes having atomically smooth, hydrophobic walls responsible for the higher outward flux of water through the pores due to the existence of considerable, substantial slip length. Further measurements with these membranes reveal 90% rejection coefficients that match or exceed those of commercially available nanofiltration membranes while exceeding their flux by up to four times. It could be quite helpful if possible to design such kind of nanostructure or similar defect-free membrane at large scale which are specific and having the higher flux for water molecules only.

Interfacial Water in Biological Functions

Water acts as a primary solvent in all life processes. Initiation of various biochemical reactions inside living organisms requires critical hydration level. Few of them are cellular respiration, incorporation of CO₂ into amino and nucleotides (carbon fixation), synthesis of protein and RNA. In the vicinity of few hydration layers onset of various critical biochemical processes is seen¹⁶⁻²¹. Hydration layers of water molecules present around biomolecules is 3-4 molecular layers thick.

Another example is how protein folding-unfolding mechanism is affected by level of hydration²²⁻²⁴. Protein folding takes place very fast time scale than predicted by Levinthal paradox²⁵. One of the most probable reasons behind it is hydrophobic interaction^{26,27}. Water molecules play a significant role in defining the structure and function of the protein. Open questions exist regarding relative amount of hydration, and how water may be involved in solute distribution across cell membranes. No clear answer to these questions yet. All intracellular water molecules present around biomolecules and near cell membrane are termed as confined water.

Flow Sensor

Understanding flow properties of confined liquids find application in next-generation flow sensor²⁸. Measurement of these properties gives information about how the viscosity, diffusion of liquid changes at confinement in comparison to bulk dynamics. Ghosh et.al; have reported that flow of liquid in single-walled carbon nanotube bundles induces voltage along the direction of flow in an electrical circuit. They have also shown that the voltage induced depends on the polar nature and ionic conductivity of the liquid and flow velocity. These results indicate that by measuring the voltage produced due to liquid flow would provide information about polarity, ionic conductivity and flow properties of liquid.

Nanofluidics

Nanofluidic devices consist of multiple arrays of channels that are few nanometres in width and few micrometres in length for exquisite control of fluid flow. Nanofluidic arrays find application in separating out the molecules of interest from a mixture under the action of applied external forces such as pressure, potential and concentration gradients across nanochannels²⁹. The passage of solvent through these devices depends on hydrodynamic force, diffusion, migration, and friction with the wall of nanochannels. Understanding effect of these forces on flow properties through nanochannels have applications in the field of biomedical devices, such as transport in kidney³⁰, separation science^{31,32}, and membrane technology³³. Thus it is fundamentally essential to study the flow response of simple or complex fluids with varying degrees of confinement scale, chemical nature of boundaries; to understand and design nano-machines with complex transport phenomena. Fig. 1.3 represents few areas where presence of nanoconfined water plays critical role.

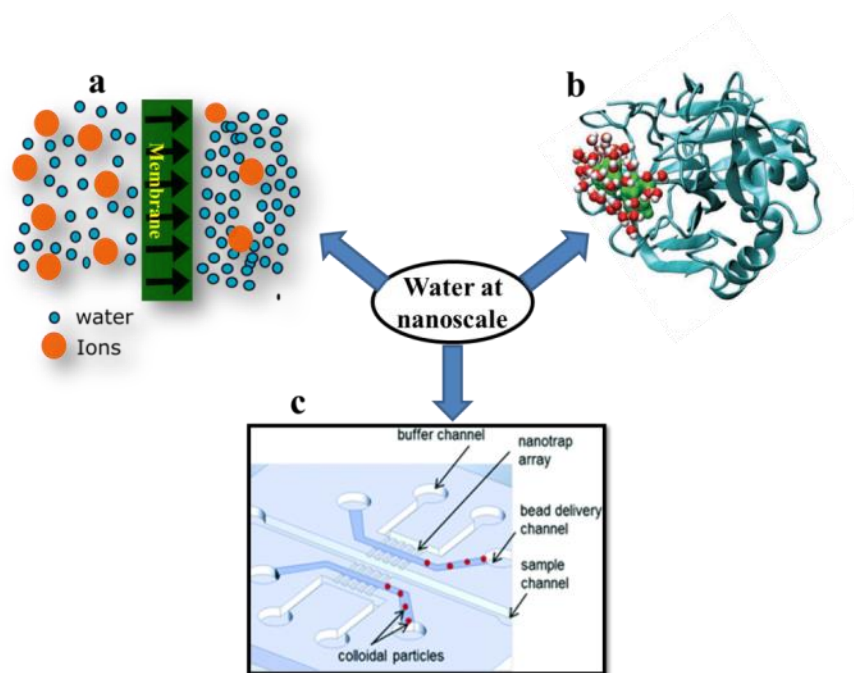


Fig. 1.3 Presence of confined water in different areas from biology to nanofluidics. (a) Desalination of water using filtration membrane (b) presence of water around biomolecule³⁴ (c) nanofluidics array for separation of an interested molecule³⁵. This figure is adapted with permission from Ref. 34, copyright (2008) American Association for Advancement of Science, Ref. 35, copyright (2014), Royal Society of Chemistry.

1.3 Organic Liquids

Organic liquids are mainly made of carbon and hydrogen atoms. There are two types of organic liquids; polar and non-polar types. These liquids act as a model system for oil molecules having applications in lubrication industry. Thus, understanding the flow properties of these liquids in confined pores could be helpful in areas such as; enhanced oil recovery field (EOR) and lubrication Industry. In present work, flow response of two organic liquid such as Octamethylcyclotetrasiloxane (OMCTS) and Tetrakis (2-ethylhexoxy)silane (TEHOS) was measured. These liquids are neutral, nonpolar and globular in shape.

1.3.1 Enhanced Oil Recovery

Oil and gas are significant resources of energy for sustaining life on earth. Other than, recently developed alternative energy sources, the majority of consumed energy by humankind is coming from naturally produced and stored coal and oil across the globe. However, most of these residual oils are 'trapped' in tiny micrometric pores of the reservoir rock which makes their efficient recovery to be difficult. At present, recovery rates lie, at

best, in the range of 30-45 % after application of primary and secondary extraction techniques. There is a need for development or improvement in existing technology which could achieve high recovery rate and assure the energy production for at least upcoming decades under the assumption of fast economic growth scenarios^{3,36}. It emerges the significant area of research which is based on studying the flow properties of oil or model system molecules at similar size micro or nano-pores.

1.3.2 Lubricants

For any molecules system to acts as a lubricant, it should have a low coefficient of friction at high normal pressure (MPa) and high shear rates (10^6 s^{-1}). The size of molecule also plays an important role to act as a better lubricant for next-generation nano-machines. To get an application in this area, it is essential to study the shear response of these liquids under high pressure and shear rates at confinement for designing next-generation novel lubricants.

1.4 Techniques to Measure flow Properties at Nanoscale

1.4.1 Flow at nanoscale

Flow properties of the fluid at nano-confinement can be measured by estimating the outward flux of liquid through nanochannels under the action of applied external forces such as pressure, potential and concentration gradients across nanochannels²⁹. Fig. 1.4 shows schematic for measuring flow properties of fluid by measuring flow response through nanochannels. Fluid properties such as viscosity, diffusion, and effect of substrate term of slip length³⁷ can be evaluated. The factors which govern the outward flux of liquid are diffusion along axial direction due to the external field across the channel (D_s), liquid substrate interaction (W_A), length to radius ratio^{38,39}. For the hydrophobic surface, D_s is high, and W_A is low giving rises to substantial enhancement in flow; for the hydrophilic surface, D_s is low, and W_A is high give rise to minimal flow rates. In past, researchers have reported about flux enhancement by 5-6 orders of magnitude for water molecules through hydrophobic carbon nanotube channels than predicted by fluid flow theory⁴⁰. For hydrophilic channels, it has been reported that the viscosity of liquid flowing through them is 30% larger than that of bulk water⁴¹.

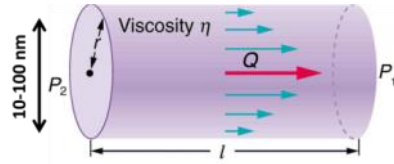


Fig. 1.4 Pictorial representation of the flow of liquid through a nanochannel. Properties of flowing liquid are measured by applying a pressure gradient across the channel. P, Q, l, and η represent pressure, flux, length of channel and viscosity respectively.

1.4.2 Stress-Strain nanoscale

Another way to measure the flow properties of the liquid at nano-confinement is by measuring stress-strain at nanoscale. In stress-strain measurement, one surface moves in a parallel or perpendicular direction to another surface with fluid placed between them, and the resulting stress is measured. The stress generated is generally measured by attaching a force sensor system with proper electronics and feedback mechanism to one of the sliding surfaces. The measured stress is related to the drag force experienced due to liquid molecules interactions with these two surfaces; hence drag force can be related to the viscosity of the confined liquid.

Rheometers are employed to apply oscillatory/steady strain to plate or sensor moving in liquid to measure its shear stress response. Parallel plate and cone-plate geometry rheometers are usually used. SFA⁴² and AFM⁴³ correspond to the category of these rheometers to measure shear stress at nanoscale. Fig. 1.5 shows the schematic of SFA and AFM. In these measurements, the sinusoidal strain (stress) is applied upper plate or cone of rheometer. Using the methodology of bulk rheometers, the resulting stress (strain) can be resolved into components that are in phase or $\pi/2$ out of phase to the input. From these data, a complex modulus or viscosity is determined as a function of shear rate or frequency. As given below:

$$G^* = G' + iG'' \quad \text{or} \quad \eta^* = G^*/i\omega \quad \text{-----} \quad \text{eqn (2.32)}$$

Where G' is storage modulus and G'' is loss modulus give information about energy storage and energy dissipation in flow respectively. For perfectly elastic solid, $G'' = 0$ and $G' = G^*$. For Newtonian liquid, $G' = 0$ and $\eta^* = G''/\omega$.

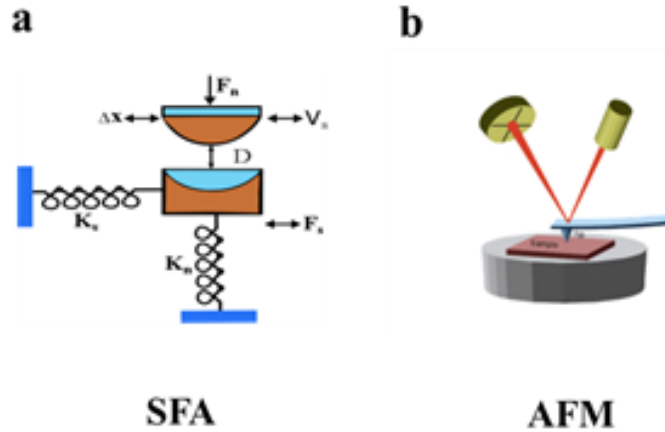


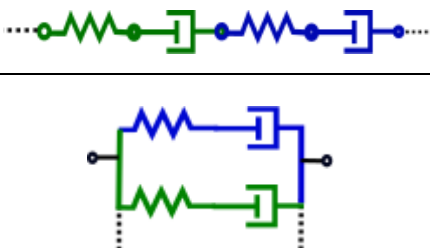


Fig. 1.5 Schematic of SFA and AFM employed to measure dynamics properties of the confined liquid by performing shear strain measurement. (a) measured the shear response of liquid confined between cross cylindrical plates and (b) between tip and substrate below.

Analysis about the dynamics of liquid at nanoscale is based on measuring the change in oscillation amplitude and phase of force sensor oscillating in liquid medium by varying the distance between two surfaces. If there is no phase lags between the input (strain) and the output signal (stress), it is known as Hookian solid. The pure spring system acts as analogy system for Hookian solid. If there is phase lag and it is 90 degrees, it is known as a Newtonian liquid. The simple dashpot system acts as an analogy for a Newtonian fluid. Other possibility is finite phase lag which lie between 0 and 90 degrees, it is known linear viscoelastic liquid (Non-Newtonian Liquid). This system can be described by the combination of spring and dashpot in series (Maxwell Model) or parallel configuration (Kelvin Model). But in all above configuration, the change in stress with stain or strain rate is linear. If there are liquids in which the change in stress is nonlinear with strain or strain rate, they are called nonlinear viscoelastic liquids (Shear-thinning, shear thickening). Shear thinning or shear thickening behaviour is exhibited by complex liquids those have a shear rate dependent viscosity such as mayonnaise, polymer melts, starch solution. Table 1.1 represents all these processes.

Table 1.1 It comprises all possible relation between stress and shear rate. Liquid behavior is categorized to Newtonian and non-Newtonian on the basis of stress and strain rate curve. Various combinations of spring and dashpot are considered to represent the behaviour of Newtonian and non-Newtonian fluids.

Stress Strain rate Relation	Behavior		Representation
Linear	Only Viscous	Newtonian Liquid	
	Viscous + elastic	Non Newtonian	
Non Linear	Viscous +Elastic	Non Newtonian (Shear Thinning Shear Thickening)	

Initially, all measurements were done mainly using SFA and AFM in normal mode to measure the response of nanoconfined water. These reports found slowdown dynamics⁴⁴⁻⁴⁶, presence⁴⁷⁻⁵⁰ or absence^{51,52} of hydration layers, dynamic solidification^{53,54}, and no change in viscosity at separation $d < 1\text{nm}$ ⁵¹. A lot of controversies exist regarding the behavior of nanoconfined water. To resolve it various researchers started addressing this question by performing measurement in shear mode. It was addressed using SFA, AFM and their modified instruments in shear mode. Researchers using SFA reported about the viscoelastic response exhibits by aqueous liquid⁵⁵. The shear response was measured by oscillating the one plate parallel to another plate in liquid medium with oscillation frequency $< 100\text{ Hz}$ and amplitude $0.1-10\text{ nm}$. Another report by Klein group reported no change in viscosity of water molecules below to one molecular layer⁵¹. They measured the viscosity by measuring the exclusion of water from the surfaces during the jump in contact. Around the same time, Antonozzi group⁵⁶ using novel fiber-based transverse shear force microscope (TFM) reported

about linear viscoelastic response and longest relaxation time around 1ms in comparison to bulk relaxation time (1ps). Other results by Granick group⁵⁷ states the change in dynamic properties of nanoconfined water versus the twist angle of substrates. They reported about the viscosity and relaxation time is oscillating with the twist angle of substrates. It signifies that at nano-confinement water behave as a viscoelastic liquid but enhancement in viscosity and relaxation time by orders of magnitude as compared to bulk. Reido group⁵⁸ reported the nonlinear viscoelastic response for nanoconfined water using AFM. They have reported shear rate dependent relaxation time. The change of viscosity of water due to surface wettability in addition to confinement distance is addressed. It is found out that the enhancement of lateral force on the nonwetting substrate is less in comparison to wetting substrate⁵⁹. The reason behind the reduction in lateral force is stated due to the existence of slip length⁶⁰. In the recent measurement, the researcher has reported about the nonlinear shear thinning behavior for bilayers of water molecules confined between substrates⁶¹. These are the different results in the literature about the dynamics exhibits by nanoconfined water.

Table 1.2 Summary of studies done in the past to measure flow properties of nanoconfined water in normal mode.

Instrument	Frequency (Hz)	Amplitude (A ⁰)	Approach rates (nm/s)	Conclusions	Ref.
SA-AFM	400	0.36	1	Highly Viscous	⁶²
SA-AFM	400 - 900	0.6 - 1.1	0.2 - 1.4	Dynamic solidification	⁵³
SFA	1 - 5	2000	0.03	No change in viscosity	⁵¹
SFA	-	-	-	Oscillatory force due to hydration layer	⁴⁷
Thermally excited AFM	-	-	0.4 - 1	Solvation forces	⁴⁸
Static AFM	-	-	5	No solvation forces	⁵²
Dynamic AFM	14000	12	-	Oscillatory forces	⁶³
Simulations	100	1 - 20	-	Viscosity increase by orders	⁶⁴
AFM	2000	1 - 30	0.2	Viscosity increase by orders	⁵⁹

Table 1.3 Summary of all published studies reporting on the measurement of the shear response of nanoconfined water in shear mode.

Instrument	Frequency (Hz)	Amplitude (nm)	Shear rates (s ⁻¹)	Conclusions	Ref.
SFA	100	0.1 - 10	10 - 10 ³	Linear viscoelastic	⁵⁵
SFA	1-5	200	10 ² - 10 ⁴	No change in viscosity	⁵¹
TFM	10,000	1 - 5	10 - 10 ⁴	Linear viscoelastic	⁵⁶
AFM	50 - 2000	0.06 - 3	1 - 10 ³	Nonlinear viscoelastic	⁶⁵
AFM	1000	0.9	1 - 10 ³	Enhancement in viscosity	⁶⁰
SA-AFM	1000 - 2000	0.2	10 ³	Dynamic solidification	⁵²
AFM	3000 - 30,000	0.06 - 0.25	10 ³ - 10 ⁶	Shear thinning	⁶⁶
Tf-SFM	1000 - 15,000	1 - 5	10 ² - 10 ⁶	Viscoelastic and Shear thinning	⁶⁷

Table 1.4 Summary of published reports on the measurement of the normal and shear response of nanoconfined organic liquids.

Organic Liquids	Instrument	Frequency (Hz)	Amplitude (nm)	Mode	Conclusions	Ref.
TEHOS	SA-AFM	< 2000	< 0.6	Normal	Non Newtonian behaviour	⁶⁸
OMCTS, Cyclohexane, Toluene	SFA	10		Normal	Solidification	⁶⁹
OMCTS	SFA	1-257	10 - 20	Oscillatory Shear	Phase transition, Slow relaxation time	^{70,71}
TEHOS	SA-AFM, FCS	465	34	Normal	Heterogeneous molecular mobility	⁷²
OMCTS	SFA+FCS	0.02-52		Normal, Steady shear	Slowdown in diffusion coefficient under normal mode, Diffusion coefficient changes by 2-3 factor under shear mode	^{73,74}
OMCTS	AFM			Oscillatory	Non-Newtonian	⁵⁸

				shear	behaviour	
OMCTS	SFA	5	10^5	Steady state shear	Non-Newtonian Behavior at high shear rate	⁷⁵
OMCTS, Dodecane	SFA	0.02- 52	$0.4- 6 \times 10^3$	oscillatory shear	Non-Newtonian, shear thinning	⁷⁶
OMCTS	SA-AFM	squeeze out	2	Normal	Dynamic solidification	⁵⁴
Dodecanol Hexane	FM-AFM	50,000	2.5	Normal mode	Crystalline nature with imaging the layered structure	⁷⁷
Hexadecane	FM-AFM	73,500	2.5	Oscillatory Shear	Slowdown dynamics	⁷⁸

Results tabulated in Table 1.2, 1.3 and 1.4 clearly demonstrate that several research groups have attempted to measure the viscoelastic response of nanoconfined water, and several organic liquids are employing different forms of SFA, AFM, and FCS spectroscopies. Despite all these studies, there is a lack of consensus regarding behavior of confined liquids at nano-confinement.

1.4.3 Our Home- built Instrument

In context of this, we have built a novel tuning fork based shear rheometer to shed more light into this area. In our instrument, the confinement of liquid takes place between the fibre tip attached to tuning fork and substrate below (See Chapter 2 for experimental details). Quartz tuning fork acts as force sensor. This experimental scheme has two advantages over previous techniques; (i) the sensor is made up of quartz material which is piezoelectric in nature, so all readouts are electrical no optical setup is required, (ii) spring measuring the viscous drag has high stiffness (55000 N/m) and yet has force sensitivity of few nN due to its piezoelectric nature. (iii) The force sensing spring is out of liquid and hence has a high resonance frequency and quality factor. This allows off-resonance measurement with high shear frequency (5-20 kHz) and shear rates ($10^4- 10^6 \text{ s}^{-1}$). This instrument enables us to measure the dynamics viscosity of nanoconfined liquid at range of shear frequencies and shear rates and could be able to capture non-Newtonian behaviour of nanoconfined liquid if any. Using this measurement technique, I have measured effect of nano-confinement and wettability on shear response of water and two organic liquids (Octamethylcyclotetrasiloxane (OMCTS) and Tetrakis (2-ethylhexoxyl) silane (TEHOS)).

References

- (1) Ball, P. Life's Matrix: A Biography of Water. In *Life's Matrix: A Biography of Water*.
- (2) Derksen, J. B. D.; Kendrick, J. W. *Productivity Trends in the United States*; 1961; Vol. 29.
- (3) Thomas, S. Enhanced Oil Recovery - An Overview. *Oil Gas Sci. Technol. - Rev. l'IFP* **2008**, *63*, 9–19.
- (4) Lake, L. W. Enhanced Oil Recovery. In *Enhanced Oil Recovery*; Society of Petroleum Engineers, 2010; p 550.
- (5) Cavendish, H. Three Papers, Containing Experiments on Factitious Air, by the Hon. Henry Cavendish, F. R. S. *Philos. Trans. R. Soc. London* **1766**, *56*, 141–184.
- (6) Pauling, L. The Nature of Chemical Bond. In *Cornell University Press*; Cornell University Press, 1948.
- (7) Latimer, W. M.; Rodebush, W. H. Polarity and Ionization from the Standpoint of the Lewis Theory of Valence. *J. Am. Chem. Soc.* **1920**, *42*, 1419–1433.
- (8) Sengers, J. V; Levelt Sengers, J. M. H. Thermodynamic Behavior of Fluids Near the Critical Point. *Annu. Rev. Phys. Chem.* **1986**, *37*, 189–222.
- (9) Dunaeva, A. N.; Antsyshkin, D. V.; Kuskov, O. L. Phase Diagram of H₂O: Thermodynamic Functions of the Phase Transitions of High-Pressure Ices. *Sol. Syst. Res.* **2010**, *44*, 202–222.
- (10) Brovchenko, I.; Oleinikova, A. Interfacial and Confined Water. In *Elsevier*; Elsevier, 2008; p 303.
- (11) Shannon, M. A.; Bohn, P. W.; Elimelech, M.; Georgiadis, J. G.; Mariñas, B. J.; Mayes, A. M. Science and Technology for Water Purification in the Coming Decades. *Nature* **2008**, *452*, 301–310.
- (12) Hummer, G.; Rasaiah, J. C.; Noworyta, J. P. Water Conduction through the Hydrophobic Channel of a Carbon Nanotube. *Nature* **2001**, *414*, 188–190.

- (13) Kalra, A.; Garde, S.; Hummer, G. Osmotic Water Transport through Carbon Nanotube Membranes. *Proc. Natl. Acad. Sci.* **2003**, *100*, 10175–10180.
- (14) Hinds, B. J.; Chopra, N.; Rantell, T.; Andrews, R.; Gavalas, V.; Leonidas G, B. Aligned Multiwalled Carbon Nanotube Membranes. *Science* **2004**, *303*, 62–65.
- (15) Holt, J. K. Fast Mass Transport Through Sub-2-Nanometer Carbon Nanotubes. *Science* **2006**, *312*, 1034–1037.
- (16) Clegg, J. S. Interrelationships between Water and Metabolism in Artemia Salina Cysts: Hydration-Dehydration from the Liquid and Vapour Phases. *J. Exp. Biol.* **1974**, *61*, 291–308.
- (17) Clegg, J. S. Interrelationships between Water and Metabolism in Artemia Cysts—II. Carbohydrates. *Comp. Biochem. Physiol. Part A Physiol.* **1976**, *53*, 83–87.
- (18) Clegg, J. S. Interrelationships between Water and Metabolism in Artemia Cysts—III. Respiration. *Comp. Biochem. Physiol. Part A Physiol.* **1976**, *53*, 89–93.
- (19) Clegg, J. S. Interrelationships between Water and Cellular Metabolism InArtemia Cysts. V.14CO₂ Incorporation. *J. Cell. Physiol.* **1976**, *89*, 369–380.
- (20) Clegg, J. S.; Cavagnaro, J. Interrelationships between Water and Cellular Metabolism InArtemia Cysts IV. Adenosine 5'-Triphosphate and Cyst Hydration. *J. Cell. Physiol.* **1976**, *88*, 159–166.
- (21) Clegg, J. S. Interrelationships between Water and Cellular Metabolism InArtemia Cysts. VI. RNA and Protein Synthesis. *J. Cell. Physiol.* **1977**, *91*, 143–154.
- (22) Riback, J. A.; Bowman, M. A.; Zmyslowski, A. M.; Knoverek, C. R.; Jumper, J. M.; Hinshaw, J. R.; Kaye, E. B.; Freed, K. F.; Clark, P. L.; Sosnick, T. R. Innovative Scattering Analysis Shows That Hydrophobic Disordered Proteins Are Expanded in Water. *Science* **2017**, *358*, 238–241.
- (23) Levy, Y.; Onuchic, J. N. Water and Proteins: A Love-Hate Relationship. *Proc. Natl. Acad. Sci.* **2004**, *101*, 3325–3326.
- (24) Papoian, G. A.; Ulander, J.; Eastwood, M. P.; Luthey-Schulten, Z.; Wolynes, P. G. From The Cover: Water in Protein Structure Prediction. *Proc. Natl. Acad. Sci.* **2004**,

- 101, 3352–3357.
- (25) Finkelstein, A. V.; Garbuzynskiy, S. O. Solution of Levinthal’s Paradox Is Possible at the Level of the Formation and Assembly of Protein Secondary Structures. *Biophysics (Oxf)*. **2016**, *61*, 1–5.
- (26) Harano, Y.; Kinoshita, M. Translational-Entropy Gain of Solvent upon Protein Folding. *Biophys. J.* **2005**, *89*, 2701–2710.
- (27) Kinoshita, M. Roles of Translational Motion of Water Molecules in Sustaining Life. *Front. Biosci.* **2009**, *Volume*, 3419.
- (28) Ghosh, S. Carbon Nanotube Flow Sensors. *Science* **2003**, *299*, 1042–1044.
- (29) Sparreboom, W.; Van Den Berg, A.; Eijkel, J. C. T. Principles and Applications of Nanofluidic Transport. *Nat. Nanotechnol.* **2009**, *4*, 713–720.
- (30) Deen, W. M. Hindered Transport of Large Molecules in Liquid-Filled Pores. *AIChE J.* **1987**, *33*, 1409–1425.
- (31) Prieve, D. C.; Hoysan, P. M. Role of Colloidal Forces in Hydrodynamic Chromatography. *J. Colloid Interface Sci.* **1978**, *64*, 201–213.
- (32) Ruckenstein, E.; Prieve, D. C. Adsorption and Desorption of Particles and Their Chromatographic Separation. *AIChE J.* **1976**, *22*, 276–283.
- (33) Bowen, W. R.; Mukhtar, H. Characterisation and Prediction of Separation Performance of Nanofiltration Membranes. *J. Memb. Sci.* **1996**, *112*, 263–274.
- (34) Granick, S.; Bae, S. C. A Curious Antipathy for Water. *Science* **2008**, *322*, 1477–1478.
- (35) Syed, A.; Mangano, L.; Mao, P.; Han, J.; Song, Y.-A. Creating Sub-50 Nm Nanofluidic Junctions in a PDMS Microchip via Self-Assembly Process of Colloidal Silica Beads for Electrokinetic Concentration of Biomolecules. *Lab Chip* **2014**, *14*, 4455–4460.
- (36) Rivet, S.; Lake, L. W.; Pope, G. A. A Coreflood Investigation of Low-Salinity Enhanced Oil Recovery. In *SPE Annual Technical Conference and Exhibition*; Society of Petroleum Engineers, 2010.

- (37) Thomas, J. A.; McGaughey, A. J. H.; Kuter-Arnebeck, O. Pressure-Driven Water Flow through Carbon Nanotubes: Insights from Molecular Dynamics Simulation. *Int. J. Therm. Sci.* **2010**, *49*, 281–289.
- (38) Secchi, E.; Marbach, S.; Niguès, A.; Stein, D.; Siria, A.; Bocquet, L. Massive Radius-Dependent Flow Slippage in Carbon Nanotubes. *Nature* **2016**, *537*, 210–213.
- (39) Chakraborty, S.; Kumar, H.; Dasgupta, C.; Maiti, P. K. Confined Water: Structure, Dynamics, and Thermodynamics. *Acc. Chem. Res.* **2017**, *50*, 2139–2146.
- (40) Majumder, M.; Chopra, N.; Andrews, R.; Hinds, B. Enhanced Flow in Carbon Nanotubes. *Nature* **2005**, *438*, 44.
- (41) Tas, N. R.; Haneveld, J.; Jansen, H. V.; Elwenspoek, M.; van den Berg, A. Capillary Filling Speed of Water in Nanochannels. *Appl. Phys. Lett.* **2004**, *85*, 3274–3276.
- (42) Winterton, R. H. S.; Tabor, D. The Direct Measurement of Normal and Retarded van Der Waals Forces. *Proc. R. Soc. A Math. Phys. Sci.* **1969**, *312*, 435–450.
- (43) Binnig, G.; Quate, C. F.; Gerber, C. Atomic Force Microscope. *Phys. Rev. Lett.* **1986**, *56*, 930–933.
- (44) Jeffery, S.; Hoffmann, P. M.; Pethica, J. B.; Ramanujan, C.; Özer, H. Ö.; Oral, A. Direct Measurement of Molecular Stiffness and Damping in Confined Water Layers. *Phys. Rev. B* **2004**, *70*, 054114.
- (45) Li, T.-D.; Gao, J.; Szoszkiewicz, R.; Landman, U.; Riedo, E. Structured and Viscous Water in Subnanometer Gaps. *Phys. Rev. B* **2007**, *75*, 115415.
- (46) Major, R. C.; Houston, J. E.; McGrath, M. J.; Siepmann, J. I.; Zhu, X.-Y. Viscous Water Meniscus under Nanoconfinement. *Phys. Rev. Lett.* **2006**, *96*, 177803.
- (47) Israelachvili, J. N.; Pashley, R. M. Molecular Layering of Water at Surfaces and Origin of Repulsive Hydration Forces. *Nature*. 1983, pp 249–250.
- (48) Cleveland, J. P.; Schäffer, T. E.; Hansma, P. K. Probing Oscillatory Hydration Potentials Using Thermal-Mechanical Noise in an Atomic-Force Microscope. *Phys. Rev. B* **1995**, *52*, 8692–8696.
- (49) Higgins, M. J.; Polcik, M.; Fukuma, T.; Sader, J. E.; Nakayama, Y.; Jarvis, S. P.

- Structured Water Layers Adjacent to Biological Membranes. *Biophys. J.* **2006**, *91*, 2532–2542.
- (50) Uchihashi, T.; Higgins, M.; Nakayama, Y.; Sader, J. E.; Jarvis, S. P. Quantitative Measurement of Solvation Shells Using Frequency Modulated Atomic Force Microscopy. *Nanotechnology* **2005**, *16*, S49–S53.
- (51) Raviv, U.; Laurat, P.; Klein, J. Fluidity of Water Confined to Subnanometre Films. *Nature* **2001**, *413*, 51–54.
- (52) O’Shea, S. J.; Welland, M. E.; Rayment, T. Solvation Forces near a Graphite Surface Measured with an Atomic Force Microscope Solvation Forces Microscope near a Graphite Surface Measured with an Atomic Force. *Appl. Phys. Lett.* **1992**, *60*, 2356–2358.
- (53) Khan, S. H.; Matei, G.; Patil, S.; Hoffmann, P. M. Dynamic Solidification in Nanoconfined Water Films. *Phys. Rev. Lett.* **2010**, *105*, 106101.
- (54) Patil, S.; Matei, G.; Oral, A.; Hoffmann, P. M. Solid or Liquid? Solidification of a Nanoconfined Liquid under Nonequilibrium Conditions. *Langmuir* **2006**, *22*, 6485–6488.
- (55) Dhinojwala, A.; Granick, S. Relaxation Time of Confined Aqueous Films under Shear. *J. Am. Chem. Soc.* **1997**, *119*, 241–242.
- (56) Antognozzi, M.; Humphris, A. D. L.; Miles, M. J. Observation of Molecular Layering in a Confined Water Film and Study of the Layers Viscoelastic Properties. *Appl. Phys. Lett.* **2001**, *78*, 300–302.
- (57) Zhu, Y.; Granick, S. Viscosity of Interfacial Water. *Phys. Rev. Lett.* **2001**, *87*, 096104.
- (58) Li, T.-D.; Riedo, E. Nonlinear Viscoelastic Dynamics of Nanoconfined Wetting Liquids. *Phys. Rev. Lett.* **2008**, *100*, 106102.
- (59) Li, T.-D.; Gao, J.; Szoszkiewicz, R.; Landman, U.; Riedo, E. Structured and Viscous Water in Subnanometer Gaps. *Phys. Rev. B* **2007**, *75*, 115415.
- (60) Ortiz-Young, D.; Chiu, H.-C.; Kim, S.; Voitchovsky, K.; Riedo, E. The Interplay between Apparent Viscosity and Wettability in Nanoconfined Water. *Nat. Commun.*

- 2013**, *4*, 2482.
- (61) Kageshima, M. Layer-Resolved Relaxation Dynamics of Confined Water Analyzed through Subnanometer Shear Measurement. *EPL* **2014**, *107*, 66001.
- (62) Jeffery, S.; Hoffmann, P. M.; Pethica, J. B.; Ramanujan, C.; Özer, H. Ö.; Oral, A. Direct Measurement of Molecular Stiffness and Damping in Confined Water Layers. *Phys. Rev. B* **2004**, *70*, 054114.
- (63) Jarvis, S. P.; Uchihashi, T.; Ishida, T.; Tokumoto, H.; Nakayama, Y. Local Solvation Shell Measurement in Water Using a Carbon Nanotube Probe. *J. Phys. Chem. B* **2000**, *104*, 6091–6094.
- (64) Major, R. C.; Houston, J. E.; McGrath, M. J.; Siepmann, J. I.; Zhu, X. Y. Viscous Water Meniscus under Nanoconfinement. *Phys. Rev. Lett.* **2006**, *96*, 5–8.
- (65) Li, T.-D.; Riedo, E. Nonlinear Viscoelastic Dynamics of Nanoconfined Wetting Liquids. *Phys. Rev. Lett.* **2008**, *100*, 106102.
- (66) Kageshima, M. Layer-Resolved Relaxation Dynamics of Confined Water Analyzed through Subnanometer Shear Measurement. *EPL (Europhysics Lett.)* **2014**, *107*, 66001.
- (67) Kapoor, K.; Amandeep; Patil, S. Viscoelasticity and Shear Thinning of Nanoconfined Water. *Phys. Rev. E* **2014**, *89*, 013004.
- (68) Khan, S. H.; Kramkowski, E. L.; Ochs, P. J.; Wilson, D. M.; Hoffmann, P. M. Viscosity of a Nanoconfined Liquid during Compression. *Appl. Phys. Lett.* **2014**, *104*, 023110.
- (69) Klein, J.; Kumacheva, E. Simple Liquids Confined to Molecularly Thin Layers. I. Confinement-Induced Liquid-to-Solid Phase Transitions. *J. Chem. Phys.* **1998**, *108*, 6996–7009.
- (70) Demirel, A. L.; Granick, S. Origins of Solidification When a Simple Molecular Fluid Is Confined between Two Plates. *J. Chem. Phys.* **2001**, *115*, 1498–1512.
- (71) Demirel, A. L.; Granick, S. Glasslike Transition of a Confined Simple Fluid. *Phys. Rev. Lett.* **1996**, *77*, 2261–2264.
- (72) Patil, S.; Matei, G.; Grabowski, C. A.; Hoffmann, P. M.; Mukhopadhyay, A.

- Combined Atomic Force Microscopy and Fluorescence Correlation Spectroscopy Measurements to Study the Dynamical Structure of Interfacial Fluids. *Langmuir* **2007**, *23*, 4988–4992.
- (73) Mukhopadhyay, A.; Zhao, J.; Bae, S. C.; Granick, S. Contrasting Friction and Diffusion in Molecularly Thin Confined Films. *Phys. Rev. Lett.* **2002**, *89*, 136103.
- (74) Mukhopadhyay, A.; Bae, S. C.; Zhao, J.; Granick, S. How Confined Lubricants Diffuse During Shear. *Phys. Rev. Lett.* **2004**, *93*, 236105.
- (75) Bureau, L. Nonlinear Rheology of a Nanoconfined Simple Fluid. *Phys. Rev. Lett.* **2010**, *104*, 218302.
- (76) Granick, S. Motions and Relaxations of Confined Liquids. *Science* **1991**, *253*, 1374–1379.
- (77) Hofbauer, W.; Ho, R. J.; R., H.; Gosvami, N. N.; O’Shea, S. J. Crystalline Structure and Squeeze-out Dissipation of Liquid Solvation Layers Observed by Small-Amplitude Dynamic AFM. *Phys. Rev. B* **2009**, *80*, 134104.
- (78) Krass, M.-D.; Gosvami, N. N.; Carpick, R. W.; Müser, M. H.; Bennewitz, R. Dynamic Shear Force Microscopy of Viscosity in Nanometer-Confined Hexadecane Layers. *J. Phys. Condens. Matter* **2016**, *28*, 134004.

Chapter 2

Experimental and Theoretical Methods

Understanding of flow properties of nanoconfined liquids is central to a wide range of areas from biology to nanofluidics devices. Flow properties of nanoconfined fluids are mainly measured by two methods, i.e., by performing flow measurement and shear measurement. In flow measurement, the flow of liquid through the nanochannels is examined under a gradient of external force to measure its flow properties such as viscosity, diffusion. In shear measurement, the oscillatory strain is applied to one plate to oscillate it in liquid medium and stress generated due to surrounding liquid is measured. For measuring the shear response of nanoconfined liquid, the separation between two plates is in nanometre scale. The fluid volume involved for viscosity measurement of nanoconfined liquids is of the order of attoliters to zeptoliters, and the shear forces that they generate are in pico-Newton (pN) to nano-Newton (nN) range.

Conventional Rheology instruments are not capable of capturing the possible nonlinear behavior of these thin films. SFA and AFM set-ups are modified to measure the shear stress developed due to straining of nanoconfined thin films of liquid. In both SFA and AFM experiments the shear frequency is limited from a few Hz to 1 kHz. To measure the change in relaxation time upon confinement, we need a broader shear frequency range, typically larger than the inverse of the system's relaxation time. Also, jump-to-contact instability of the confining surfaces is a severe issue in controlling the film thickness while shear straining these films. It is, therefore, crucial to develop new techniques employing force sensor which have large normal stiffness to avoid the instability and can perform in the broader shear frequency range with force sensitivity of the order of nN. This chapter reports the development of an instrument for oscillatory rheology on nanoconfined liquids with unprecedented shear frequencies and nearly infinite normal stiffness. Detail instrumentation and measurement methodology developed to measure the viscous drag of nanoconfined liquid is explained in the following text.

2.1 Details of Instrument

Our home-built tuning fork based shear rheometer consists quartz tuning fork based force sensor and sample stage assembly. Force sensor consists of diether piezo, tuning fork and fiber tip which is attached to free prong of tuning fork. Sample stage assembly consists of two piezo tubes responsibly for movement in the Z direction. All the details about the force sensor and sample assembly are explained in next sections.

2.1.1 Tuning fork, the Force Sensor

Tuning fork acts as essential part of our instrument. It consists of two prongs and is made up of quartz crystal which is piezoelectric in nature^{1,2}. The dimension of one prong of the tuning fork is 6mm x 350 μ m x 620 μ m. Fig. 2.1 shows SEM image of a tuning fork which is used as a force sensor in our experimental setup.

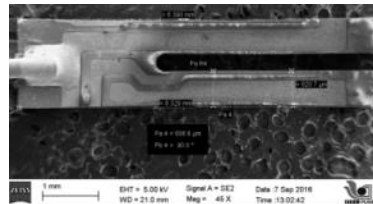


Fig. 2.1: SEM image of the Tuning fork

Electrodes are designed and connected in such as way over the two prongs to accumulate maximum charge per mechanical deflection as shown in Fig. 2.2.

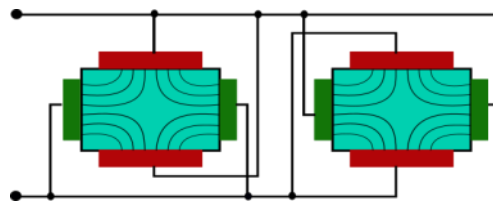


Fig. 2.2 Electrode connection of Tuning Fork

The resonance frequency of tuning fork is 32.764Hz and has a very high-quality factor (10000). Due to high-quality factor, it has excellent use in timekeeping application³ Such as; quartz crystal watches. The time accuracy of quartz watches depends on frequency shift which could occur due to change in temperature, acoustic vibration, and aging effects. The frequency shift of quartz crystal is about 2×10^{-6} Hz per year. The efficient design of geometry and arrangement of electrodes is responsible for this small frequency shift. At resonance frequency, two prongs of tuning fork move out of phase which exerts equal and

opposite force at center holder hence the net force exerted on the central region is zero which also play a role in less damping of the system. Tuning fork has high spring constant (10^5 N/m) and low thermal noise. In spite, of having large spring constant, it has high force sensitivity in the range of nN-pN⁴.

2.1.2 Fibre Tip

To measure the viscous drag of liquid environment fiber tip was attached to tuning fork prong to avoid its contact with the liquid. Fiber tip was made by pulling single mode optical fiber in Sutter instrument under CO₂ laser heating⁵. Sutter instrument consists of various programs with parameters such as; heat, filament, velocity, delay and pull. The value of these parameters play major role in forming probe of particular taper length and diameter. Heat parameter controls current through the filament and is required to melt a piece of optical fiber. Filament parameter sets the limit of the longitudinal area for projection of laser beam on fiber. Velocity parameter specifies the speed at which the glass carriage must be moving before the hard pull is executed. Velocity of the glass carriages during the initial pull is dependent on the viscosity of the glass and viscosity of the glass is dependent on its melting temperature. Delay parameter controls the time between when the heat turns off and when the hard pull will be activated which is required to separate out glass into two parts. Pull parameter controls the force of the hard pull to separate out fiber into two parts to form two fibre tips of equal diameter.

2.1.3 Mechanical Excitation of the Tuning fork

For mechanical excitation tuning fork with fiber tip attached is fixed on diether piezo⁶. We refer to the whole assembly as probe assembly. It is shown in Fig. 2.3. The tuning fork is mechanically excited by providing AC voltage to diether piezo. Being piezoelectric in nature, mechanical oscillation in tuning fork gives rise to the current signal. The current signal is measured with the help of high gain ($10^6 - 10^8$) preamplifier and lock-in amplifier at a fixed frequency.

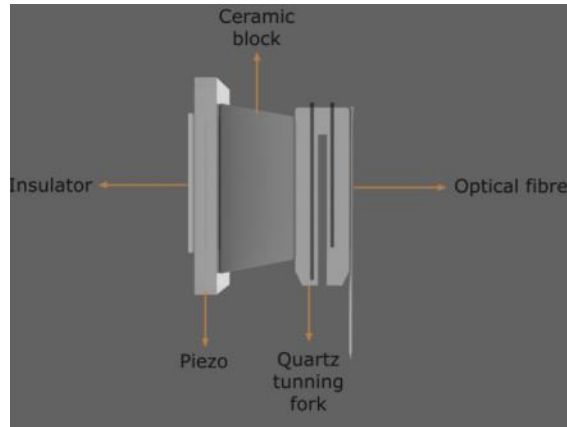


Fig. 2.3 Probe assembly of an experiment set up consists of a Tuning fork with fiber tip is fixed to diether piezo for mechanical excitation.

2.1.4 Electrical Circuit of Tuning fork

Electrical equivalent circuit for the mechanical oscillator is represented by LCR circuit and shown in Fig. 2.4. Tuning fork also acts as mechanical oscillator so; its electrical equivalent circuit is represented⁷ by LCR circuit with C_2 in parallel. C_2 is known as parasitic capacitance. It exists due to electrodes or connections on tuning fork. The current flow through prongs (eqⁿ 2.1) consists of two terms; (i) due to differential bending of two prongs (ii) parasitic current flowing through parasitic capacitance.

$$I = \alpha\omega(A_1 - A_2) + \omega C_2 V \quad \text{-----} \quad (2.1)$$

Where α is coupling constant and it's value is $12 \mu\text{C}/\text{V}$, ω is oscillation frequency, A_1 and A_2 are oscillation amplitudes of fixed and free prong respectively, C_2 is a parasitic capacitor, and V is drive voltage which applied to diether piezo.

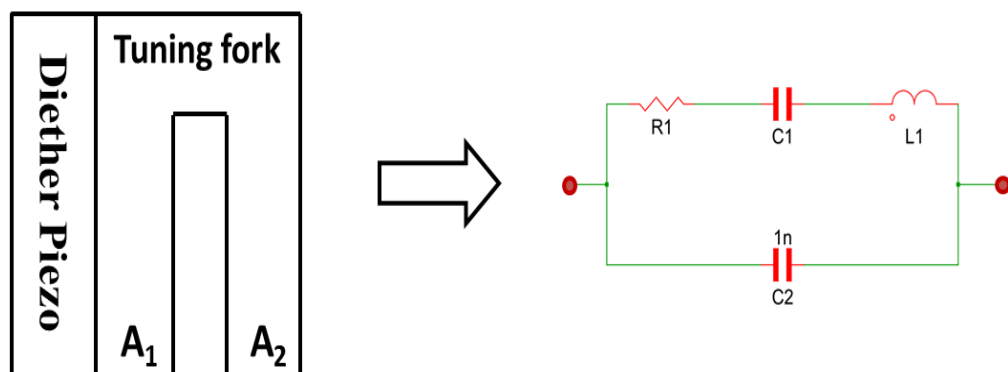


Fig. 2.4 Electrical equivalent circuit of tuning fork.

2.1.5 Calibration of oscillation amplitudes

Oscillation amplitude of tuning fork free prong and diether piezo was determined by using fiber-based interferometer shown in Fig. 2.5. The oscillation amplitude was measured for a range of frequency and with a voltage applied across diether piezo. For 1-5 kHz range of frequency, we found no change in amplitude of free prong but rise in current signal. At off-resonance frequency (1-15 kHz) both prongs of tuning fork oscillate with same phase and amplitude. It shows that there will be no current signal due to differential bending of two prongs. The rise in current signal is observed due to parasitic capacitance. As parasitic current is directly proportional to frequency ($I_p = \omega C_p V$). Calibrated amplitude for tuning fork free prong obtained by performing fibre based interferometry measurement is 1.2 nm/V. Fig. 2.6 shows oscillation amplitude versus applied voltage and current signal versus frequency respectively.

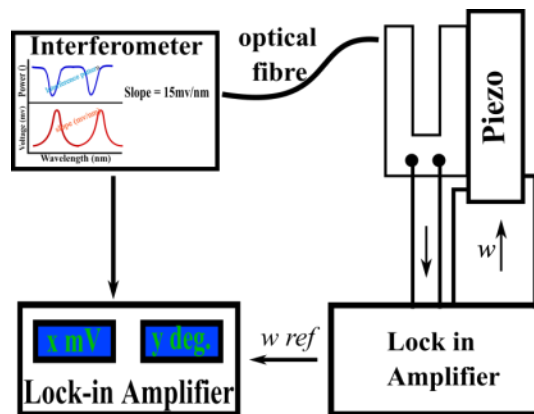


Fig. 2.5 A schematic of fiber-based interferometer setup. It was employed to measure oscillation amplitude of tuning fork free prong.

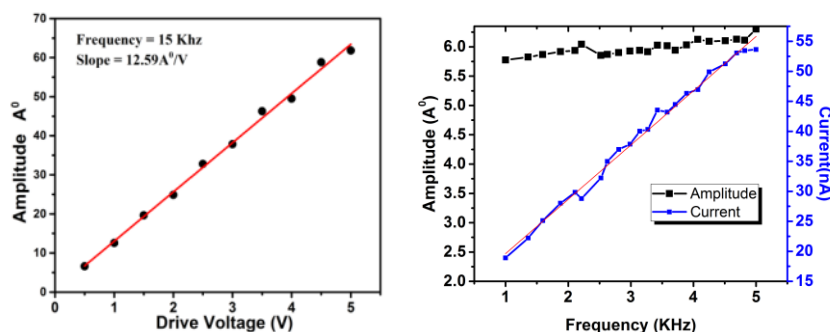


Fig. 2.6 (a) Plot of oscillation amplitude versus drive voltage applied across diether piezo. (b) Oscillation amplitude versus oscillation frequency at fixed drive voltage.

2.1.6 X-Y-Z Positioner

Sample assembly mainly consists of two piezos i) Hammer piezo ii) Scanner piezo. These piezos play vital role for movement of the substrate in Z direction towards fiber tip with the precision of nm and range of mm. For approaching the fiber tip from separations of mm to nm, we used the inertial sliding approach mechanism used first by Pohl². The entire approach mechanism is placed in a heavy steel base; the central part is carved out to accommodate coarse and fine X-Y-Z positioner. To achieve coarse motion a steel piece called hammer is attached to one end of a piezo tube (hammer piezo). On top of the hammer piezo, a quartz glass tube is fitted. This tube is inserted in a metal connector having a copper leaf spring that holds the quartz tube. The tension in the leaf spring can be adjusted to achieve the best motion in a vertical direction against gravity. The quartz tube makes contact with the connector piece along flat walls. Voltage pulses with a slowly rising edge and fast drop off are applied to the hammer piezo. During the initial slow rising of the pulse, the hammer piezo contracts (expands) moving the hammer up (down) and the tube remains clamped at the leaf spring. When the voltage suddenly drops to zero, the hammer stays in its place and due to inertia pushing the tube up (down) achieving a net movement in each pulse. The inertial sliding mechanism^{2,8} is represented in Fig. 2.8. The height and width of the pulse can be controlled to achieve the desired step length. The connector bearing the quartz tube is placed onto a coarse X-Y scanner. The quadrant piezo tube (scanner piezo) is mounted inside the quartz tube and moves with the hammer piezo, hammer, and the quartz tube assembly. Scanner piezo was moved up-down and X-Y direction by applying voltage ramp. A liquid cell is magnetically attached to the top of the scanner tube. The cell comprises of two circular Teflon pieces clamped together with a Viton O-ring between them. The top Teflon piece has an opening to allow access to the fiber tip mounted on the tuning fork. The liquid is filled in the cell from the top opening with a glass syringe. Fig. 2.7 shows whole sample assembly⁹.

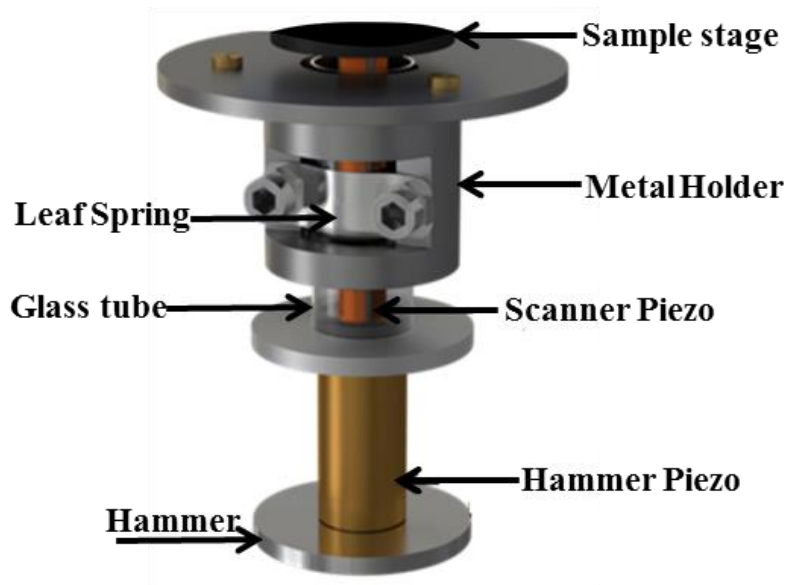


Fig. 2.7 Sample assembly of the instrument.

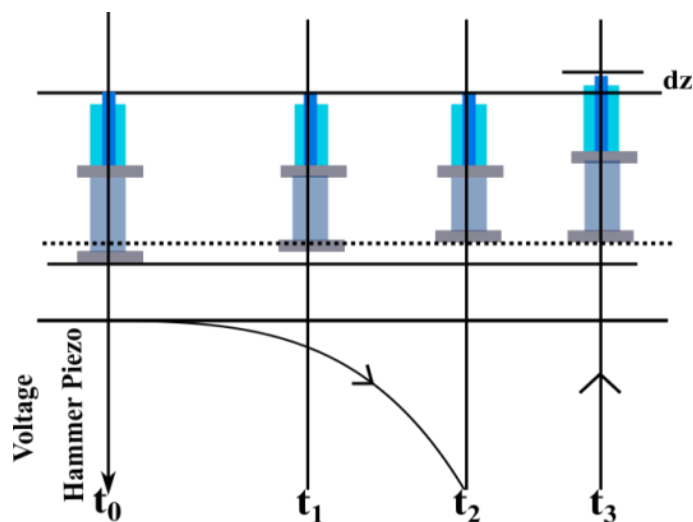


Fig. 2.8 shows inertial sliding principle to achieve movement in Z direction corresponding to the saw-tooth pulse.

2.2 Electronics

2.2.1 Electronics Circuits

Various electronic circuits are required for operation of the instrument such as; preamplifier, high voltage amplifier and feedback. Preamplifier circuit is to amplify the current signal generated by tuning fork due to mechanical deflection. (ii) High Voltage Operational amplifier is to amplify saw-tooth voltage pulses and voltage ramp to hundreds volt required for movement of piezos in the Z direction. (iii) Feedback circuit is to hold fiber tip attached

tuning fork in the interaction region. All these circuits are explained in details in the following text.

2.2.2 Pre-amplifier

Preamplifier¹⁰ is used to amplify nano-amperes of current signal with high gain (10^6 - 10^8). Fig. 2.9 shows a circuit diagram of the preamplifier. It consists of OPA656¹¹ operational amplifier IC. Power supply value for OPA656 is $\pm 5V$.

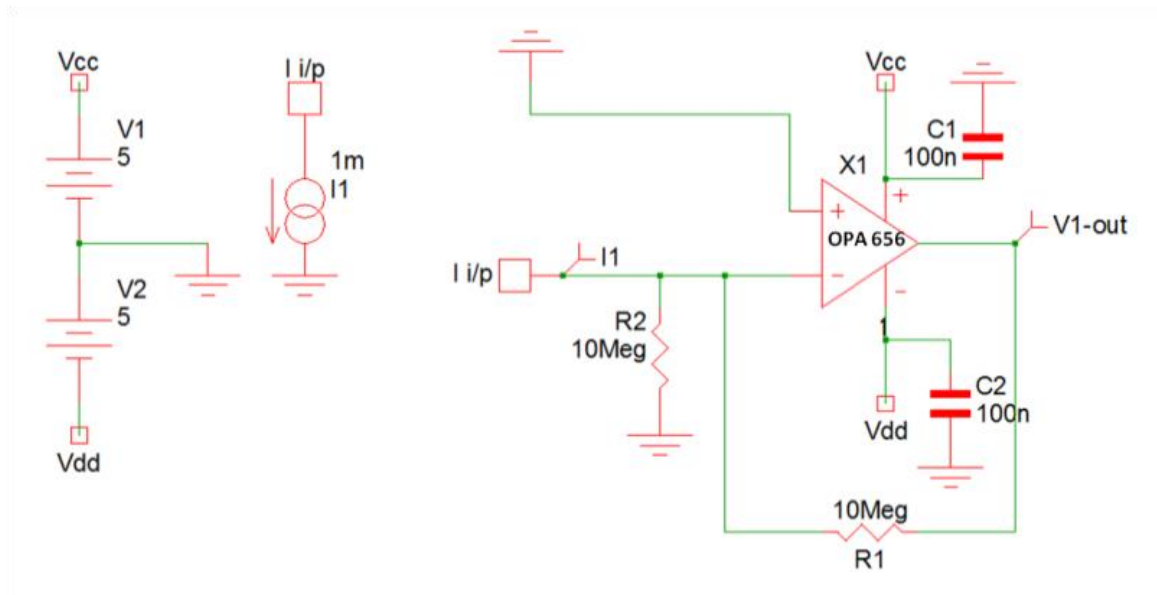


Fig. 2.9 Circuit diagram of the OPA656 preamplifier.

2.2.3 High Voltage operational amplifier

High Voltage operational amplifier (HV op-amp)¹² is to amplify the voltage pulses generated by DAQ up to hundreds of volts. BB3584jm¹³ was used for high voltage amplifier (optional PA88, PA340CC). Power supply value required for operation op-amp BB3584 is $\pm 150V$. Maximum output voltage value can be achieved 300V. The circuit diagram using PA88 opamp is shown in Fig. 2.10.

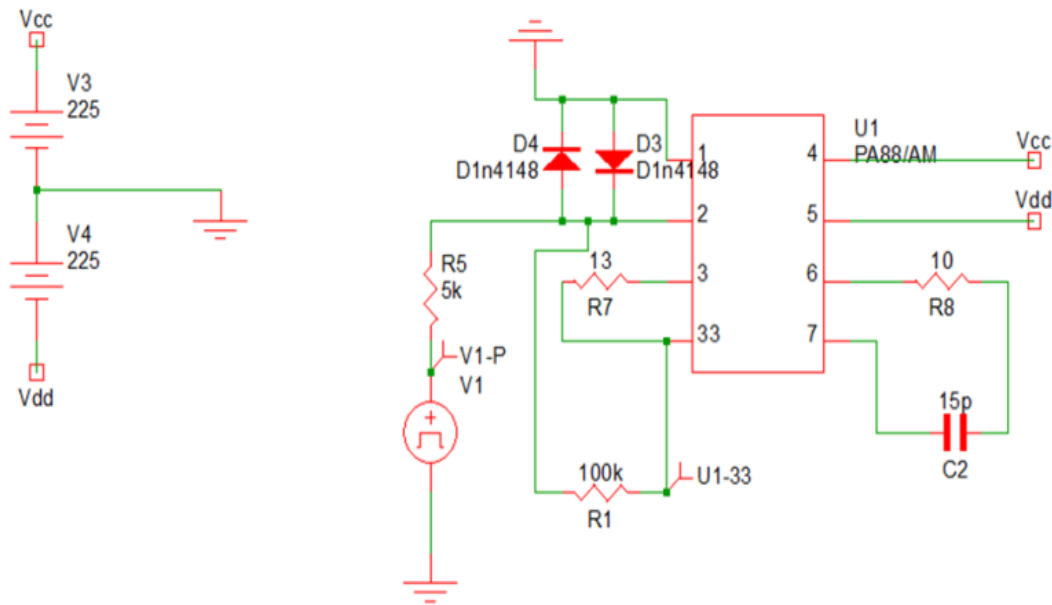


Fig. 2.10 Circuit diagram of high voltage operational amplifier.

2.2.4 Proportional Integrator (PI) Feedback

Feedback has become a necessary tool for an experimentalist to improve the stability of instruments. Feedbacks are mostly used for precise control of temperature, for enhancing the performance of AFM and in other devices to achieve stability. The primary objective of the feedback circuit is to keep the state of system locked or set to desired value $S = S_d$.

Feedback working principle

1. To lock or set the state of the system to desired value following procedure is followed.
2. Measure state S of the system.
3. Measure how far the system is from the desired set point, it is sensed by measuring the error signal.
4. Calculate a trail control value $u = u(e)$.
5. Feed this controlled value back into the input of the system.
6. The state of system changes in response to a change in control value.

This process will keep on moving until the desired set point is reached.

In our feedback circuit, we used proportional and integral gain. Proportional term plays a role in estimating the error signal between the output value and set point of a system for particular

time. Whereas integral term considers the history of the error, or how long and how far the measured process variable has been from the set point over time before correcting for error.

The following relation gives the output of PI controller.

$$u(e, t) = g_p e(t) + g_I \int_0^t e(t) dt$$

Where $e(t)$ is error signal, g_p is proportional gain and g_I is an integral gain.

CA3140 IC¹⁴ was used for designing PI feedback circuit. The circuit diagram of PI feedback is Fig. 2.11.

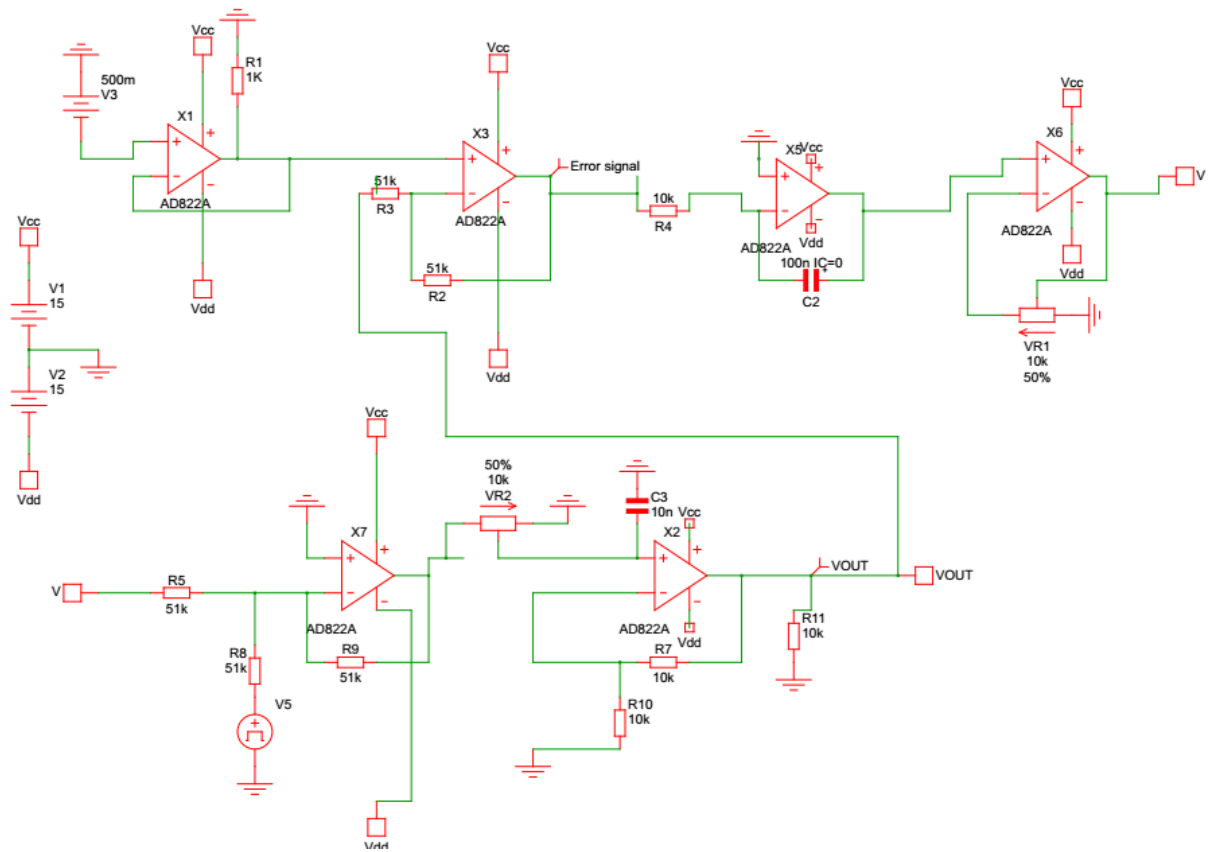


Fig. 2.11 Circuit diagram of closed loop PI feedback using CA3140 opamp IC.

2.2.5 Data Acquisition card (DAQ (6259))

DAQ 6259 PXI Express¹⁵ was employed to read and write data from our experimental setup. DAQ 6259 consists of 4 Analog output and 16 Analog inputs. The sampling rate of Analog input is 1MS/s. The sampling rate for analog output is dependent on channels in use. For 1 channel in use it is 2.56MS/s, 2 channels- 2 MS/s, 3 channels - 1.54MS/s, 4 channels - 1.25

MS/s. The minimum value of voltage can be read from the analog input is 0.11mV on the $\pm 10V$ scale. Minimum output value can be generated for Analog output is 2mV on a scale of $\pm 10V$ and 1mV on a scale of $\pm 5V$. By knowing calibration of scanner piezo and minimum possible value of voltage can be generated from DAQ card, it is possible to achieve smallest step size as 0.3Å. LabVIEW for used for interfacing of DAQ with the instrument.

2.2.6 Lock-in Amplifier

Lock-in amplifier¹⁶ is used to detect and measure AC signals and convert it into DC voltage at the reference frequency of the oscillator. Lock-in amplifier uses a technique called phase sensitive detection to single out the component of the signal of the specific reference frequency. Phase-sensitive detector (PSD) multiplies the output signal with the reference frequency signal and filters it using low pass filter to single out the DC component resultant of the signal at the particular reference frequency. See reference for more details¹⁶. PSD can detect the signal with bandwidth as narrow as 0.01. In following we briefly discuss the advantage of using lock-in amplifier.

If we measure the signal output using an amplifier with a bandpass filter with a $Q=100$ (a perfect filter) centered at 10 kHz, any signal in a 100 Hz bandwidth will be detected (10 kHz/ Q). A good noise amplifier has small noise as $5nV/(Hz)^{1/2}$. The noise in the bandpass filter will be $50 \mu V (5nV/\sqrt{Hz} \times \sqrt{100} Hz \times 1000)$ and the signal will still be $10 \mu V$. The output noise is much greater than the signal and, an accurate measurement cannot be made. Further gain will not help the signal to noise problem.

Phase sensitive detector (PSD) is used for analyzing the signal to high precision. The PSD can detect the signal of any frequency with bandwidth as small as 0.01 Hz. Due to very narrow bandwidth, the noise in the detection bandwidth will be only $0.5 \mu V$ but the signal is still $10 \mu V$. It makes a signal to noise ratio to be 20, and accurate measurement of the signal is possible. Hence, lock-in amplifier plays an essential role in measuring small voltage signal obscured with noise. In our experimental setup, SRS830 lock-in amplifier¹⁶ was employed to measure voltage signals.

2.3 Operational details of Instrument

The Instrument uses Tuning Fork as a Force Sensor. Fig. 2.12 shows schematic of the instrument. A quartz crystal tuning fork, which is piezoelectric, is mechanically excited using diether piezo. The current generated due to differential bending of prongs is measured using

pre-amplifier. The confinement of liquid takes place between the optical fiber attached to tuning fork and substrate placed in a liquid cell on XYZ sample stage. The sample stage moved in steps of mm to nm toward optical fiber for confining liquid between fiber tip and substrate using coarse and fine approach principle. The approach is made by simultaneously oscillating tuning fork at the resonance frequency, as there is a maximum change in signal during interaction with the substrate. Once the sensor is reached near the substrate which is known by looking at change in amplitude to 60% of its bulk amplitude at resonance frequency, then it is held at that particular position called interaction region with the help PI feedback. Afterward, the oscillation frequency of force sensor is changed to off-resonance for measuring the shear response of confined liquid by varying separation between substrates. The instrument is interfaced with the computer by using Lab view programming. Various LabVIEW programs are written for different tasks (i) Auto Approach Program, for the coarse and fine approach of the substrate towards the tip (ii) Data acquisition, for acquiring and storing data in particular file. The details of all programs are described below.

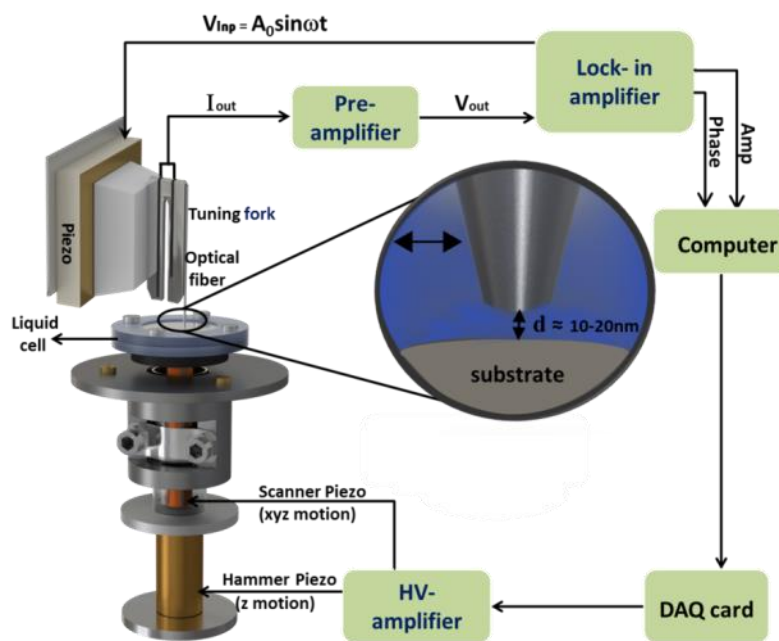


Fig. 2.12 Schematic of our experimental set-up

2.3.1 Automation using LabVIEW

The manual approach of tip towards substrate is impossible as one surface moves towards another surface in steps of nanometers. Thus, a fully automated approach mechanism is required and is developed using LabVIEW software. The program contains the generation of waveforms for the scanner and hammer piezo tubes, auto approach and data acquisition

system to obtain the force curves. The slow rising saw-tooth pulses for the hammer piezo were created. The pulses were programmed in such a way that the frequency, the amplitude, the time between two burst and number of pulses in a burst could be easily controlled. Alone, these pulses are used to control the coarse Z motion. But together with the triangular ramp pattern for the scanner, they form the auto approach mechanism. During the auto approach, the scanner moves a distance towards the tip in small steps, checking at each step whether the tip is engaged with the sample or not. The interaction region is determined from the difference between the output signal from the tuning fork and a set-point amplitude. If the tip is not in the interaction region for the entire range, then the scanner comes back to its original length, and the hammer is moved by a distance, a little less than the scanner range, towards the sample. It keeps on running until the set-point amplitude is reached, which defines that the tip is in the interaction region. Once the setpoint is reached, the control of the program is transferred immediately to the PID controller, to hold the tip at a particular position.

The approach is made on resonance as there is maximum amplitude change and it is easy to determine when the tip is engaged with the sample. The final step of the program is to collect data. PI Feedback is disabled, and the scanner piezo is given a voltage ramp of the desired range, and at each step the amplitude and phase values of the tuning fork are collected and stored into the computer. During data acquisition, the control of the range, step size and the number of points are user controllable.

2.4 Measurement Methodology

Measurement methodology was developed to measure the dissipation coefficient of tuning fork tip bearing prong in liquid medium from the measured current signal. Tuning fork generates current signal due to differential bending between two prongs oscillating at resonance or off-resonance frequency. It is given by eqn 2.2. below.

$$I_a = \alpha\omega(A_{drive} - A_{tip}) + I_p \quad \text{-----} \quad (2.2)$$

Where α is coupling constant with units C/m. It defines the charge accumulation on the electrode of tuning fork per unit deflection, ω is oscillation frequency, I_p is parasitic current due to electrodes on tuning fork or connecting wires.

At Resonance frequency, $A_{tip} \gg A_{drive}$ so current equation will reduce to:

$$I_a = \alpha\omega(A_{tip}) + I_p \quad \text{-----} \quad (2.3)$$

At off-resonance frequency $A_{\text{drive}} \leq A_{\text{tip}}$ so the current equation will be same as given by eqn 2.2

$$I_a = \alpha\omega(A_{\text{drive}} - A_{\text{tip}}) + I_p \quad \text{-----} \quad (2.4)$$

Eqn 2.3 implies that at the resonance frequency, the current signal is just proportional to the amplitude of tip bearing prong. At off-resonance, eqn 2.4 means that the current signal is proportional to the differential amplitude of both prongs. The tip experiences a drag force while going from air to liquid. Fig. 2.13 shows the change in current at resonance and off-resonance frequency while dipping the tip into the fluid. At resonance frequency, we always find a decrease in current value whereas at off-resonance there is an increase in current value.

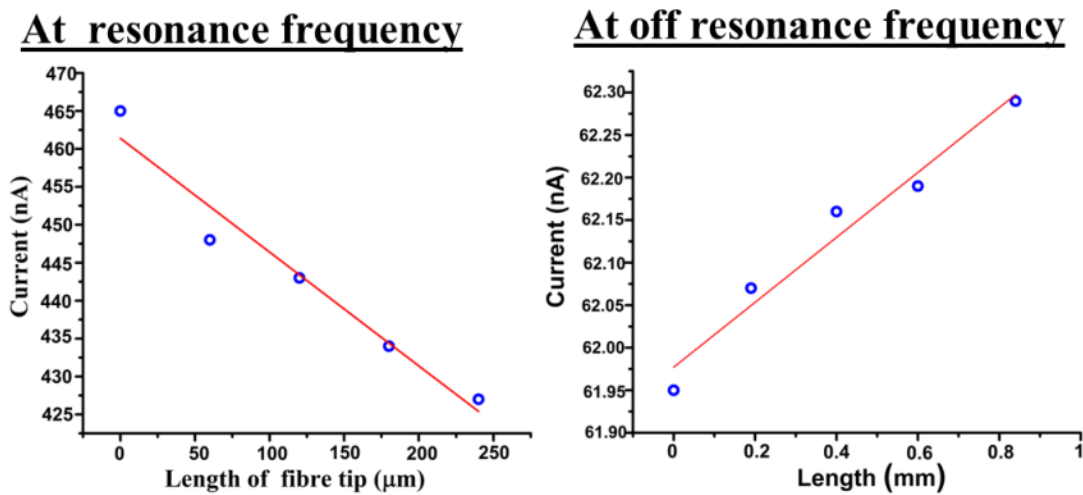


Fig. 2.13 shows the change in the current signal while the tip into a liquid at resonance and off-resonance frequency. The minimum sensitivity of tuning fork is 0.2pA/pm^{17} .

2.4.1 Determination of oscillation amplitude from a current value

Oscillation amplitude of tip bearing tuning prong at bulk and confinement can be evaluated from current equation once oscillation amplitude of the same is known in the air. As described previously, the oscillation amplitude of tuning fork free prong is determined by using fiber-based interferometry. Current equations are employed for determining oscillation amplitude at bulk and confinement of liquid. All details are as follow

In the air, at off-resonance frequency current equation is written as follow:

$$I_a = \alpha\omega(A_{\text{drive}} - A_{\text{tip}}) + I_p \quad , \text{ where } A_{\text{drive}} = A_{\text{tip}} \quad \text{-----} \quad (2.5)$$

Where A_{drive} is drive amplitude, A_{tip} is oscillation amplitude of tip bearing prong.

In bulk of the liquid, it is :

$$I_b = \alpha\omega(A_{drive} - A_b) + I_p \quad \text{-----} \quad (2.6)$$

A_b is oscillation amplitude of tip bearing prong in bulk liquid.

Where $A_{drive} \approx A_{tip}$, to evaluate amplitude of tip bearing prong at bulk eqn 2.5 is subtracted from 2.6, it is reduced to following eqn:

$$\Delta I = I_b - I_a = \alpha\omega(A_{drive} - A_b)$$

$$A_b = A_{drive} - \frac{I_b - I_a}{\alpha\omega} \quad \text{-----} \quad (2.7)$$

Similarly, oscillation amplitude under confinement is evaluated by measuring the change in current signal going from bulk liquid to confinement and described below:

$$\Delta I_c = I_c - I_b = \alpha\omega(A_b - A(d))$$

$$A(d) = A_b - \frac{I_c - I_b}{\alpha\omega} \quad \text{-----} \quad (2.8)$$

Where $A(d)$ is distance dependent amplitude of prong at confinement.

2.4.2 Determination of dissipation coefficient from amplitude and phase

Oscillation amplitude of tip bearing prong is measured using previous mathematical eqn's. The change in amplitude and phase was converted into more meaningful parameter which is dissipation coefficient. For force sensor oscillating at off-resonance frequency¹⁸, dissipation coefficient was derived by solving the kinematic equation for force sensor oscillating at the off-resonance frequency.

$$P_{in} = P_{tip} - P_0 \quad \text{-----} \quad (2.9)$$

Where P_{in} is power input to the sensor using drive voltage, P_0 is power output of the sensor and P_{tip} is due to intrinsic power losses in the tip (sensor).

At off-resonance frequency, the cantilever oscillates at minimal amplitude. Intrinsic loss term related to the cantilever is tiny = 10^{-4} Joule/sec, it can be ignored so above equation reduced to relation below¹⁹:

$$P_{in} = F_d(t)Z_d(t)$$

$$F_d(t) = K_{\text{lever}}(Z(t) - Z_d(t))$$

Where F_d is drive force, K_{lever} is stiffness constant of cantilever and $Z(t)$ is oscillation amplitude of cantilever tip, and $Z_d(t)$ is oscillation amplitude of cantilever base.

$$P_{\text{in}} = K_{\text{lever}}[Z(t) - Z_d(t)]\dot{Z}_d(t) \quad \text{-----} \quad (2.10)$$

Where

$$Z_d(t) = A_0 \cos(\omega t) \quad \text{-----} \quad (2.11)$$

K_{lever} is stiffness constant of the force sensor, $Z(d)$ is drive amplitude of cantilever. A is magnitude and ω is oscillation frequency.

And

$$Z(t) = A \cos(\omega t - \varphi) \quad \text{-----} \quad (2.12)$$

where $Z(t)$ is expression for cantilever oscillation amplitude.

Total power loss per unit circle is given by putting relation defined by eqn 2.11 and 2.12:

$$P_{\text{in}} = \frac{1}{T} \int_0^T P_{\text{in}} dt$$

$$P_{\text{loss}} = \frac{1}{2} K_{\text{lever}} \omega A_0 A \sin(\varphi) \quad \text{-----} \quad (2.13)$$

Similarly, Energy loss per cycle is given by

$$E_{\text{loss}} = \frac{2\pi}{\omega} P_{\text{loss}}$$

$$E_{\text{loss}} = \pi K_{\text{lever}} A_0 A \sin(\varphi) \quad \text{-----} \quad (2.14)$$

The corresponding damping force:

$$F_{\text{loss}} = \frac{E_{\text{loss}}}{\pi A}$$

$$F_{\text{loss}} = K_{\text{lever}} A_0 \sin(\varphi) \quad \text{-----} \quad (2.15)$$

Dissipation coefficient evaluated from F_{loss} is as follow:

$$F = \gamma V$$

$$F = \gamma A \omega$$

$$\gamma = \frac{F}{A \omega}$$

$$\gamma = -\frac{K_{\text{lever}}A_o\sin(\varphi)}{A\omega} \quad \text{-----} \quad (2.16)$$

Eqn (2.16) implies that dissipation coefficient is inversely proportional to oscillation amplitude. The decrease in oscillation amplitude corresponds to larger of tip energy to surrounding liquid.

Dissipation coefficient in bulk liquid

By evaluating oscillation amplitude and phase at bulk, it is possible to estimate dissipation coefficient of the tip in bulk liquid which is given as follows :

$$\gamma_b = -\frac{K_{\text{lever}}A_d\sin(\varphi_1)}{A_b\omega} \quad \text{-----} \quad (2.17)$$

Where A_d is drive amplitude, A_b is amplitude in bulk liquid, φ_1 is a change in phase takes place while going from air to liquid.

Dissipation coefficient at confinement

The dissipation, when the tip is close to the substrate (<25nm) and water is confined characterized by the separation dependent amplitude $A(d)$ is given by

$$\gamma_c(d) = -\frac{K_{\text{lever}}A_d\sin(\varphi_1+\varphi_2)}{A(d)\omega} \quad \text{-----} \quad (2.18)$$

Where A_d is drive amplitude, $A(d)$ is amplitude at confinement, φ_2 is addition phase lag from bulk to confinement.

2.4.3 Relative change in dissipation coefficient

Relative change in dissipation coefficient is estimated by taking from the difference of dissipation coefficient going bulk to confinement and then normalizing it with bulk dissipation coefficient value.

$$\frac{\Delta\gamma}{\gamma} = \frac{\gamma_c - \gamma_b}{\gamma_b} = \frac{A_b\sin(\varphi_1+\varphi_2)}{A(d)\sin(\varphi_1)} - 1 \quad \text{-----} \quad (2.19)$$

2.5 Validity of Measurement Methodology

To validate our methodology of estimating dissipation from the amplitude and phase measurement, we measure E_{loss} for two organic liquids of known viscosity. E_{loss} is determined by using the eqn (2.14) stated previously and is rewritten as follow:

$$E_{\text{loss}} = \pi K_{\text{lever}} A_0 A \sin(\varphi) \quad \text{-----} \quad (2.20)$$

One of the liquid is Octamethylcyclotetrasiloxane (OMCTS), a model lubricant having viscosity value 2.6 cP, the other paraffin oil with a considerably high viscosity (55 cP) as compared to OMCTS. We took the same volume of both liquids in the liquid cell. It ensures that the level of liquid above the bottom surface is the same for both liquids. The tip is then immersed in it and approached till it reaches the surface through auto-actuation without breaking the tip. The tip is then pulled back by 100 nm. The ratio of energy loss in OMCTS and paraffin should be equal to the ratio of their known viscosity values. We estimated the E_{loss} value for both liquids from by measuring the change in amplitude (A_b) and the phase lag (φ_1) going from air to bulk liquid. The ratio E_{loss} in both liquids turned out to be 20.68 ± 3 . The ratio of the known viscosity of paraffin and OMCTS is 21.2. It shows that the ratio of E_{loss} measured experimentally agrees well with a ratio of the known viscosity of both liquids. This result ensures that by using eqn (2.18), we will measure dissipation constants accurately. It validates our methodology developed to measure the dissipation coefficient of liquid under confinement.

References

- (1) Friedt, J.-M.; Carry, É. Introduction to the Quartz Tuning Fork. *Am. J. Phys.* **2007**, *75*, 415–422.
- (2) Pohl, D. W. Dynamic Piezoelectric Translation Devices. *Rev. Sci. Instrum.* **1987**, *58*, 54–57.
- (3) Momosaki, E. A Brief Review of Progress in Quartz Tuning Fork Resonators. In *Proceedings of International Frequency Control Symposium*; IEEE, 1997; pp 552–565.
- (4) Grober, R. D.; Acimovic, J.; Schuck, J.; Hessman, D.; Kindlemann, P. J.; Hespanha, J.; Morse, A. S.; Karrai, K.; Tiemann, I.; Manus, S. Fundamental Limits to Force Detection Using Quartz Tuning Forks. *Rev. Sci. Instrum.* **2000**, *71*, 2776–2780.

- (5) Manual Fibre puller. P - 2000. *Fibre Puller Sutter Instrum. P-2000*.
- (6) Technology, P. Piezoelectric Ceramic Products. **2014**, 1–44.
- (7) Rychen, J.; Ihn, T.; Studerus, P.; Herrmann, A.; Ensslin, K.; Hug, H. J.; van Schendel, P. J. A.; Güntherodt, H. J. Operation Characteristics of Piezoelectric Quartz Tuning Forks in High Magnetic Fields at Liquid Helium Temperatures. *Rev. Sci. Instrum.* **2000**, *71*, 1695–1697.
- (8) Blackford, B. L.; Jericho, M. H. A Hammer-Action Micropositioner for Scanning Probe Microscopes. *Rev. Sci. Instrum.* **1997**, *68*, 133–135.
- (9) Kapoor, K.; Kanawade, V.; Shukla, V.; Patil, S. A New Tuning Fork-Based Instrument for Oscillatory Shear Rheology of Nano-Confined Liquids. *Rev. Sci. Instrum.* **2013**, *84*, 025101.
- (10) Jahncke, C. L.; Brandt, O.; Fellows, K. E.; Hallen, H. D. Choosing a Preamplifier for Tuning Fork Signal Detection in Scanning Force Microscopy. *Rev. Sci. Instrum.* **2004**, *75*, 2759–2761.
- (11) IC, D. P. Preamplifier IC. *OPA 656*.
- (12) PA88, D. S. High Voltage Amplifier IC. No. 800.
- (13) Amplifier, H. V. High Voltage Amplifier IC. *BB3584jm*.
- (14) Feedback IC, D. sheet of. Feedback IC. *CA3140*.
- (15) DAQ, M. National Instruments. *DAQ-6259* No. 866, 1–19.
- (16) Manual Lock in amplifier. Model SRS830. *SRS830*.
- (17) Giessibl, F. J. Atomic Resolution on Si(111)-(7×7) by Noncontact Atomic Force Microscopy with a Force Sensor Based on a Quartz Tuning Fork. *Appl. Phys. Lett.* **2000**, *76*, 1470–1472.
- (18) Anczykowski, B.; Gotsmann, B.; Fuchs, H.; Cleveland, J. P.; Elings, V. B. How to Measure Energy Dissipation in Dynamic Mode Atomic Force Microscopy. *Appl. Surf. Sci.* **1999**, *140*, 376–382.
- (19) Hoffmann, P. M.; Jeffery, S.; Pethica, J. B.; Özgür Özer, H.; Oral, A. Energy

Dissipation in Atomic Force Microscopy and Atomic Loss Processes. *Phys. Rev. Lett.*
2001, 87, 265502-1-265502–265504.

Chapter 3

Flow Properties of Nanoconfined Water[†]

3.1 Introduction

Water permeation through hydrophobic channels, such as nanotubes, is five orders larger than expected from conventional fluid theory¹. Similarly, Hydrophobic interiors of membrane proteins allow a rapid transit of water molecules². The flow of water through hydrophilic channels, on the contrary, is hindered compared to bulk water^{3,4}. The measured viscosity through hydrophilic nanochannels is 30 percent larger than bulk water³. The viscosity measurement of nanoconfined water by independent means have resulted in different findings⁵⁻⁸. It has also been argued that water under confinement is a non-Newtonian fluid with finite relaxation⁹⁻¹³. Despite contradictory claims, understanding flow behavior of water under nano-confinement is vital due to its relevance in various areas such as flow through biological pores¹⁴⁻¹⁶, lubrication processes in nano-mechanical devices¹⁷, filtration using nanoporous media^{18,19} and transport through nanofluidic devices^{3,4}.

Conclusions regarding viscosity of nanoconfined water are difficult to reach owing to possible surface effects such as surface registry and finite slip at the boundary^{5,20}. It is also difficult to attribute a physical meaning to this term where the liquid is flowing past a nanotube or is sheared using Atomic Force Microscopy tip. Although no-slip boundary condition is mostly valid for bulk flows, it is suggested that there is a possibility of finite slippage when liquid flows through or is squeezed out of the gap which is of the order of few nm²¹. Indeed, to explain the enhanced flow rates in nanotubes, the violation of no-slip is invoked¹. Researchers in the past have claimed contradictory findings regarding the existence of slip for water nanoconfined by wetting surfaces^{22,23}. The violation of no-slip boundary condition should reveal itself through a reduction in measured stress. This affects the apparent viscosity of nanoconfined liquids and a parameter called "slip-length" is included in models describing the flow²⁰. The slip-length, as defined by the Navier, is the distance from

[†] The version of this chapter is published in Sekhon, A.; Ajith, V. J.; Patil, S. The Effect of Boundary Slippage and Nonlinear Rheological Response on Flow of Nanoconfined Water. *J. Phys. Condens. Matter* 2017, 29, 205101

the boundary inside the solid where liquid velocity is extrapolated to be zero. If slip exists, a wetting surface is expected to exhibit smaller slippage compared to non-wetting ones.

Here, we measure the dissipation in nanoconfined water using a tuning fork based instrument developed in our laboratory. A tip oscillates over a surface at a distance of few nm and the intervening gap between the tip and surface was filled with water. The measurement of change in dissipation from bulk to nano-confinement is measured when the tip approaches from bulk to within a distance of few nm from the surface. Eventually, the tip makes contact with the surface draining all the liquid beneath it to the surrounding bulk. Fig. 3.1 shows the schematic of this process. It was observed that the dissipation was reduced under confinement by 20 %. The observed reduction in dissipation was fitted with Carreau-Yasuda model of shear thinning, assuming that the change in viscosity under confinement is causing the decrease of dissipation.

The characteristic time of shear thinning is found to be $10\mu\text{s}$. To separate the effects of surface wettability and inherent slow-down in dynamics of water molecules on the flow of nanoconfined water, we performed measurements on different substrates. We found that, for entirely wetting to non-wetting substrates, Carreau-Yasuda model comprising finite slip-length fits better to experimentally observed reduction in dissipation. From the fitting, we extract characteristic time-scales and the slip-length for measurements on all the surfaces. The slip is found to increase by 6 folds from 2 to 12 nm with non-wettability (larger contact angles), whereas characteristic time-scales of shear thinning vary by two folds from 28 to 64 μs on different substrates. Thus, the fitting of modified Carreau- Yasuda model to the data suggests that it is possible to single out the dynamics of water molecules under confinement. The slip exists, and it is negligibly small ($< 1\text{nm}$) for thoroughly wetting surfaces ($\Theta = 0^\circ$), such as mica, and increases to 10 nm for intermediate ($\Theta = 50^\circ$) and non-wetting surfaces ($\Theta = 90^\circ$). Although preliminary, these measurements could provide a partial explanation of the enhanced permeation of water through hydrophobic channels^{1,2,19}. The fitting exercise suggests that the flow of water at the nanoscale is determined by both the slip-boundary and the altered response from Newtonian in bulk, to rheological under confinement. The measurements also suggest that the flow under confinement should be treated as that of complex fluids and different experiments may provide inconsistent values for viscosity under confinement, primarily determined by the operational parameters of the measurement.

3.2 Method

3.2.1 The instrument

The measurements were performed using a home-built instrument. Fig. 3.1 shows schematic of instrument. A liquid cell is mounted on the inertial-sliding X-Y-Z positioner. The bottom of the liquid cell holds the substrate which is one of the confining surfaces. The sample is approached towards the tip mounted on one of the prongs of tuning fork. Water is confined between a smooth surface and a fibre tip. The samples are kept in Milli-Q water for a few hours before placing them at the bottom of a liquid cell, which is again immediately filled with Millipore water.

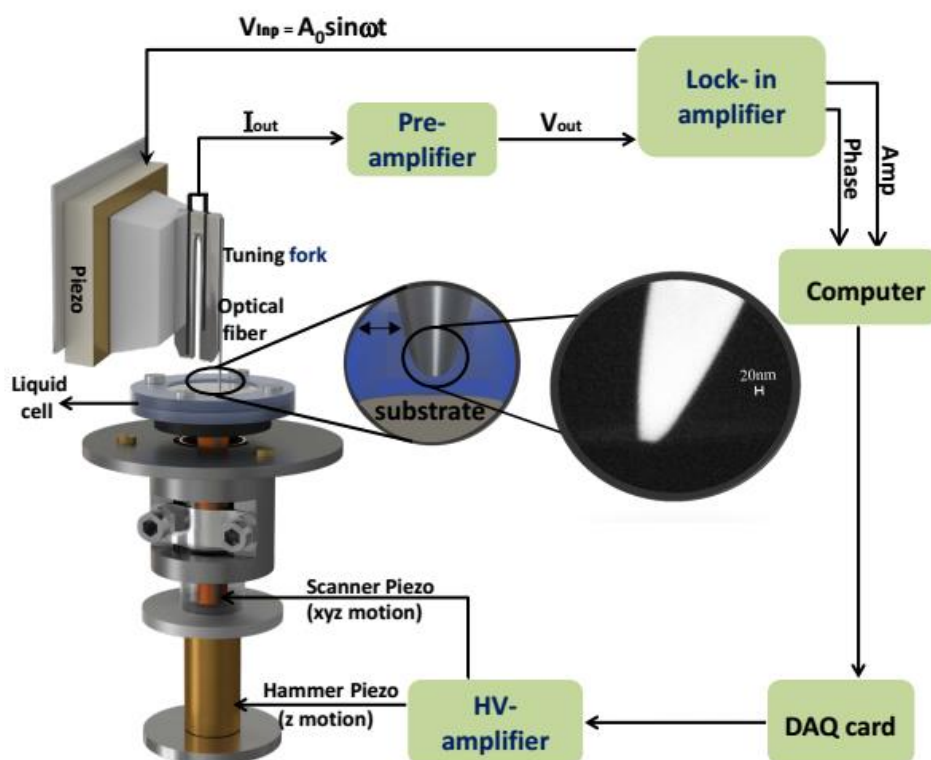


Fig. 3.1 Schematic of the measurements. A tuning fork is used as force sensor to measure the dissipation as the tip oscillates off-resonance in liquid. The current through the electrodes connected to prong surfaces is a measure of the amplitude and phase of the tip-bearing prong. The tip is approached towards the substrate to cause the confinement. The change in dissipation due to altered flow response of the confined molecules beneath the tip is measured as a function of separation (≤ 25 nm).

In a typical measurement, the tip is oscillated off-resonance and brought close to the surface in a controlled manner. The tips are prepared by pulling an optical fiber in laser-based fiber puller and are imaged under Scanning Electron Microscope (SEM) before use. Inset of Fig. 3.1 shows schematic of water confinement in these experiments.

The fiber-tip is fixed on one prong of the tuning fork, and the other prong is mounted on a piezo which is used to provide off-resonance drive to the tuning fork. The current through tuning fork electrodes is due to differential bending in prongs. In off-resonance operation, amplitudes of both the prongs are equal, and the prong motions are in phase. Therefore, the current through the electrodes due to bending is zero. The amplitude of one prong which is bearing the tip reduces due to viscous drag once the tip is immersed in liquid. It causes a finite amount of current to flow through the electrodes. The change in current is measured as the tip is approached towards the surface using a lock-in amplifier and is used to estimate the change in amplitude. In turn, is a measure of dissipation in the tip oscillations. Over the distance covered by the tip in our experiments, the bulk drag force changes by immeasurably small amount. The changes in dissipation are measurably substantial once the tip is within few nm from the surface with water in the intervening gap. Estimation of oscillation amplitude from current signal and dissipation coefficient from amplitude and phase is explained in details in section 2.4.1 and 2.4.2 (Chapter-2)

3.2.2 Models

No-slip boundary condition is likely to be violated when one is measuring the flow properties in nanochannels^{21,22}. This slippage is characterized by a slip length “b,” which is a distance from the boundary inside the solid where liquid velocity, is extrapolated to be zero.

If the liquid under confinement retains its Newtonian nature, rate independent viscosity, the finite slip reduces the viscous stress due to altered shear rate. The shear rate for finite slippage becomes $A\omega/(d+b)$.

The ratio of damping constants then gives the relative change in dissipative force experienced by the tip.

$$\frac{\Delta\gamma}{\gamma} = \frac{d}{d+b} - 1 \quad \text{-----} \quad (3.1)$$

The other possible reason behind the reduction in dissipation upon confinement is shear thinning. Here the change in dissipative force experienced by the tip can be related to altered viscosity. In shear thinning liquids, this depends on shear rate. The phenomenon is observed in non-Newtonian fluids such as whipped cream, polymer melts, and colloidal

suspensions. It can be described using Carreau-Yasuda Model which relates reduction in viscosity to shear rate²⁴.

$$\eta = \eta_0(1 + (\dot{\Gamma}\tau)^a)^{\frac{n-1}{a}} \quad \text{-----} \quad (3.2)$$

Where, $\dot{\Gamma}$ is the shear rate, τ is characteristic shear thinning time and n is an exponent of the power law region of shear thinning and should be between 0 and 1, a is parameter that characterizes the transition from the Newtonian region to the power law. The shear rate in our experiments is given by $\dot{\Gamma} = \frac{A_0}{d}\omega + \frac{rv}{2d^2}$. The term $\frac{rv}{2d^2}$ is due to the rate of water squeeze out and depends on the speed v with which we bring the tip towards the surface⁸. Eqn 3. 2 becomes

$$\frac{\Delta\eta}{\eta} \propto \frac{\Delta\gamma}{\gamma} = \left(1 + \left(\tau\left(\frac{A_0}{d}\omega + \frac{rv}{2d^2}\right)\right)^a\right)^{\frac{n-1}{a}} \quad \text{-----} \quad (3.3)$$

We replace d by $d+b$ in eqn 3.3 to include slippage ($b \neq 0$) in Carreau-Yasuda model.

$$\frac{\Delta\eta}{\eta} \propto \frac{\Delta\gamma}{\gamma} = \left(1 + \left(\tau\left(\frac{A_0}{d+b}\omega + \frac{rv}{2(d+b)^2}\right)\right)^a\right)^{\frac{n-1}{a}} \quad \text{-----} \quad (3.4)$$

The relative change in dissipation measured experimentally can be related to the viscosity since the tip-geometry remains the same. We fit the expression on the right-hand side of 3.1, 3.3 and 3.4 with the measured reduction in dissipation coefficient given by eqn 2.18 (Chapter-2)

3.2.3 Sample preparation

Water is confined between the substrates of different wettability and a fibre tip. The fibre tip having diameter $\approx 50\text{nm}$ is prepared by pulling the single mode optical fibre in fibre-puller having a CO₂ laser and was imaged using Scanning Electron Microscope (SEM) as shown in inset of Fig. 3.1.(Sutter Instrument Co. P2000). Contact angle measurements were performed to measure wettability of the substrates. We used five different substrates, mica ($\theta = 5^\circ$), Silicon Carbide, SiC($\theta = 42^\circ$), Aluminium Oxide, Al₂O₃ ($\theta = 55^\circ$), Lanthanum Oxide, LaO ($\theta = 65^\circ$) and Hydrogen terminated silicon ($\theta = 75^\circ$). Mica is freshly cleaved with scotch tape and then placed in the liquid cell. The liquid cell was immediately filled with MilliQ water. Single crystals of SiC, Al₂O₃, and LaO were first rinsed with ethanol followed by sonication in ethanol and Milli-Q water for 10 minutes each. Hydrogen-terminated Silicon substrate is prepared by dipping single crystal Si substrate in Hydrogen Fluoride (HF) solution for 5-10 minutes to terminate surface with hydrogen and rinsed with water. Each substrate is kept in MilliQ water for few hours to equilibrate before the experiments.

3.3 Results

Fig. 3.2 (a) and 3.2 (b) shows the measured amplitude of the tip-bearing prong versus separation. For a wetting substrate (mica) the amplitude starts to increase below 10 nm and for non-wetting substrate (SiH) below 25 nm. Qualitatively, the data indicate reduced dissipation under confinement. The data shown here is representative. Typically more than 50 measurements are performed on each substrate in a range of frequency (10 -15 KHz) and amplitude (0.5 -1 nm).

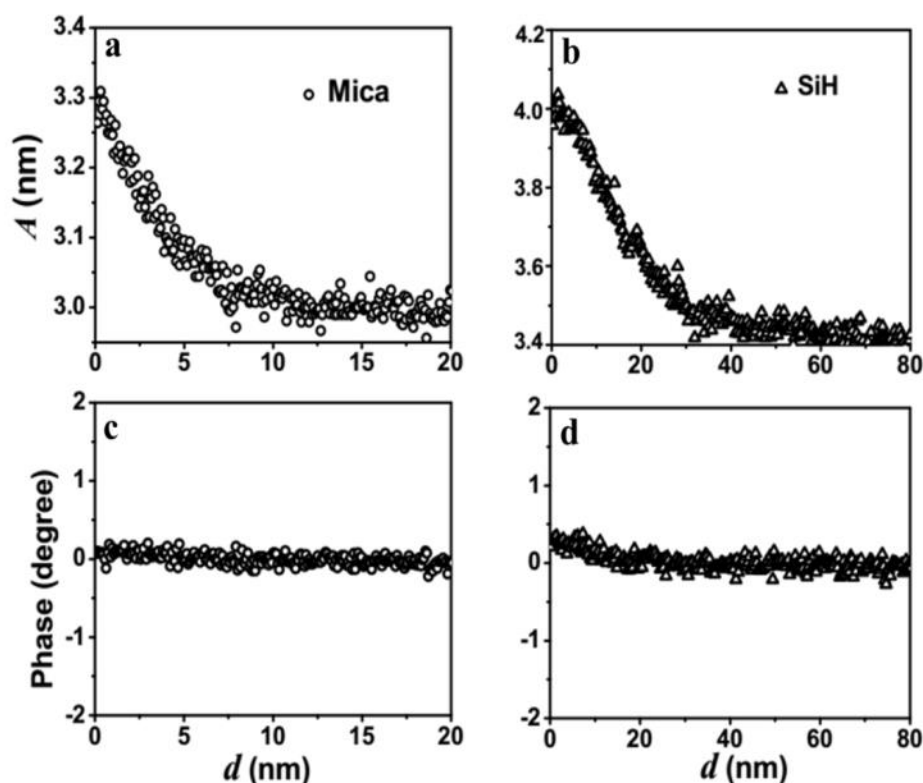


Fig. 3.2 The measurement of change in oscillation amplitude as the tip approaches the surface of (a) mica and (b) hydrogen-terminated Si surface, and corresponding phase value in (c) and (d).

Fig. 3.3 (a) and (b) show relative change in dissipation calculated from data in 3.2 (a), (b), (c) and (d) using equation 2.18 (chapter 2). The dissipation under confinement is reduced compared to the dissipation in bulk. This reduction is 10 %. Note that this 10 % change is compared to the dissipation due to the entire tip. The entire tip area is roughly is $\approx 10^{-7} \text{ m}^2$; the area at the end of the tip which serves as one of the confining surfaces is $\approx 10^{-15} \text{ m}^2$. The change in dissipation is entirely due to an altered flow response of water molecules beneath the tip which is referred to as nanoconfined. This change is 10% of the total dissipation due to macroscopic tip moving in the bulk water. It shows that the altered flow response due to confinement is quite significant.

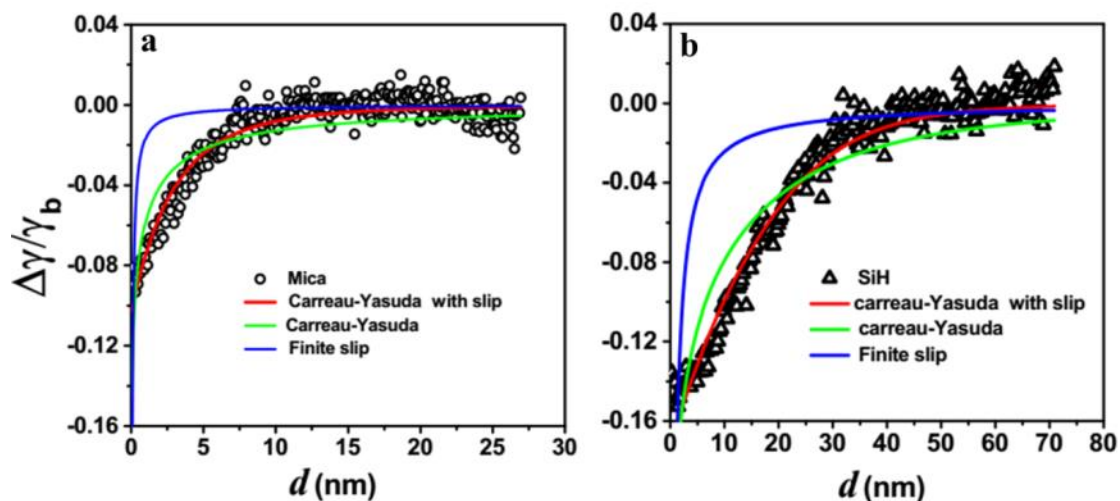


Fig. 3.3 The measurement of change in dissipation as the tip approaches the surface of (a) mica and (b) hydrogen-terminated Si surface. The open circles and triangles are experimental data, and continuous lines are fits of various models. Blue line — finite slip and no change in water viscosity, Greenline — viscosity changes as per the Carreau–Yasuda rule without slippage and redline—the modified Carreau–Yasuda with finite slippage. Clearly, the modified Carreau-Yasuda fits better than other two models for both wetting (mica - $\theta \approx 5$) and non-wetting surfaces (SiH - $\theta \approx 75$).

Table 3.1 shows all the fit parameters of fitting eqn (3.4) to experimental data. The fitting exercise shows that the dynamics under confinement is characterized by both nonlinear rheological response akin to complex fluids and finite slippage at the boundary. The relevant fit parameters for different wettability are plotted in fig 3.4.

In the following, we explore the possible reasons behind the reduction in dissipation when water is confined beneath it. If the no-slip boundary is violated retaining the viscosity to bulk value, the slippage can result in reduced viscous drag. The other possibility is shear thinning. Here, the change can be related to an altered viscosity which depends on shear rate. The observed dissipation reduction can also be attributed to the combined effect of shear thinning and finite slippage. All three possible scenarios are discussed in details in the section "Methods".

We use models to fit experimental data given by eqn's 3.1, 3.3 and 3.4. The continuous green line is fit of Carreau Yasuda model of shear thinning to the data given by eqn 3.3. The continuous blue line represents finite slippage described by eqn 3.1. The red line is modified Carreau-Yasuda to include finite slip. The comparison between three fits clearly shows that the observed dissipation can be attributed to both the nonlinear rheological

response of shear thinning at high shear rates (10^6s^{-1}) and finite slippage at the boundary. To elucidate the role of surface wettability on the dynamics of water confined at the nanoscale, we repeated the measurements on five substrates with different degree of wettability characterized by the contact angle (data not shown). We used mica ($\theta= 5^\circ$), Silicon Carbide, SiC($\theta= 42^\circ$), Aluminium Oxide, Al_2O_3 ($\theta= 55^\circ$), Lanthanum Oxide, LaO ($\theta= 65^\circ$) and Hydrogen terminated silicon ($\theta= 75^\circ$). In all these measurements it is seen that the modified Carreau-Yasuda with finite slippage fits better than pure shear thinning or pure slippage.

Fig. 3.4(b) shows a plot of characteristic shear thinning time-scale for different substrates. It is plotted versus the contact angle. The τ varies from 28 to 64 μs for wetting to non-wetting surfaces, a two fold increase. The slip length for substrates with different wettability follows a expected trend. The slip progressively increases from, less than 1.5nm for wetting (mica), to 12 nm for non-wetting substrates (Si-H), a six fold increase. The fitting of modified Carreau-Yasuda model to the experimental data successfully separates the effect of surface wettability on the dynamics under confinement. Moreover, The characteristic shear thinning time-scale matches well with other similar observations wherein, the dynamics of water condensed over a wetting substrate is probed with on-resonance method²⁵.

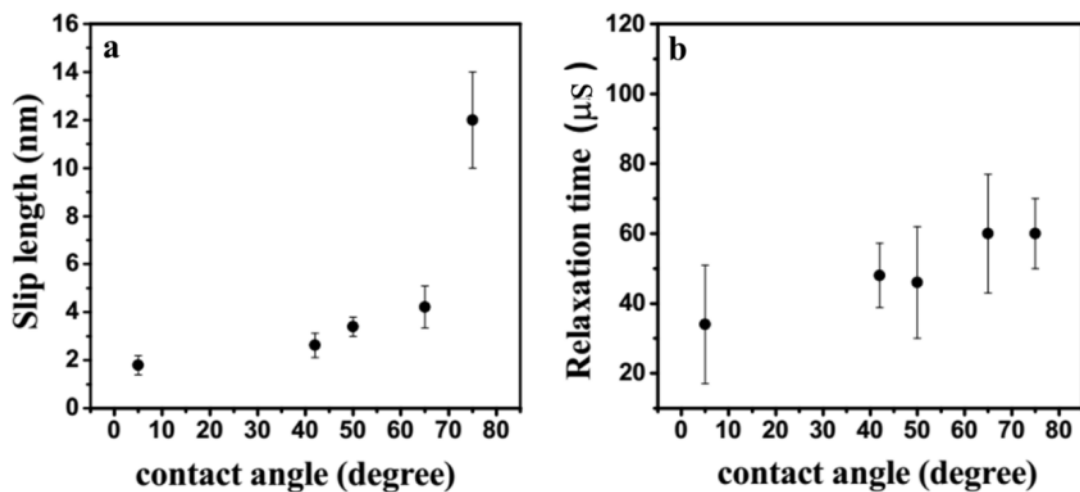


Fig. 3.4 (a) The slip length b versus the contact angle for five different substrates. The slip length is below 2 nm for a wetting substrate such as mica ($\theta = 5^\circ$) and reaches above 12 nm for SiH ($\theta = 75^\circ$). (b) The characteristic shear thinning time scale for all substrates. There is no appreciable change over contact angles from $\theta = 5^\circ$ to 75° .

Table 3.1 Fit parameters obtained on five substrates for Carreau–Yasuda model with finite slippage.

Substrate	τ (μs)	L_s (nm)	n	a
Mica (5°)	28 ± 15	1.5 ± 0.4	0.77 ± 0.16	2.3 ± 0.5
SiC (42°)	48 ± 9	2.6 ± 0.5	0.75 ± 0.06	2.9 ± 0.7
Al ₂ O ₃ (55°)	45 ± 16	3.2 ± 0.4	0.76 ± 0.07	2.5 ± 0.5
LaO (65°)	49 ± 16	5 ± 0.8	0.8 ± 0.1	2.9 ± 1.1
SiH (75°)	64 ± 5	12 ± 2	0.89 ± 0.02	2.5 ± 0.3

3.4 Discussions

Li et al. measured the viscosity of nanoconfined water to be several orders of magnitude higher than bulk⁶. On the contrary, the measurement by Raviv and Klein suggested that water viscosity under confinement remains close to bulk or increases by three times the bulk viscosity⁷. Our novel dynamic shear measurement method concludes that dissipation offered by the water confined under the tip is reduced. The change is 10 % of the tip-dissipation. It indicates that, Although dissipation reduces under confinement due to shear thinning and finite slip with a characteristic time-scale of μs , the reduction is close to 10 percent of the bulk dissipation experienced by the macroscopic tip. The characteristic shear thinning time-scale is roughly of the same order as Maxwell's relaxation previously measured¹².

The nanofluidic measurements on the flow of water suggest that water viscosity increases slightly in hydrophilic channels^{3,4}. The flow through carbon nanotubes (hydrophobic channels), on the other hand, is four to five orders faster than the one expected from fluid dynamic equations. The permeability through membranes is shown to enhance with a decrease in pore size¹⁹. The reasons behind such rapid flow are mostly unknown and are usually attributed to enormous slippage at the boundary¹. Here we show that not only slip is responsible for enhanced flow but shear thinning also plays a significant role. Our measurements imply that flow through nanochannels can be complex and may result in more substantial flux with reduced viscosity under high shear rates. The flow rate will be determined by both, the phenomenon of shear thinning and the slippage at the boundary that depends on the wettability of confining surfaces.

The existence of slip has been historically debated²¹. In 1845, G. Stokes, based on the experiments at the time and his calculations concluded that no-slip boundary condition is valid for all flows. In recent years, the attempts are being made to determine slip from fitting Reynold's equation to hydrodynamic drag experienced by a sphere in front of the plane using

AFM. It has resulted in contradictory findings of the existence of slip²¹⁻²³. In small-amplitude AFM measurements of squeeze-out dynamics, the conclusion regarding slip could not arrive at⁸. Ortiz-Young et al. have fitted oscillatory shear data using an AFM to a model based finite slip²⁰. The measurements on wetting ($\theta \approx 0^\circ$), intermediate ($\theta = 50^\circ$) and non-wetting ($\theta = 90^\circ$) samples in our study conclude that although slip length is close to zero for thoroughly wetting surfaces, it takes values of the order of 10 nm for non-wetting surfaces. This finding may play a crucial role in determining the discharge of water through carbon nanotubes or hydrophilic nanochannels.

Shear thinning is commonplace in binary mixtures, polymer melts, and colloidal suspensions. Its existence in case of pure water confined to small dimensions is puzzling. It is usually attributed to forming and breaking of flow-induced microstructures²⁶. Recently, shear thinning was shown to have entropic origins by directly imaging the suspension with fast confocal microscopy²⁷. At the moment, it is difficult to point out sources of shear thinning of pure liquids under nano-confinement. Further experiments planned in our laboratory to simultaneously measure stress and diffusion using optical spectroscopy could provide a molecular level explanation of the phenomenon observed here.

Shear thinning has been observed for dodecane liquid in confinement²⁸. Clear and quantitative evidence of shear thinning in case of nanoconfined water reported here suggests a general resemblance in behavior between organic solvents (non-polar, non-associative) and water (polar and associative). These were thought to behave differently under nano-confinement in the past⁷. Indeed, the flow through carbon nanotubes also shows faster flow rates for both water and organic solvents¹. This hints at a need for a general understanding of reasons behind nonlinear rheological response of pure liquids under nano-confinement.

It has been argued that reduction in water viscosity as opposed to the enhanced viscosity of organic solvents under confinement is due to the breaking of hydrogen bonds in water under confinement. Our normal stiffness and damping measurements in the past have shown that the polar water and OMCTS behave similarly under confinement and both show dynamic solidification^{11,29}. The slow-down in dynamics from ps to more than μ s is suggested to be arising out of criticality of nanoconfined water related to a second-order phase transition of capillary condensation concerning pore size¹². We emphasize a need for simultaneous spectroscopic and stress measurement for divulging the molecular origins of slow relaxation and reduced dissipation in nanoconfined water.

3.5 Conclusions

In summary, we have performed dynamic shear measurement on water confined between a sharp tip and substrates of different wettability. We explain the experimental observation of a reduction in dissipation under confinement with the help of Carreau-Yasuda model of shear thinning and/or finite slippage at the boundary.

We found a clear evidence for shear thinning along with finite slippage for both wetting as well as non-wetting substrates. The slip length extracted from the fit procedures progressively increase for non-wetting substrates. On the contrary, the shear thinning time scale does not vary appreciably over five substrates with different degree of wettability. The method allows the separation of contributions arising out of surface wettability and slow-down in molecular dynamics. The findings have relevance in understanding the flow in nanofluidics and explaining rapid transit of water through carbon nanotubes reported earlier.

References

- (1) Majumder, M.; Chopra, N.; Andrews, R.; Hinds, B. Enhanced Flow in Carbon Nanotubes. *Nature* **2005**, *438*, 44.
- (2) Hille, B. *Ion Channels of Excitable Membranes*; Sinauer Associates, Inc., 2001.
- (3) Tas, N. R.; Haneveld, J.; Jansen, H. V.; Elwenspoek, M.; Van Den Berg, A. Capillary Filling Speed of Water in Nanochannels. *Appl. Phys. Lett.* **2004**, *85*, 3274–3276.
- (4) Sobolev, V. D.; Churaev, N. V.; Velarde, M. G.; Zorin, Z. M. Surface Tension and Dynamic Contact Angle of Water in Thin Quartz Capillaries. *J. Colloid Interface Sci.* **2000**, *222*, 51–54.
- (5) Zhu, Y.; Granick, S. Viscosity of Interfacial Water. *Phys. Rev. Lett.* **2001**, *87*, 096104.
- (6) Li, T. De; Gao, J.; Szoszkiewicz, R.; Landman, U.; Riedo, E. Structured and Viscous Water in Subnanometer Gaps. *Phys. Rev. B - Condens. Matter Mater. Phys.* **2007**, *75*, 1–6.
- (7) Raviv, U.; Laurat, P.; Klein, J. Fluidity of Water Confined to Subnanometre Films. *Nature* **2001**, *413*, 51–54.
- (8) Khan, S. H.; Kramkowski, E. L.; Ochs, P. J.; Wilson, D. M.; Hoffmann, P. M.

- Viscosity of a Nanoconfined Liquid during Compression. *Appl. Phys. Lett.* **2014**, *104*.
- (9) Li, T.-D.; Riedo, E. Nonlinear Viscoelastic Dynamics of Nanoconfined Wetting Liquids. *Phys. Rev. Lett.* **2008**, *100*, 106102.
- (10) Jeffery, S.; Hoffmann, P. M.; Pethica, J. B.; Ramanujan, C.; Özer, H. Ö.; Oral, A. Direct Measurement of Molecular Stiffness and Damping in Confined Water Layers. *Phys. Rev. B* **2004**, *70*, 054114.
- (11) Khan, S. H.; Matei, G.; Patil, S.; Hoffmann, P. M. Dynamic Solidification in Nanoconfined Water Films. *Phys. Rev. Lett.* **2010**, *105*, 106101.
- (12) Kapoor, K.; Amandeep; Patil, S. Viscoelasticity and Shear Thinning of Nanoconfined Water. *Phys. Rev. E* **2014**, *89*, 013004.
- (13) Kageshima, M. Layer-Resolved Relaxation Dynamics of Confined Water Analyzed through Subnanometer Shear Measurement. *EPL* **2014**, *107*, 66001.
- (14) Sansom, M. S. P.; Biggin, P. C. Water at the Nanoscale. *Nature* **2001**, *414*, 156–159.
- (15) Granick, S.; Bae, S. C. A Curious Antipathy for Water. *Science* **2008**, *322*, 1477–1478.
- (16) Finney, J. L. Overview Lecture. Hydration Processes in Biological and Macromolecular Systems. *Faraday Discuss.* **1996**, *103*, 1–18.
- (17) Scherge, M.; Li, X.; Schaefer, J. A. The Effect of Water on Friction of MEMS. *Tribol. Lett.* **1999**, *6*, 215–220.
- (18) Cohen-Tanugi, D.; Grossman, J. C. Water Desalination across Nanoporous Graphene. *Nano Lett.* **2012**, *12*, 3602–3608.
- (19) Lee, B.; Baek, Y.; Lee, M.; Jeong, D. H.; Lee, H. H.; Yoon, J.; Kim, Y. H. A Carbon Nanotube Wall Membrane for Water Treatment. *Nat. Commun.* **2015**, *6*, 7109.
- (20) Ortiz-Young, D.; Chiu, H. C.; Kim, S.; Voitchovsky, K.; Riedo, E. The Interplay between Apparent Viscosity and Wettability in Nanoconfined Water. *Nat. Commun.* **2013**, *4*.
- (21) Neto, C.; Evans, D. R.; Bonaccorso, E.; Butt, H. J.; Craig, V. S. J. Boundary Slip in Newtonian Liquids: A Review of Experimental Studies. *Reports Prog. Phys.* **2005**, *68*,

- 2859–2897.
- (22) Bonaccorso, E.; Butt, H. J.; Craig, V. S. J. Surface Roughness and Hydrodynamic Boundary Slip of a Newtonian Fluid in a Completely Wetting System. *Phys. Rev. Lett.* **2003**, *90*, 4.
 - (23) Honig, C. D. F.; Ducker, W. A. No-Slip Hydrodynamic Boundary Condition for Hydrophilic Particles. *Phys. Rev. Lett.* **2007**, *98*, 028305.
 - (24) Byron Bird, R.; Carreau, P. J. A Nonlinear Viscoelastic Model for Polymer Solutions and Melts—I. *Chem. Eng. Sci.* **1968**, *23*, 427–434.
 - (25) Kim, B.; Kwon, S.; Lee, M.; Kim, Qh.; An, S.; Jhe, W. Probing Nonlinear Rheology Layer-by-Layer in Interfacial Hydration Water. *Proc. Natl. Acad. Sci.* **2015**, *112*, 15619–15623.
 - (26) Vermant, J.; Solomon, M. J. Flow-Induced Structure in Colloidal Suspensions. *J. Phys. Condens. Matter* **2005**, *17*, 187–216.
 - (27) Xiang Cheng; Jonathan H. McCoy; Jacob N. Israelachvili; Itai Cohen. Imaging the Shear Thinning and Thickening in Colloidal Suspensions. *Science* **2011**, *333*, 1276–1280.
 - (28) Granick, S. Motions and Relaxations of Confined Liquids. *Science* **1991**, *253*, 1374–1379.
 - (29) Patil, S.; Matei, G.; Oral, A.; Hoffmann, P. M. Solid or Liquid? Solidification of a Nanoconfined Liquid under Nonequilibrium Conditions. *Langmuir* **2006**, *22*, 6485–6488.

Chapter 4

Flow Properties of Non-polar Liquids

4.1 Introduction

Understanding the flow properties of the liquid in confined pores at the nanoscale is essential for many areas such as interfacial adhesion and friction^{1,2}, filtration^{3,4}, molecular transport in nanostructures⁵⁻⁷ lubrication in nanoelectromechanical systems (NEMS)⁸ and enhanced oil recovery^{9,10}. Liquids, when confined between two surfaces that are tens of nanometers apart, exhibit unique structural, dynamic, and mechanical properties which are significantly different from those observed in bulk¹¹⁻¹⁸. Researchers have reported that liquids under nanoconfinement show density oscillations near the solid walls^{19,20}, enhanced effective shear viscosity,^{21,22} prolonged relaxation time²³, transition to dynamic solidification²⁴⁻²⁶, reduced diffusion coefficient²⁷, and nonlinear rheological response under shear²⁸⁻³⁰. There are various factors which determine the behavior of confined liquids such as the degree of confinement, applied shear rates, interactions at the solid-liquid interface, quench rates, molecular structure, and chemical nature.

Examining flow behaviour of non-polar liquids in confined pores can play an important role in the field of enhanced oil recovery^{9,10} and lubrication⁸. In literature, the shear response of organic solvents such as Octamethylcyclotetrasiloxane (OMCTS), alkanes, tetrakis (2-ethylhexoxy) silane (TEHOS) is measured using techniques such as Surface Force Apparatus (SFA) and Atomic Force Microscope (AFM). Typically, shear measurements using SFA^{23,31-33} are done at low frequency (1Hz – 100Hz) and large shear amplitudes (1µm – 5 µm) while AFMs reached larger shear frequencies (100 Hz – 1000 Hz) but limited to small amplitude. In the past, it is reported that liquids under confinement exhibit rheological response under confinement and it is important to measure their shear rate dependent response^{28,34,35}.

In the previous chapter, we investigated the effect of surface wettability on flow properties of water under confinement. We provided a method to separate the impact of shear-thinning resulting from shearing a slowly relaxing microstructure and finite slippage at

the boundary. Here, We measured the shear response of non-polar liquids such as OMCTS and TEHOS and compared it with a polar liquid such as water under high shear rates (10^6 s^{-1}) by employing large shear frequencies [10 kHz-15 kHz] and small oscillation amplitude (1nm-3nm). Recently, we have measured dissipation in a 5 nm thick films of water at high shear rates, and it was found to decrease with a degree of confinement^{28,34,35} progressively. Using the same methodology, we determined and compared dissipation for polar and non-polar liquids under confinement.

We measure dissipation coefficient of a tip oscillating in liquids close to ($d < 10 \text{ nm}$) to an atomically flat mica substrate. It reduces with separation for both polar (water) and nonpolar (OMCTS, TEHOS) liquids confined to the nanoscale. We attribute this reduction in dissipation to shear thinning by fitting Carreau-Yasuda model with finite slip. The fit procedure yields characteristic shear thinning time for water of $28 \pm 15 \mu\text{s}$. For OMCTS and TEHOS it is 176 ± 18 and $256 \pm 180 \mu\text{s}$ respectively. We found that the nonpolar liquids exhibit more considerable slip lengths compared to polar liquid (water). This difference can be attributed to a lesser wettability of mica concerning these liquids. We claim that our model could separate out the effect of confinement and substrate from the rheological response exhibited by liquid at nano-confinement. We qualitatively explain the observed rheological response of both polar and nonpolar liquids confined to nanoscale by suggesting that it is a system poised close to a criticality such as capillary condensation.

4.2 Materials and Methods

Measurement for liquids under confinement was performed using a home built quartz tuning fork based oscillatory shear Rheometer³⁶ as shown in Fig. 4.1. A silica fibre tip was prepared by pulling the single mode optical fibre in fibre puller by heating with the CO_2 laser (Sutter Instrument, CA, USA). A fiber tip having a diameter of 50nm was fixed to the free prong of quartz tuning fork which acts as a shear force sensor. Quartz tuning fork is piezoelectric in nature, and the current signal generated by tuning fork is proportional to the differential amplitude of its prongs. At resonance frequency, both the prongs move out of phase and have maximum differential amplitude. At off-resonance frequency, both the prongs move in phase with a similar amplitude which results in zero differential bending between the prongs. Hence, the current value through electrodes is zero. The tip bearing prong experiences excess viscous dissipation as the fiber tip gets immersed in liquid. It produces differential bending in prongs and results in a finite current through the electrodes. This current is proportional to

viscous dissipation on the tip. The fluid was confined between the substrate placed in a liquid cell and fiber tip as shown in Fig. 4.1. The sample stage was approached towards the fiber tip with the help of auto actuation stage.

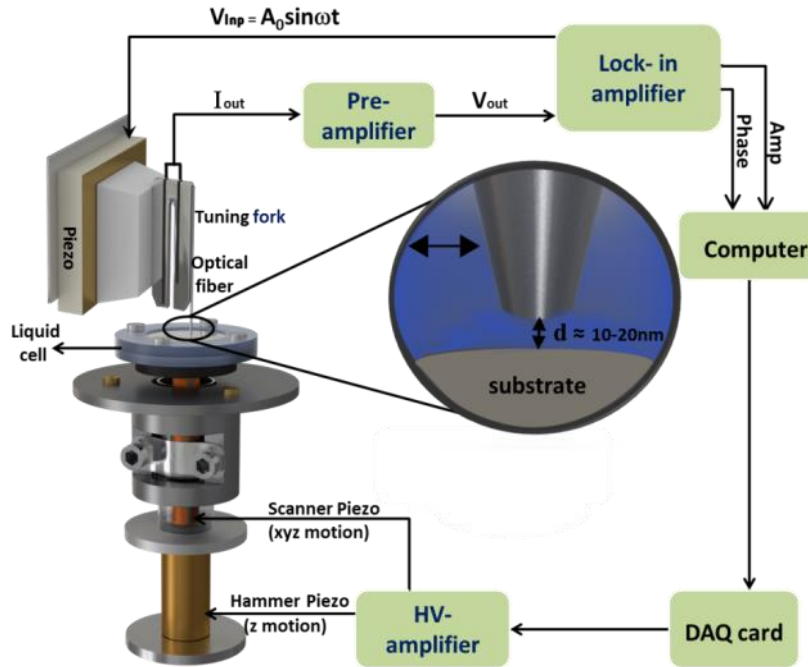


Fig. 4.1 Schematic of experimental setup. Liquid confinement takes place between optical fiber attached to the free prong of tuning fork and substrate below as shown in the inset. A tuning fork acts as a force sensor and change in current is measured during the confinement. This current is a measure of dissipation of confining liquid.

Freshly cleaved mica was used as one of the confining substrates. For determining the wettability of the substrate, the contact angle of all liquids was measured on a freshly cleaved mica substrate. The contact angle of water, OMCTS and TEHOS were $5^{\circ} \pm 0.5^{\circ}$, $20^{\circ} \pm 0.4^{\circ}$ and $30^{\circ} \pm 0.4^{\circ}$ respectively. The substrate was placed in a liquid cell and immediately filled with liquids for performing further experiments. MilliQ water having resistance value $18\text{M}\Omega$ was used in experiments. OMCTS was stored with molecular sieves overnight and filtered through $0.2\ \mu\text{m}$ pore size filter before measurement. TEHOS was used as purchased. All the experiments were performed in ambient conditions

The current signal which is proportional to amplitude is measured as the distance between confining surfaces is varied. Afterward, the amplitude and phase lag of tip bearing prong from the drive was calculated from current signal. Then, dissipation was determined

from the amplitude and phase value. The expression for evaluating dissipation coefficient is given as follow.

$$\gamma = k \frac{A_0}{A} \sin\phi \quad \text{----} \quad (4.1)$$

Where A_0 is free amplitude without dissipation which is equal to drive amplitude, ϕ is phase lag between the drive and tip amplitude in presence of dissipating medium. All measurements were performed in the frequency range of 10-15 kHz and oscillation amplitude 1-3 nm.

4.3 Models

The observed decrease in the dissipation near substrate ($d < 10$ nm) as compared bulk was modeled with a) finite slip at the boundary, b) Carreau-Yasuda model for shear thinning and c) shear thinning with finite slip. The details regarding these models are as follow:

4.3.1 Finite slippage

The observed reduction in dissipation can also be attributed to the violation of no-slip boundary condition with no change in intrinsic viscosity of the liquid. The slippage is characterized by slip-length L_s , where the slip is extrapolated to be zero inside the solid wall. The shear stress experienced from the fluid is described by the product of viscosity and shear rate, *i.e.* “ $A_0\omega/d$ ” where, A_0 is bulk oscillation amplitude, d is the distance between the confining substrates and ω is oscillation frequency. The altered shear rate in the presence of slip length will be “ $A_0\omega/d+L_s$ ”. The ratio of shear rates then gives the ratio of dissipative forces for slip and no-slip boundary. The relative change in dissipation concerning bulk is given by,

$$\frac{\Delta\gamma}{\gamma} = \frac{d}{d+L_s} - 1 \quad \text{----} \quad (4.2)$$

4.3.2 Carreau-Yasuda Shear thinning model

The Carreau-Yasuda model³⁷ captures the shear rate dependent viscosity of nonlinear liquids.

$$\frac{\eta}{\eta_0} = \left[1 + (\dot{\gamma}\tau)^a \right]^{\frac{n-1}{a}} \quad \text{-----} \quad (4.3)$$

Where η is viscosity at confinement, η_0 is bulk viscosity. $\dot{\Gamma}$ is shear rate and is given by the relation $\dot{\Gamma} = \frac{A_0\omega}{d} + \frac{rv}{2(d)^2}$. In this expression ω is oscillation frequency, A_0 is drive amplitude in bulk liquid, r is the radius of fiber tip, and v is approach velocity of fiber tip towards the substrate. τ is a characteristic time of shear thinning. The first term in shear rate is $A_0\omega/d$ which corresponds to shear rate due to shear oscillation of fiber tip parallel to the substrate, and rv/d^2 corresponds to shear rate due to squeezing out of fluid between the tip and substrate as the tip approaches the substrate. The shear rate generated due to rv/d^2 is three orders of magnitudes smaller than $A_0\omega/d$ and can be ignored. The relative change in dissipation measured experimentally can be related to the viscosity since the tip-geometry remains the same, $\Delta\eta/\eta = \Delta\gamma/\gamma$. The final expression of Carreau-Yasuda shear thinning model can be stated as follow:

$$\frac{\Delta\gamma}{\gamma} = \left[1 + \left(\frac{A_0\omega\tau}{d} \right)^a \right]^{\frac{n-1}{a}} - 1 \quad \text{----} \quad (4.4)$$

4.3.2 Combined shear thinning with finite slippage

The other possibility of reduction of dissipation under confinement could be due to the combined effect of both boundary slippage ($L_s \neq 0$) and shear thinning. The boundary slippage effect can be included in shear thinning model by replacing the distance “d” by “d+L_s.” The model consisting of shear thinning as well boundary slippage effect is as follows:

$$\frac{\Delta\gamma}{\gamma} = \left[1 + \left(\frac{A_0\omega\tau}{d+L_s} \right)^a \right]^{\frac{n-1}{a}} - 1 \quad \text{----} \quad (4.5)$$

4.4 Results

The amplitude of the tip bearing prong versus distance (d) between the tip and the substrate is shown in Fig 4.2(a), (b) and (c) for water, OMCTS and TEHOS respectively. The amplitude increases, while the tip approaches substrate and gap, was progressively decreased. We observed that the amplitude starts to increase below 10 nm separation for all liquids. Fig 4.2 (d), (e) and (f) show correspondingly phase lag between the drive and vibrating tip bearing prong in water, OMCTS and TEHOS. In case of water, the phase value did not vary under

confinement, but for OMCTS and TEHOS the phase changes were observed but not appreciably large as the tip approached within 10 nm distance from the substrate.

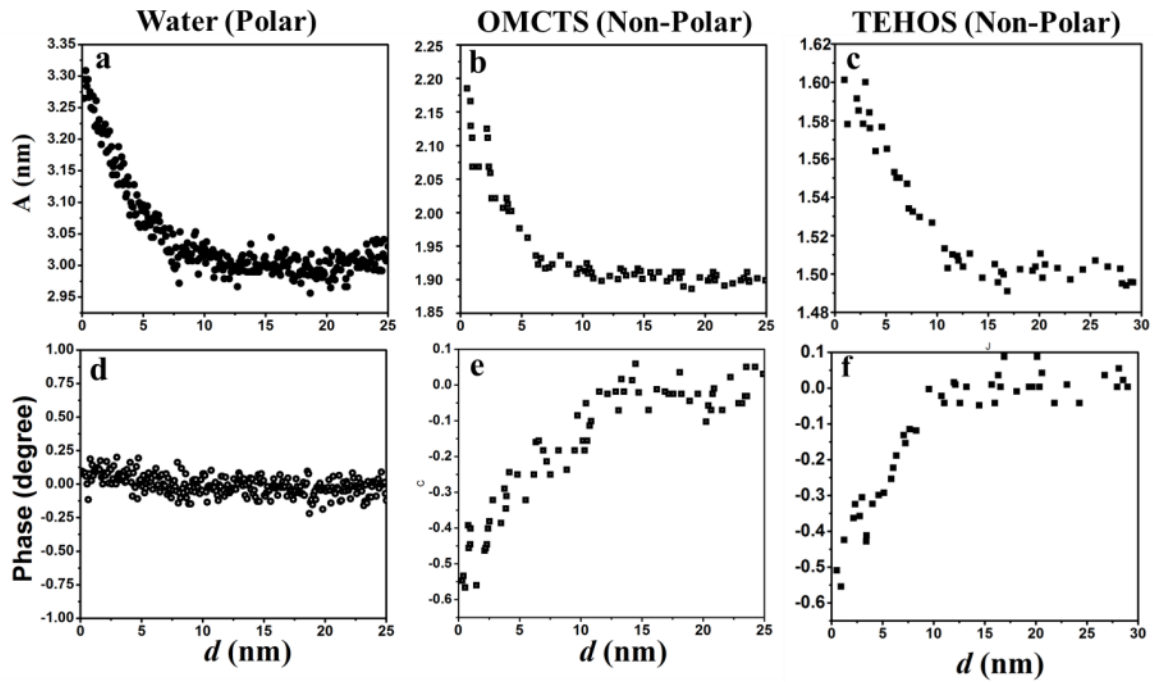


Fig. 4.2 Amplitude and Phase value of tuning fork prong oscillating at the off-resonance frequency. Amplitude shows the deviation from bulk behavior at $d = 5\text{ nm}$ for water (a) and $d = 10\text{--}12\text{ nm}$ for OMCTS (b) and TEHOS (c), the Corresponding phase is shown in (d), (e) and (f). Amplitude is evaluated from measured current signal and phase value from lock-in amplifier at a fixed frequency. All details are provided elsewhere³⁶.

We used eqn (4.1) for computing the relative change in dissipation coefficient for all the measurements on water, OMCTS, and TEHOS. Fig 4.3(a),(b) and (c) show estimated relative changes in dissipation under confinement from amplitude and phase value for water, OMCTS, and TEHOS respectively. We observed that dissipation coefficient decreases by 10% for both polar and non-polar liquids under confinement. Note that this 10% change is compared to dissipation due to entire tip. This shows that it is an appreciable change in dissipation coefficient. More than 20 measurements were performed on each liquid in a range of frequencies of 10–15 kHz, and oscillation amplitudes of 1–3 nm.

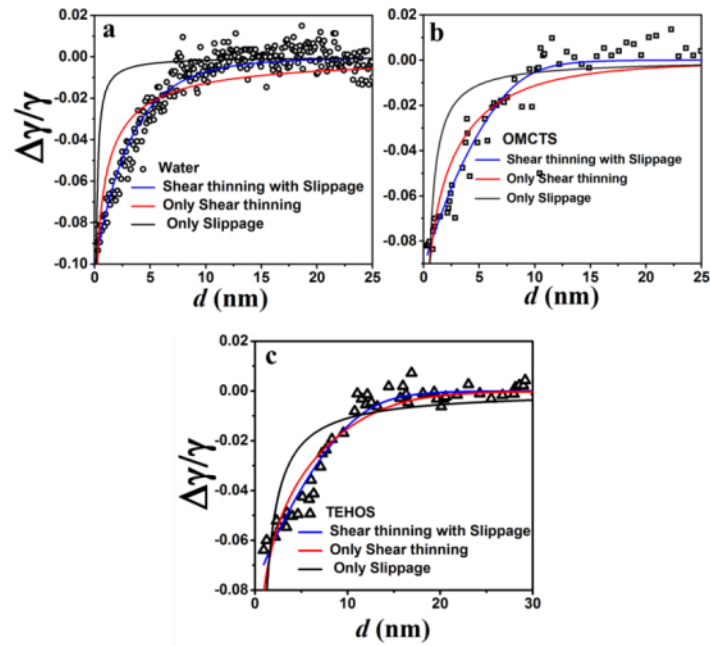


Fig. 4.3 Relative change in dissipation coefficient of confining liquid in comparison to its bulk value for water (a), OMCTS (b) and TEHOS (c). This decrease in dissipation coefficient is modeled by three different eqn's (4.2), (4.4) and (4.5). It is best fitted by the combined effect of shear thinning and finite slippage. Fitting parameters of the corresponding model are listed in Table 4.1.

In this section, we discuss possible reasons behind the reduction in dissipation coefficient exhibited by confined liquids. First, a possible reason is if No-slip boundary condition gets violated, then slippage leads to reduced viscous dissipation with no change in viscosity of the liquid. The other possible reason is shear thinning wherein the viscosity is shear rate dependent. It relates the reduction in viscous dissipation to shear rates. It can only take place if shear rates are larger than the inverse of relaxation of liquid. The third possibility is combined effect of shear thinning and slip length. Reduction in dissipation coefficient was fitted to models describing above-mentioned three different physical scenarios given by eqn's (4.2), (4.4), and (4.5). The fits are shown in Fig. 4.3 (a), (b) and (c). The continuous black line is fit of slippage only given by eqn (4.2) which considers the role of the substrate. The continuous red line is a fit of Carreau-Yasuda model of shear thinning given by with eqn (4.4) which describes shear rate dependent viscosity. The continuous blue line is fit of Carreau-Yasuda model of shear thinning along with finite slippage given by eqn (4.5). The comparison between three fits clearly shows that the observed decrease in

dissipation coefficient is best described by the combined effect of shear thinning and finite slippage at the boundary.

The values of four fit parameters extracted from fitting dissipation data on different liquids are reported in Table 4.1. In Carreau-Yasuda model, n and a represent strength of shear thinning and transition from Newtonian to power law behavior respectively. The value of n did not alter much for water, OMCTS and TEHOS from each other and lies between 0 and 1. The value of τ characteristic shear thinning time extracted from the fit, whose values are $28 \pm 15 \mu\text{s}$, $179 \pm 18 \mu\text{s}$ and $252 \pm 18 \mu\text{s}$ for water, OMCTS and TEHOS respectively. It represents the slowdown in dynamics under confinement. The relaxation time of OMCTS, TEHOS is one order of magnitude higher than water. The slip length L_s increases with non-wettability of the substrate. For water, the slip length value is $1.5 \pm 0.5 \text{ nm}$ which is negligibly small. In case of, OMCTS, TEHOS the slip is 4.6 ± 1.1 and $9.0 \pm 1.4 \text{ nm}$ respectively.

Table 4.1 consists of the fitting parameter obtained by fitting model composed of the combined effect of shear thinning and finite slippage.

Liquid	n	a	τ (μs)	L_s (nm)
Water (5°)	0.77 ± 0.16	2.3 ± 0.5	28 ± 15	1.5 ± 0.4
OMCTS (20°)	0.91 ± 0.01	4.9 ± 1.4	179 ± 18	4.6 ± 1.1
TEHOS (30°)	0.89 ± 0.01	7 ± 1.2	253 ± 18	9.0 ± 1.4

We remark here that Carreau-Yasuda model for shear thinning with slip length describes the dynamics of both confined polar (water) and non-polar liquids (OMCTS, TEHOS) accurately captures. Moreover, Once again our study and model could separate out the confinement and substrate effect on behavior exhibited by liquid at nano-confinement irrespective of their chemical nature.

4.5 Discussion

Our measurements show a reduction in dissipation coefficient upon confinement for water, OMCTS, and TEHOS. The response to shear alters from that of bulk at approximately, $d = 10 \text{ nm}$. This reduction in dissipation was observed, and it is about 10% compared to the tip dissipation in respective bulk liquid. In literature, it is reported that confined fluid exhibits

different behavior from bulk^{12,38-40} at 1 to 2 nm, while the flow through nanochannels differed from bulk for channel radius of the order of 10-50 nm. Researchers have reported flux enhancement by five orders of magnitude for water flowing through a carbon nanotube or its membrane^{7,41,42}. It is possible that we can measure such variations from bulk behavior due to higher shear rates used in our work. In this context, it is required to relate the dissipation measurement in both shear and flow experiments.

In our previous work, we investigated the effect of substrate wettability on flow properties of nanoconfined water. We were able to separate the contributions from shear thinning and finite slip in an effective manner. The fitted slip lengths varied systematically with substrate wettability. In present work, we measured the response of liquids which differ in polarity and also having different wettability on same substrate *i.e.*, mica. It was confirmed by measuring their contact angle on the substrate. OMCTS ($20^{\circ} \pm 0.4^{\circ}$) and TEHOS ($30^{\circ} \pm 0.4^{\circ}$) have large contact angle in comparison to water ($5^{\circ} \pm 0.4^{\circ}$) on a mica substrate. In present case too, the reduction in dissipation was favored and fitted well to shear thinning with finite slip. The fit procedure has returned characteristic times, which are $179 \pm 8 \mu\text{s}$, $252 \pm 18 \mu\text{s}$ and $28 \pm 18 \mu\text{s}$ for OMCTS, TEHOS, and water respectively. The slip length value extracted from model fitting for OMCTS, TEHOS and water are $4.6 \pm 1.1\text{nm}$, $9.0 \pm 1.4 \text{ nm}$ and $1.5 \pm 0.5 \text{ nm}$ respectively. It shows that OMCTS and TEHOS exhibit larger slip which is consistent with their lower wettability as compared to water on mica. Once again, using previously derived methodology, we could separate out the effect of confinement and substrate wettability from the behavior exhibited by liquids at nano-confinement. This represents the robustness of our method built to explain the observed behavior of fluids under nano-confinement.

In our finding, we report relaxation time of OMCTS and TEHOS at nano-confinement are higher than water. These relaxation times are large in comparison to their bulk relaxation time. This enhancement in relaxation time represents the slow-down of dynamic in the confined state. These characteristic relaxation times are similar to those reported previously for OMCTS and TEHOS^{31,43,44}. OMCTS and TEHOS exhibited a larger relative increase of the relaxation time in comparison to water. This may reflect the better ordering of the larger and more “sluggish” OMCTS and TEHOS molecules³⁹.

Shear Thinning is observed in materials possessing a microstructure that is slowly relaxing. In measurements where shear rates are faster than the inverse of this relaxation,

shear thinning is observed. Typically such materials are complex liquids, such as polymer melts and whipped-cream. Our observation of shear thinning in nanoconfined liquids, both polar and nonpolar solvents, raises a question - what is the microstructure responsible for causing shear thinning in pure nanoconfined water? Many pure fluids such as Xenon have shown rheological response such as shear thinning and viscoelasticity in microgravity environments wherein layering under gravity is avoided. It is argued that fluids poised close to a critical phase transition have a microstructure whose relaxation can be as long as few seconds compared to picoseconds of the bulk fluid. We argue here that nanoconfined water is also close to such criticality. In case of confined liquids, it is not difficult to imagine a capillary condensation-like phase transition where high density and low-density liquids phases co-exist to produce a microstructure whose spatial expanse does not have to be too large since the size of the confinement is less than a few nm. This means that such a microstructure does not have to be larger than 2 or 3 molecules. We are planning to experimentally confirm the existence of such criticality by gaining optical access to the nanoconfined region.

In summary, we have measured rheological response of nanoconfined polar and non-polar liquids with unprecedented shear rates. The measurements reveal shear thinning with finite slippage effect at confining separations as large as few nms. The divergence of relaxation with reducing separation hints at a possible criticality in nanoconfined water and organic liquids.

References

- (1) Singer, I. L.; Pollock, H. M. *Fundamentals of Friction: Macroscopic and Microscopic Processes*; Springer Netherlands: Dordrecht, 1992; Vol. 27.
- (2) Bowden, F. P.; Tabor, D.; Freitag, E. H. *Fundamental of Friction on Solid*; Springer Berlin Heidelberg, 1959.
- (3) Cohen-Tanugi, D.; Grossman, J. C. Water Desalination across Nanoporous Graphene. *Nano Lett.* **2012**, *12*, 3602–3608.
- (4) Lee, B.; Baek, Y.; Lee, M.; Jeong, D. H.; Lee, H. H.; Yoon, J.; Kim, Y. H. A Carbon Nanotube Wall Membrane for Water Treatment. *Nat. Commun.* **2015**, *6*, 7109.
- (5) Sobolev, V. D.; Churaev, N. V.; Velarde, M. G.; Zorin, Z. M. Surface Tension and

- Dynamic Contact Angle of Water in Thin Quartz Capillaries. *J. Colloid Interface Sci.* **2000**, *222*, 51–54.
- (6) Tas, N. R.; Haneveld, J.; Jansen, H. V.; Elwenspoek, M.; van den Berg, A. Capillary Filling Speed of Water in Nanochannels. *Appl. Phys. Lett.* **2004**, *85*, 3274–3276.
- (7) Whitby, M.; Quirke, N. Fluid Flow in Carbon Nanotubes and Nanopipes. *Nat. Nanotechnol.* **2007**, *2*, 87–94.
- (8) Scherge, M.; Li, X.; Schaefer, J. A. The Effect of Water on Friction of MEMS. *Tribol. Lett.* **1999**, *6*, 215–220.
- (9) Green, D. W.; Willhite, G. P. *Enhanced Oil Recovery*; Elsevier, 1998.
- (10) Eremin, N. *Enhanced Oil Recovery Methods*; Russian Academy of Science, 2003.
- (11) Szoszkiewicz, R.; Riedo, E. Nucleation Time of Nanoscale Water Bridges. *Phys. Rev. Lett.* **2005**, *95*, 135502.
- (12) Antognozzi, M.; Humphris, A. D. L.; Miles, M. J. Observation of Molecular Layering in a Confined Water Film and Study of the Layers Viscoelastic Properties. *Appl. Phys. Lett.* **2001**, *78*, 300–302.
- (13) Jeffery, S.; Hoffmann, P. M.; Pethica, J. B.; Ramanujan, C.; Özer, H. Ö.; Oral, A. Direct Measurement of Molecular Stiffness and Damping in Confined Water Layers. *Phys. Rev. B* **2004**, *70*, 054114.
- (14) Major, R. C.; Houston, J. E.; McGrath, M. J.; Siepmann, J. I.; Zhu, X.-Y. Viscous Water Meniscus under Nanoconfinement. *Phys. Rev. Lett.* **2006**, *96*, 177803.
- (15) Uchihashi, T.; Higgins, M.; Nakayama, Y.; Sader, J. E.; Jarvis, S. P. Quantitative Measurement of Solvation Shells Using Frequency Modulated Atomic Force Microscopy. *Nanotechnology* **2005**, *16*, S49–S53.
- (16) Alcoutlabi, M.; McKenna, G. B. Effects of Confinement on Material Behaviour at the Nanometre Size Scale. *J. Phys. Condens. Matter* **2005**, *17*, R461–R524.
- (17) Scheidler, P.; Kob, W.; Binder, K. Cooperative Motion and Growing Length Scales in Supercooled Confined Liquids. *Europhys. Lett.* **2002**, *59*, 701–707.

- (18) Riedo, E.; Lévy, F.; Brune, H. Kinetics of Capillary Condensation in Nanoscopic Sliding Friction. *Phys. Rev. Lett.* **2002**, *88*, 185505.
- (19) Horn, R. G.; Israelachvili, J. N. Direct Measurement of Structural Forces between Two Surfaces in a Nonpolar Liquid. *J. Chem. Phys.* **1981**, *75*, 1400–1411.
- (20) Heuberger, M. Density Fluctuations Under Confinement: When Is a Fluid Not a Fluid? *Science* **2001**, *292*, 905–908.
- (21) Gee, M. L.; McGuiggan, P. M.; Israelachvili, J. N.; Homola, A. M. Liquid to Solidlike Transitions of Molecularly Thin Films under Shear. *J. Chem. Phys.* **1990**, *93*, 1895–1906.
- (22) Zhu, Y.; Granick, S. Superlubricity: A Paradox about Confined Fluids Resolved. *Phys. Rev. Lett.* **2004**, *93*, 096101.
- (23) Granick, S. Motions and Relaxations of Confined Liquids. *Science* **1991**, *253*, 1374–1379.
- (24) Bhushan, B.; Israelachvili, J. N.; Landman, U. Nanotribology: Friction, Wear and Lubrication at the Atomic Scale. *Nature* **1995**, *374*, 607–616.
- (25) Demirel, A. L.; Granick, S. Origins of Solidification When a Simple Molecular Fluid Is Confined between Two Plates. *J. Chem. Phys.* **2001**, *115*, 1498–1512.
- (26) Khan, S. H.; Matei, G.; Patil, S.; Hoffmann, P. M. Dynamic Solidification in Nanoconfined Water Films. *Phys. Rev. Lett.* **2010**, *105*, 106101.
- (27) Mukhopadhyay, A.; Zhao, J.; Bae, S. C.; Granick, S. Contrasting Friction and Diffusion in Molecularly Thin Confined Films. *Phys. Rev. Lett.* **2002**, *89*, 136103.
- (28) Li, T.-D.; Riedo, E. Nonlinear Viscoelastic Dynamics of Nanoconfined Wetting Liquids. *Phys. Rev. Lett.* **2008**, *100*, 106102.
- (29) Kageshima, M. Layer-Resolved Relaxation Dynamics of Confined Water Analyzed through Subnanometer Shear Measurement. *EPL* **2014**, *107*, 66001.
- (30) Kim, B.; Kwon, S.; Lee, M.; Kim, Qh.; An, S.; Jhe, W. Probing Nonlinear Rheology Layer-by-Layer in Interfacial Hydration Water. *Proc. Natl. Acad. Sci.* **2015**, *112*, 201515033.

- (31) Bureau, L. Nonlinear Rheology of a Nanoconfined Simple Fluid. *Phys. Rev. Lett.* **2010**, *104*, 218302.
- (32) Mukhopadhyay, A.; Bae, S. C.; Zhao, J.; Granick, S. How Confined Lubricants Diffuse During Shear. *Phys. Rev. Lett.* **2004**, *93*, 236105.
- (33) Li, T.-D.; Riedo, E. Nonlinear Viscoelastic Dynamics of Nanoconfined Wetting Liquids. *Phys. Rev. Lett.* **2008**, *100*, 106102.
- (34) Hu, H.; Carson, G. A.; Granick, S. Relaxation Time of Confined Liquids under Shear. *Phys. Rev. Lett.* **1991**, *66*, 2758–2761.
- (35) Demirel, A. L.; Granick, S. Glasslike Transition of a Confined Simple Fluid. *Phys. Rev. Lett.* **1996**, *77*, 2261–2264.
- (36) Sekhon, A.; Ajith, V. J.; Patil, S. The Effect of Boundary Slippage and Nonlinear Rheological Response on Flow of Nanoconfined Water. *J. Phys. Condens. Matter* **2017**, *29*, 205101.
- (37) Byron Bird, R.; Carreau, P. J. A Nonlinear Viscoelastic Model for Polymer Solutions and Melts—I. *Chem. Eng. Sci.* **1968**, *23*, 427–434.
- (38) Klein, J.; Kumacheva, E. Simple Liquids Confined to Molecularly Thin Layers. I. Confinement-Induced Liquid-to-Solid Phase Transitions. *J. Chem. Phys.* **1998**, *108*, 6996–7009.
- (39) Patil, S.; Matei, G.; Oral, A.; Hoffmann, P. M. Solid or Liquid? Solidification of a Nanoconfined Liquid under Nonequilibrium Conditions. *Langmuir* **2006**, *22*, 6485–6488.
- (40) Li, T.-D.; Gao, J.; Szoszkiewicz, R.; Landman, U.; Riedo, E. Structured and Viscous Water in Subnanometer Gaps. *Phys. Rev. B* **2007**, *75*, 115415.
- (41) Majumder, M.; Chopra, N.; Andrews, R.; Hinds, B. Enhanced Flow in Carbon Nanotubes. *Nature* **2005**, *438*, 44.
- (42) Secchi, E.; Marbach, S.; Niguès, A.; Stein, D.; Siria, A.; Bocquet, L. Massive Radius-Dependent Flow Slippage in Carbon Nanotubes. *Nature* **2016**, *537*, 210–213.
- (43) O’Shea, S. J.; Welland, M. E. Atomic Force Microscopy at Solid–Liquid Interfaces.

Langmuir **1998**, *14*, 4186–4197.

- (44) Khan, S. H.; Kramkowski, E. L.; Ochs, P. J.; Wilson, D. M.; Hoffmann, P. M. Viscosity of a Nanoconfined Liquid during Compression. *Appl. Phys. Lett.* **2014**, *104*, 023110.

Chapter 5

Finite Element Simulation of Force Sensor

5.1 Introduction

Scanning probe microscopy (SPM) has been widely used for measuring nanoscale properties in different areas of science. Local properties at the nanoscale are measured by probing the interaction forces; such as Van der waal's¹⁻³, electrostatic⁴, and DLVO forces^{5,6} between two surfaces. AFM is one of the SPM techniques⁷, where a cantilever with nanometre-sized tip is used as a probe of forces present between two surfaces – one is the tip itself, and the other one being the material under investigation. To detect surface forces which are usually in nN range, very soft and weak levers having a force constant of .01 - 10 nN/nm need to be employed. Due to their small stiffness constant, these cantilevers have a instability called snap into contact. To overcome these challenges, and as well as to perform measurements in a liquid environment, sensors should have high stiffness and high-quality factor. Günther for first time proposed the use of quartz tuning forks (QTF) as force sensor⁸⁻¹¹.

Despite having high stiffness (10^5 N/m), piezoelectric nature of quartz enables these tuning forks to have high force sensitivity in the nN-pN range¹². One key advantage of QTF is the reduction the overall instrument complexity due to its purely electrical readouts. Because of its wide use, different analytical models have been developed to study mechanical and electrical properties of QTFs. Finite Element Analysis (FEA) is one of the numerical techniques, widely used in sensor analysis and design as fast and efficient alternative to the pure analytical models^{13,14}. Finite element method (FEM) is a set of numerical methods¹⁵ that solve the general equation of motion required to understand the underlying physics of different systems in various areas, such as structural analysis, heat transfer analysis, fluid dynamics¹⁶⁻¹⁸, plasmonics¹⁹, and acoustics²⁰. However, the number of studies that investigated QTF theoretically with these numerical techniques are limited. In literature, FEM simulations have been employed to determine possible eigenmode²¹, stiffness constant^{22,23} of QTFs, and their application in various microscopies²³. While all of these

published works investigate on-resonance properties, no work has tried to understand the off-resonance response of QTF using FEM methods. In the present work, finite element analysis is performed to analyze the elastic and electrical response of our force sensor assembly at different off-resonance frequencies in the air and liquids. We hope that results of these simulations would help us to understand, and validate our measurement methodology developed to measure the shear response of liquids when confined between two surfaces at the nanoscale.

In this work, FEM simulations were employed to understand the dynamics of our tuning fork based force sensor in different surrounding mediums, such as; air, water and organic liquid (paraffin oil). In our experimental setup, the geometry of probe assembly consists of a fiber tip, attached to a tuning fork fixed on diether piezo^{24,25}. The tuning fork is mechanically excited by providing a controlled voltage across the diether piezo crystal, and an electrical signal is generated corresponding to the mechanical deflection. This current that is measured by connecting wires to tuning fork afterward was used to evaluate the oscillation amplitude of the prongs. In FEM simulation, this whole probe assembly was simulated using intrinsic mechanical and electrical properties of all the components. Frequency domain analysis was carried out to compute the response of our sensor in a different frequency regime. The response of the probe assembly is computed around resonance and off-resonance frequencies and, the oscillation amplitude of both the prongs was measured.

5.2 Theory

All FEM simulations were performed using Comsol Multiphysics Software Package. (COMSOL AB, Stockholm, Sweden). Two modules Comsol Multiphysics were employed; (i) Piezoelectric module, (ii) Acoustic- piezoelectric interaction. In the piezoelectric module, mechanical deflection in diether piezo and tuning fork was computed corresponding to the applied voltage signal, module. In acoustic piezoelectric interaction, the effect of damping medium such as water or other medium is sensed by measuring the changing in deflection of tuning fork relative to the free medium.

5.2.1 Piezoelectric module

The set of constitutive equations that were employed to relate the mechanical strains/stresses to electrical signal/field as shown below²⁶,

$$T = c_E S - e E \quad \text{-----} \quad (5.1)$$

$$D = e^T S + \epsilon_s E \quad \text{-----} \quad (5.2)$$

Where T is stress vector, D is electric flux density vector, S is strain tensor, E is electric field vector, c_E is the elasticity matrix, ϵ_s is permittivity and e is piezoelectric sensor matrix. FEM solves these set of equations to find the finite solution for the system. The finite element discretization is performed by establishing nodal solution variables and element shape function over an element domain which approximates the following solution²⁷,

$$u_c = N_u^T \cdot u \quad \text{-----} \quad (5.3)$$

$$V_c = N_V^T \cdot V \quad \text{-----} \quad (5.4)$$

where u_c is displacement within element domain in x,y,z directions, V_c is electric potential within the area, N_u is a matrix of displacement shape functions, N_V is the vector for the electrical potential shape function, u is a vector for nodal displacements, and V is the vector for nodal electrical potential. Using eqn (5.3) and (5.4) the strain S and electric field E are thus related to the displacements and potentials by eqn (5.5) and (5.6), respectively. Consider

$$S = B_u \cdot u \quad \text{-----} \quad (5.5)$$

$$E = -B_V \cdot V \quad \text{-----} \quad (5.6)$$

Where

$$B_u = \begin{bmatrix} \frac{d}{dx} & 0 & 0 & \frac{d}{dy} & 0 & \frac{d}{dz} \\ 0 & \frac{d}{dy} & 0 & \frac{d}{dx} & \frac{d}{dz} & 0 \\ 0 & 0 & \frac{d}{dz} & 0 & \frac{d}{dy} & \frac{d}{dx} \end{bmatrix}^T$$

$$B_V = \begin{bmatrix} \frac{d}{dx} & \frac{d}{dx} & \frac{d}{dx} \end{bmatrix}^T$$

By employing variational principle and the finite element discretization, the coupled finite element matrix equation is:

$$\begin{bmatrix} M & 0 \\ 0 & 0 \end{bmatrix} \begin{bmatrix} \ddot{u} \\ \ddot{V} \end{bmatrix} + \begin{bmatrix} C & 0 \\ 0 & 0 \end{bmatrix} \begin{bmatrix} \dot{u} \\ \dot{V} \end{bmatrix} + \begin{bmatrix} K & K_z \\ K_z^T & K_d \end{bmatrix} \begin{bmatrix} u \\ V \end{bmatrix} = \begin{bmatrix} F \\ L \end{bmatrix}$$

Where M is structural mass given by $M = \int \rho N_u N_u^T dv$, K is structural stiffness given by $K = \int u B_u B_u^T dv$, K_z is the piezoelectric coupling matrix given by $K_z = -\int e B_V B_u^T dv$, K_d

is the dielectric conductivity, given by $K_d = \int \epsilon B_V B_V^T dv$, C is structural damping matrix, ρ is the mass matrix, F is the structural load vector, L is the electrical load vector. The integration is over the whole element. These set of the equations were employed to measure the oscillation amplitude of any material which is piezoelectric.

Eigenfrequency and frequency domain analysis

For determining the fundamental mode of oscillation for force sensor eigenfrequency analysis were performed. After finding oscillation frequency of first fundament mode of oscillation, frequency domain analysis was performed to measure the response of force sensor around resonance frequency and below resonance frequency.

5.2.2 Acoustic-piezoelectric interaction module

In acoustic- piezoelectric interaction module, the effect of surrounding liquid medium was considered in addition to piezoelectric response. Like the previous case, eigenfrequency and frequency domain analysis were performed to understand the impact of viscous drag of surrounding liquid on the force sensor oscillation at resonance and below resonance frequency.

5.3 Results

5.3.1 Diether Piezo

Diether piezo made up of a PZT-5H piezoelectric material having dimensions 5 x 5 x 2 mm was simulated using the piezoelectric module. The material properties used for PZT-5H in the simulation are given in Table 5.1. Voltage was applied across its electrode to determine it's oscillation amplitude. To get an analytic solution, following boundary conditions were employed. (i) Voltage signal was applied to the upper surface of the piezo and bottom surface was grounded, (ii) initial velocity or displacement of whole geometry was set to zero at time $t=0$, (iii) the bottom surface of geometry was kept fixed, i.e., $x=0$ for $0 < t < \infty$ time. Frequency domain analysis was done to determine its oscillation amplitude by varying the frequency value from 5 kHz to 20 kHz. The plot of oscillation amplitude versus frequency for 1V applied across electrode is shown in Fig. 5.1. The inset shows one of oscillation modes of piezo.

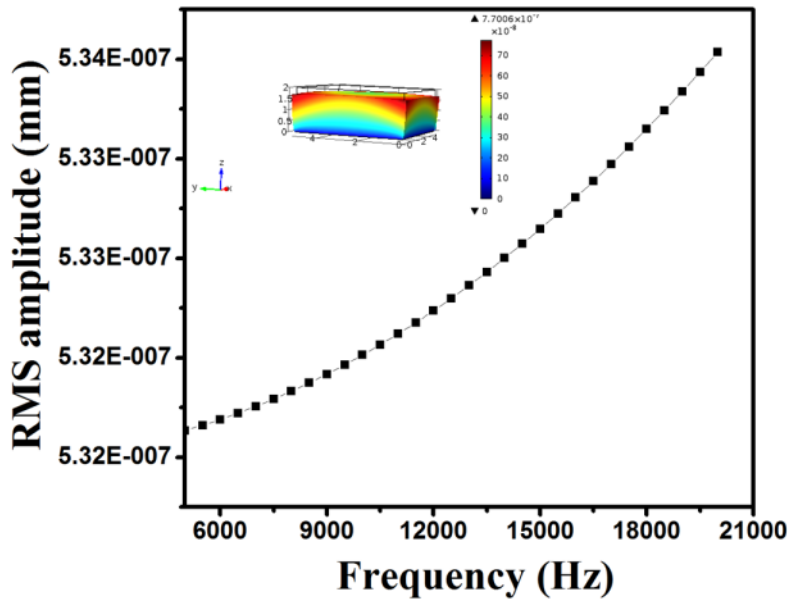


Fig. 5.1 Frequency response of diether piezo. Inset shows one of oscillation modes of diether piezo.

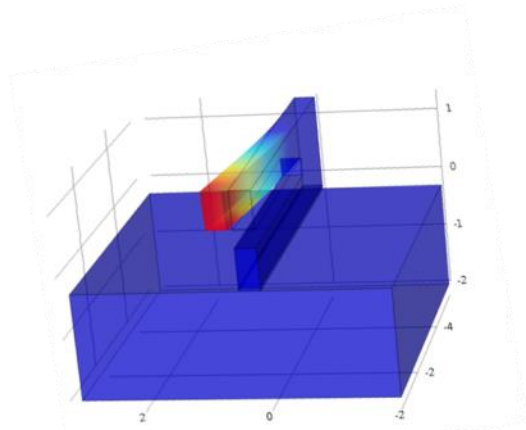
Oscillation amplitude was found to be $5 \text{ \AA}^0/\text{V}$ for simulated frequency range, and it agrees with oscillation amplitude measured experimentally using fiber-based interferometer²⁵.

5.3.2 Tuning fork with diether piezo

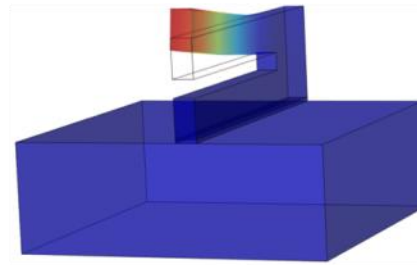
Further FEM simulations were performed for tuning fork with one prong fixed to diether piezo for mechanical excitation. The tuning fork is made up of a quartz material and piezoelectric in nature. It was fixed to a piezo by placing a thin layer of glue having thickness 0.3 mm. All the properties of quartz and glue material required for simulation are tabulated in Table 5.1 and 5.2. Tuning fork having the same dimension as in experimental setup was simulated. In this case, the piezoelectric module was employed. Similar boundary conditions were used as in case of simulation for diether piezo alone.

Eigenfrequency and frequency domain analysis was performed for this sensor assembly. Eigenfrequency analysis was done to determine all normal modes of oscillations. Frequency domain analysis was performed to assess oscillation amplitude of both prongs of tuning fork around first few fundamental resonance modes of oscillation (around 32 kHz) and below resonance frequency. To mechanically excite tuning fork voltage signal was applied across the electrode of piezo. The oscillation amplitude of both prongs of tuning fork around resonance frequency and below resonance frequency is measured. Eigenfrequency for fundamental mode agrees well with experimental eigenfrequency. Frequency domain analysis

was done to evaluate the oscillation amplitude of both prongs below resonance frequency and around resonance frequency. Fig 5.2 shows first two normal modes of oscillations around 17 kHz and 33 kHz.



Resonance Frequency = 17520 Hz



Resonance Frequency = 33757 Hz

Fig. 5.2 First two fundamental modes for tuning fork at 17 kHz and 33 kHz.

In frequency domain analysis, Fig. 5.3 shows the change in oscillation amplitude versus frequency for both prongs around first two fundamental frequency mode. We observe that for resonance mode at around 33.756 kHz, oscillation amplitude is 0.2 mm which is five orders of magnitude larger than that at about 17 kHz. The inset shows the frequency response of 2–12 kHz frequency range. It shows that oscillation amplitude of the free prong (red curve) is less in comparison to that of fixed prong (black curve).

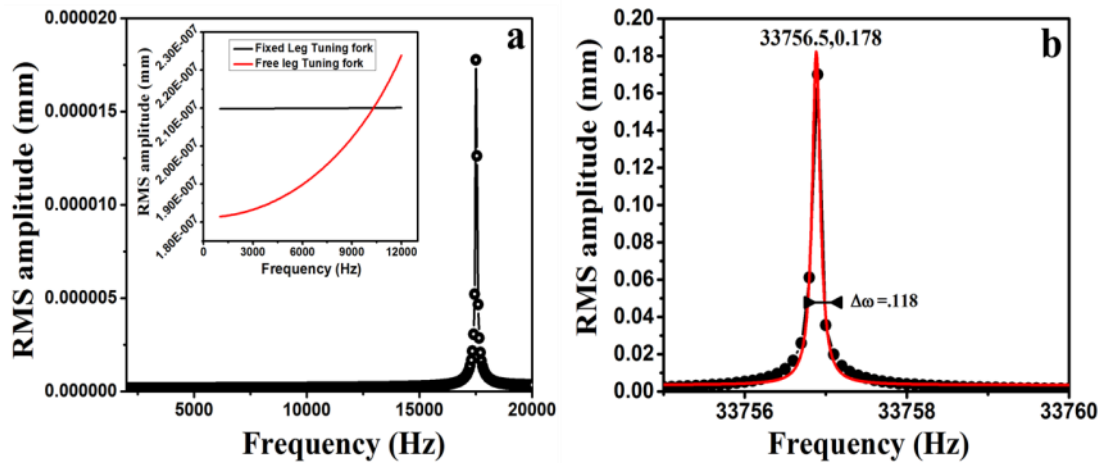


Fig. 5.3 (a) and (b) shows frequency response around first two fundamental modes of oscillation of tuning fork prong. Oscillation amplitude at 33 kHz is five orders of magnitude large than at 17 kHz. Inset shows frequency response for 2-12 kHz.

5.3.3 Optical fiber attached to tuning fork assembly

Next, the exact probe assembly (optical fiber tip attached to tuning fork) which was used in our experimental setup to perform shear measurement in a liquid environment was simulated. The piezoelectric module was employed to compute the effect of optical fiber on oscillation amplitude of prongs of the tuning form. The optical fiber made of silica glass, 3.5 mm in length, the radius of 65 μm , and tip diameter of 100 nm was fixed to tuning fork free prong by placing the thin layer of glue in between. All materials used in probe assembly and their properties are stated in Table 5.1 and 5.2.

In this case, glue as linear viscoelastic material, silica fiber as linear elastic material and remaining components as the piezoelectric element were used. Similar boundary conditions as employed in the previous case were used. Voltage was applied across the electrode of piezo and mechanical deflection in prongs of the tuning fork is measured. Eigenfrequency and frequency domain analysis was performed. Fig 5.4 is a pictorial representation of Fundamental oscillation mode around 36 kHz. Fig 5.5 shows displacement versus frequency around second fundamental mode with and without optical fiber.

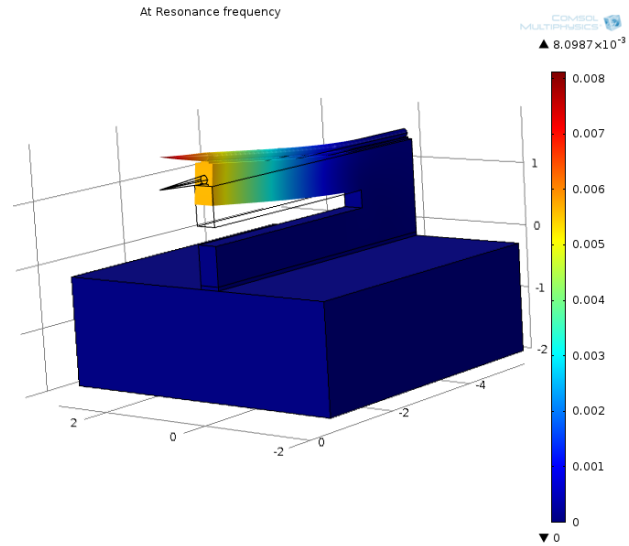


Fig. 5.4 Pictorial representation of second fundamental mode at 36 kHz.

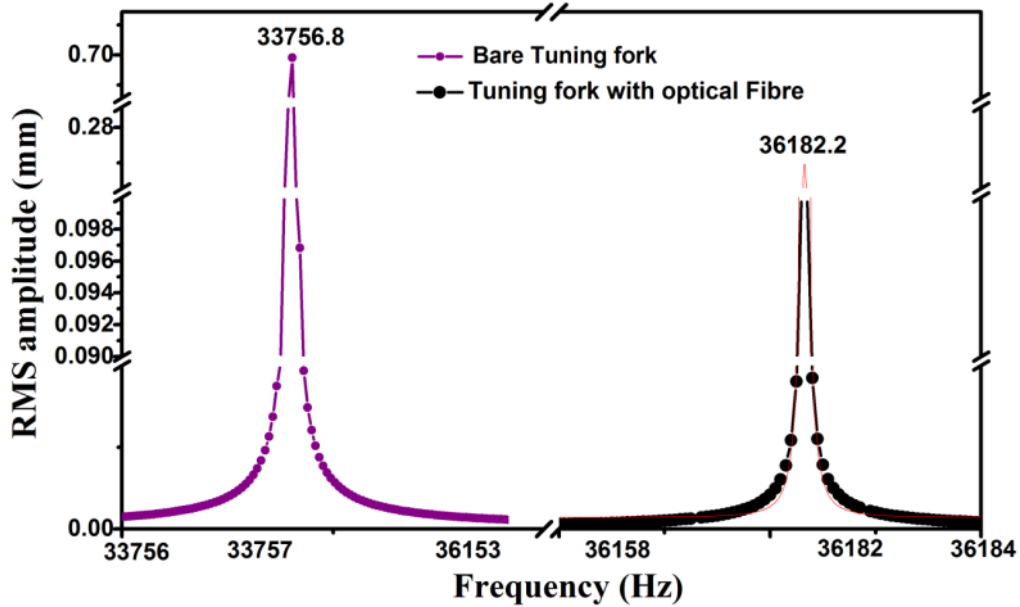


Fig. 5.5 Frequency response of tuning fork with and without fiber tip around their second fundamental mode.

We found that after attaching the fiber tip to tuning fork assembly, there is a shift in resonance frequency toward a higher value. This result agrees well with our experimental observation. The possible factors which result in a change of resonance frequency towards higher frequency are discussed in detail below. Attachment of fiber tip to tuning fork can effect in two ways; (i) mass loading (ii) the stiffness enhancement. Mass loading effect

results in a decrease in resonance frequency in comparison to only tuning fork resonance frequency. Stiffness enhancement takes place due to thickening of force sensor which results in increase in resonance frequency. The shift of resonance frequency to higher frequency in our experiment suggests the second reason of thickening the force sensor rather than mass loading.

Off-resonance frequency response was also simulated. It is found that the oscillation amplitude of the prong attached to fiber tip is oscillating with a smaller amplitude than the free leg for a range of frequencies. Fig. 5.6 shows the off-resonance frequency response of probe assembly with an optical fiber connected to tuning fork assembly.

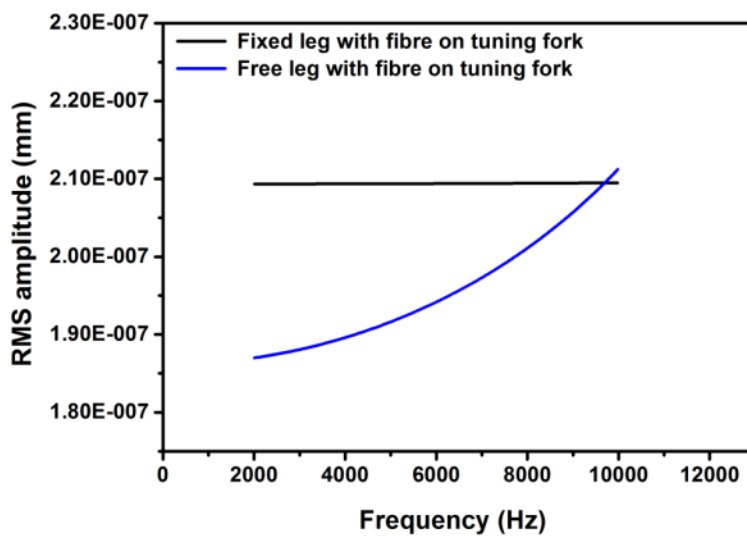


Fig. 5.6 Off-resonance frequency response of both prongs of tuning fork.

5.3.4 Simulation of a probe assembly in liquid

Acoustic structure interaction module was employed to understand the effect of surrounding fluid on the dynamics of the force sensor, that will be oscillating in a liquid medium in a real experiment. In another aspect, this simulation is also helpful in providing information about the viscous drag of liquid and understand the change in current signal taking place during the experiment as fiber tip is dipping into liquid.

In Acoustic structure interaction module, acoustic piezoelectric structure interaction was employed as sensor assembly is piezoelectric. The properties of liquid used for simulation are listed Table 5.3. Eigenfrequency and frequency domain analysis was carried out as before. Boundary conditions such as sound wall hard boundary were designated, structure sound

interaction boundary and other boundary condition were same that employed in the piezoelectric module.

During eigenfrequency analysis, the shift in resonance frequency of sensor assembly to lower frequency value was found in the liquid medium. It signifies the effect of viscous drag of liquid on force sensor. Frequency domain analysis was performed to measure the change in oscillation amplitude of tuning fork (sensor) prongs with frequency value around fundamental frequency mode. Frequency analysis was done for two liquids such as water and paraffin oil. Fig. 5.7 shows resonance tuning curve of the force sensor with its comparison in an air medium. The simulation results regarding the shift in resonance frequency agree well (up to 80%) with our experiment.

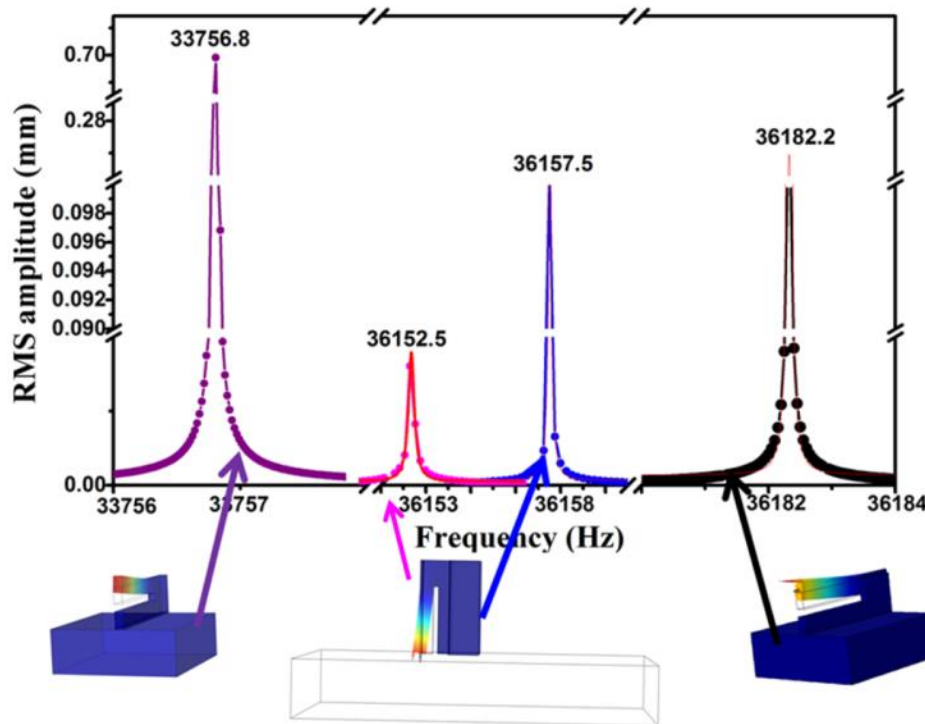


Fig. 5.7 Frequency response of force sensor in liquid medium with its comparison in air and force sensor without fiber tip.

The off-resonance frequency of force sensor was measured in water. It is already observed that at a frequency below resonance the free prong of the tuning fork oscillates with lower amplitude in comparison to the fixed prong. From the simulation result in a liquid medium, it was found out that the oscillation amplitude of the free prong decreases further due to viscous drag of water. This decrease in oscillation amplitude to a lower value, in turn, gives rise to a

more substantial differential amplitude than the case when the whole assembly is in the air (Fig. 5.8). The current flowing through tuning fork is proportional to this differential amplitude of both prongs. Our simulation shows that, at off-resonance frequencies, while going from air to liquid medium there should be an increase in the current signal – a fact in complete agreement with our experimental observation. Thus, these set of results obtained from FEM simulations directly help us to understand our measurement methodology and experimental results on the viscous drag of confined liquids.

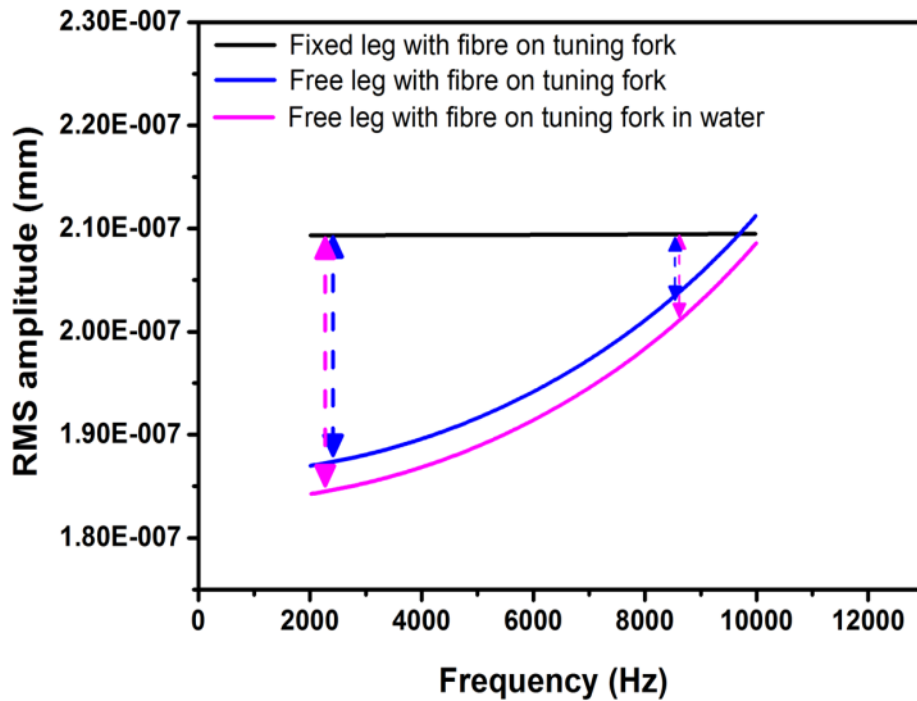


Fig. 5.8 Off- Resonance response of force sensor in the air and a liquid medium.

Table 5.1 Properties of piezoelectric materials

Material	Elasticity matrix (Pa)	Coupling matrix (C/m ²)	Relative permittivity (ϵ_{rs})	Density (ρ , Kg/m ³)
PZT 5H	$\begin{pmatrix} 12.720 & 8.021 & 8.467 & 0 & 0 & 0 \\ 8.021 & 12.720 & 8.467 & 0 & 0 & 0 \\ 8.467 & 8.467 & 11.743 & 0 & 0 & 0 \\ 0 & 0 & 0 & 2.298 & 0 & 0 \\ 0 & 0 & 0 & 0 & 2.298 & 0 \\ 0 & 0 & 0 & 0 & 0 & 2.347 \end{pmatrix}$	$\begin{pmatrix} 0 & 0 & 0 & 0 & 17.0345 & 0 \\ 0 & 0 & 0 & 17.0345 & 0 & 0 \\ -6.622 & -6.622 & 23.240 & 0 & 0 & 0 \end{pmatrix}$	$\begin{pmatrix} 1704.4 & 0 & 0 \\ 0 & 1704.4 & 0 \\ 0 & 0 & 81433.6 \end{pmatrix}$	7500
Quartz	$\begin{pmatrix} 8.673 & .698 & 8.467 & 0 & 0 & 0 \\ 0.698 & & 8.467 & 0 & 0 & 0 \\ 8.673 & -1.790 & 0 & 0 & 0 & 0 \\ 1.191 & 0 & 0 & 0 & 0 & 0 \\ 1.191 & & 0 & 0 & 0 & 1.792 \\ 10.71 & 0 & 5.794 & 0 & 0 & 3.990 \end{pmatrix}$	$\begin{pmatrix} -0.1954 & 0.1954 & 0 & 0.12120 & 0 & 0 \\ 0 & 0 & 0 & 0 & 0.12127 & 0.195 \\ 0 & 0 & 0 & 0 & 0 & 0 \end{pmatrix}$	$\begin{pmatrix} 4.4093 & 0 & 0 \\ 0 & 4.4092 & 0 \\ 0 & 0 & 4.680 \end{pmatrix}$	2651

Table 5.2 Properties of non-piezoelectric material

Material	Density (Kg/m ³)	Young Modulus (GPa)	Poisson Ratio
Silica glass	2203	73.1	0.17
Glue	1700	5	0.4

Table 5.3 Properties of liquid

Material	Density (Kg/m ³)	Dynamic Viscosity (PaS)	Speed of Sound	Bulk viscosity
Water	1225	1e-3	1450	1e-2
Oil	1200	.055	2500	0.55

5.4 Conclusion

In this work, FEM simulations were employed to understand the dynamics of the whole force sensor assembly in the air, water, and paraffin oil. In these simulations, eigenfrequency and frequency domain analysis was performed. These simulations help us to probe the fundamental mode of the frequency of tuning fork and to measure the change in oscillation

amplitude around resonance and off-resonance frequencies. We have examined the change in oscillation amplitude of our sensor with the different surrounding medium. These results are in good agreement with our experimental observations and provide information to understand the sensor assembly in more detail. FEM simulations directly support our measurement methodology that was developed to measure viscous drag of liquids when confined between the tip and mica.

References

- (1) London, F. The General Theory of Molecular Forces. *Trans. Faraday Soc.* **1937**, *33*, 8b.
- (2) Israelachvili, J. N. Van Der Waals Dispersion Force Contribution to Works of Adhesion and Contact Angles on the Basis of Macroscopic Theory. *J. Chem. Soc. Faraday Trans. 2* **1973**, *69*, 1729.
- (3) Spalding, D. B. The Molecular Theory of Gases and Liquids. J. O. Hirschfelder, C. F. Curtiss and R. B. Bird. John Wiley, New York. Chapman & Hall, London, 1954. 1,219 Pp. Diagrams. 160s. *J. R. Aeronaut. Soc.* **1955**, *59*, 228.
- (4) Israelachvili, J. N. Van Der Waals Forces. In *Intermolecular and Surface Forces*; Elsevier, 2011; pp 107–132.
- (5) Derjaguin, B.; Landau, L. Theory of the Stability of Strongly Charged Lyophobic Sols and of the Adhesion of Strongly Charged Particles in Solutions of Electrolytes. *Prog. Surf. Sci.* **1993**, *43*, 30–59.
- (6) Verwey, E. J. W. Theory of the Stability of Lyophobic Colloids. *J. Phys. Colloid Chem.* **1947**, *51*, 631–636.
- (7) Binnig, G.; Quate, C. F.; Gerber, C. Atomic Force Microscope. *Phys. Rev. Lett.* **1986**, *56*, 930–933.
- (8) Gunther, P.; Fischer, U. C.; Dransfeld, K. Scanning Near-Field Acoustic Microscopy. *Appl. Phys. B Photophysics Laser Chem.* **1989**, *48*, 89–92.
- (9) Karrai, K.; Grober, R. D. Piezoelectric Tip- sample Distance Control for near Field Optical Microscopes. *Appl. Phys. Lett.* **1995**, *66*, 1842–1844.

- (10) Ruiter, A. G. T.; Veerman, J. A.; Van Der Werf, K. O.; Van Hulst, N. F. Dynamic Behavior of Tuning Fork Shear-Force Feedback. *Appl. Phys. Lett.* **1997**, *71*, 28–30.
- (11) Atia, W. A.; Davis, C. C. A Phase-Locked Shear-Force Microscope for Distance Regulation in near-Field Optical Microscopy. *Appl. Phys. Lett.* **1997**, *70*, 405–407.
- (12) Giessibl, F. J. Atomic Resolution on Si(111)-(7×7) by Noncontact Atomic Force Microscopy with a Force Sensor Based on a Quartz Tuning Fork. *Appl. Phys. Lett.* **2000**, *76*, 1470–1472.
- (13) Ansari, M. Z.; Cho, C. Deflection, Frequency, and Stress Characteristics of Rectangular, Triangular, and Step Profile Microcantilevers for Biosensors. *Sensors* **2009**, *9*, 6046–6057.
- (14) Ma, C.-C.; Huang, Y.-H.; Pan, S.-Y. Investigation of the Transient Behavior of a Cantilever Beam Using PVDF Sensors. *Sensors* **2012**, *12*, 2088–2117.
- (15) Courant, R. Variational Methods for the Solution of Problems of Equilibrium and Vibrations. *Bull. Am. Math. Soc.* **1943**, *49*, 1–24.
- (16) Everstine, G. C. A Symmetric Potential Formulation for Fluid-Structure Interaction. *J. Sound Vib.* **1981**, *79*, 157–160.
- (17) Shen, S. Finite-Element Methods in Fluid Mechanics. **1977**.
- (18) Acharya, S. Analysis and FEM Simulation of Flow of Fluids in Pipes Fluid Flow COMSOL Analysis. **2016**.
- (19) Burger, S.; Zschiedrich, L.; Pomplun, J.; Schmidt, F. Finite Element Method for Accurate 3D Simulation of Plasmonic Waveguides. **2010**, *7604*, 1–8.
- (20) Eccardt, P.; Landes, H.; Lerch, R. Finite Element Simulation of Acoustic Wave Propagation within Flowing Media. *IEEE Ultrason. Symp.* **1996**, 991–994.
- (21) Kim, B.; Jahng, J.; Khan, R. M.; Park, S.; Potma, E. O. Eigenmodes of a Quartz Tuning Fork and Their Application to Photoinduced Force Microscopy. *Phys. Rev. B* **2017**, *95*, 075440.
- (22) González, L.; Oria, R.; Botaya, L.; Puig-Vidal, M.; Otero, J. Determination of the Static Spring Constant of Electrically-Driven Quartz Tuning Forks with Two Freely

- Oscillating Prongs. *Nanotechnology* **2015**, 26, 055501.
- (23) Falter, J.; Stiefermann, M.; Langewisch, G.; Schurig, P.; Hölscher, H.; Fuchs, H.; Schirmeisen, A. Calibration of Quartz Tuning Fork Spring Constants for Non-Contact Atomic Force Microscopy: Direct Mechanical Measurements and Simulations. *Beilstein J. Nanotechnol.* **2014**, 5, 507–516.
- (24) Kapoor, K.; Kanawade, V.; Shukla, V.; Patil, S. A New Tuning Fork-Based Instrument for Oscillatory Shear Rheology of Nano-Confined Liquids. *Rev. Sci. Instrum.* **2013**, 84, 025101.
- (25) Sekhon, A.; Ajith, V. J.; Patil, S. The Effect of Boundary Slippage and Nonlinear Rheological Response on Flow of Nanoconfined Water. *J. Phys. Condens. Matter* **2017**, 29, 205101.
- (26) Ballato, A. Basic Material Quartz and Related Innovations. *Piezoelectricity* **1880**, 9–35.
- (27) Nechibvute, A.; Chawanda, A.; Luhanga, P. Finite Element Modeling of a Piezoelectric Composite Beam and Comparative Performance Study of Piezoelectric Materials for Voltage Generation. *ISRN Mater. Sci.* **2012**, 2012, 1–11.

Chapter 6

Conclusions and Future Perspective

6.1 Conclusions

This thesis aims to measure the shear response of nanoconfined liquids at high shear rates. In our lab, we have built a tuning fork based shear Rheometer and performed off-resonance measurements with high shear frequency (5-20 kHz) and shear rates ($10^4 - 10^6 \text{ s}^{-1}$).

In this thesis, I have tried to differentiate the effect of confinement and wettability of the confining surfaces on dynamic response exhibited by nanoconfined liquid. First, we measured the shear response of water confined between the fiber tip and mica substrate. We observed a decrease in dissipation coefficient at separations between substrates to be less than 10 nm. We attribute this behavior to following possible reasons; i) violation of no-slip boundary condition (boundary slippage), ii) shear thinning (shear rate dependent viscosity), and iii) combined effect of shear thinning and slippage. We observe that our experimental data was best fitted by a combination of both shear thinning and finite slippage. Afterward, to understand the effect of slippage, we have measured the shear response of water on five substrates with variable wettability. We found reduction in dissipation on all substrates having lower ($50^\circ < \theta < 85^\circ$), intermediate ($\theta \approx 40^\circ$) and higher ($\theta < 5^\circ$) wettability. We have been able to explain this reduction in dissipation on all substrates was with shear thinning including finite slip length. We have found that the slip length increases with increase in contact angle, *i.e.*, with a decrease in substrate wettability. We see a considerable decrease in relaxation time, indicating slow-down in molecular dynamics under confinement as compared to bulk. However, no appreciable change in relaxation time was observed with increase in contact angles. Together, these findings enable us to single out the effect of confinement and substrate wettability on the non-rheological response of water at nanoconfinement.

Following this, we have tried to understand the difference in dynamic shear-response of polar and non-polar liquids. We have taken two organic non-polar liquids; OMCTS and TEHOS, which are globular in shape and act as a model system for oil molecules. We have chosen these two liquids having different contact angle on the mica substrate, to take into

account the effect of substrate wettability. We have observed a decrease in dissipation coefficient for both the non-polar liquids. Once again we could account the reduction in dissipation by the combined effect of shear thinning and slippage. We have observed that slip length increases with increase in contact angle on mica. Additionally, we also found out slowing down of dynamics (increase in relaxation time) for OMCTS and TEHOS at nanoconfinement in comparison to bulk value. This increase is also one order of magnitude more than that for water at nanoconfinement. We attribute this observation due to difference in nature of liquids at bulk, as OMCTS and TEHOS is more viscous in nature at bulk in comparison to water.. We also observe that decrease in dissipation coefficient for non-polar liquids (OMCTS and TEHOS) was 7-8 % it was same shown by polar liquid (water).

From these results, we conclude that, if the shear rates are larger than the inverse of relaxation time of nanoconfined liquid, nanoconfined liquids will undergo non-Newtonian response irrespective of their chemical nature. We would like to comment that, in most of the published studies, the non-Newtonian response is not observed for both polar (water) and non polar liquids (OMCTS, TEHOS), as the dynamic response of both liquids is measured at shear frequencies < 200 Hz and $< 1-2$ kHz by using SFA and AFM respectively (Fig. 6.1). These shear rates are not large enough to capture the non-Newtonian response of the confined water.

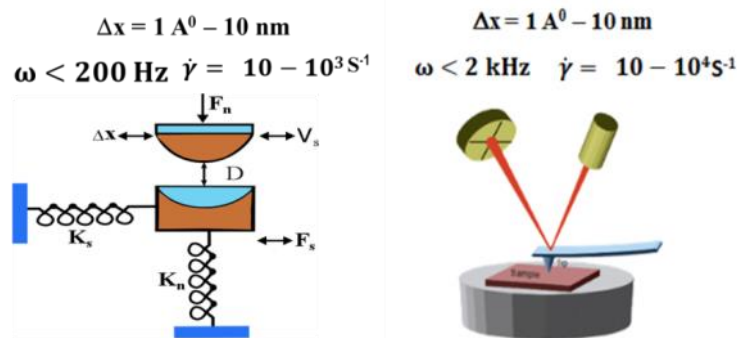


Fig. 6.1 Possible range of attainable shear frequencies and shear rates SFA (on the left) and AFM (on the right)

Beside this thesis, we present the future perspective of this work in the following section.

6.2 Future Outlook

In this thesis, the mechanical response of nano-confined liquid was measured using a home-built dynamic shear-rheometer. To get a direct understanding of the processes, which are

responsible for showing non-Newtonian behavior for nanoconfined fluid at the nanoscale, the system needs to be probed optically along with mechanical measurement. There are various possible ways to implement optical access by integrating mechanical analysis with (i) Fluorescence correlation spectroscopy, to measure the diffusion coefficient of probe molecules immersed in a liquid of interest at nano-confinement, and (ii) Raman spectroscopy, to probe the structural changes taking place at a molecular level giving rise to non-Newtonian behavior.

6.2.1 Integration with Fluorescence correlation spectroscopy

Fluorescence Correlation Spectroscopy (FCS) is a non-invasive optical technique to measure the diffusion coefficient based on fluorescence fluctuations of solute molecules in a small volume under equilibrium conditions. In FCS measurements, the fluorescence fluctuations can be measured by using dilute concentrations (nanomolar-picomolar) of the sample and using small detection volumes (femtolitre). The autocorrelation function of fluorescence fluctuations carries information about dynamics of the system at different time scales. Therefore, by choosing the appropriate model solute, different dynamics can be probed by its measuring characteristic timescales. Integration of mechanical shear-measurement with FCS spectroscopy is currently under development in our lab. In this setup, a laser beam of a particular wavelength is passed through the optical fibre to excite the probe molecules, which are fluorescent, and present in detection volume. Fluorescence emission signal can be collected by APD and correlated afterward to measure diffusion coefficient of the solutes when present in the confined liquid.

6.2.2 Integration with Raman spectroscopy

Raman spectroscopy is a light scattering technique, discovered by Sir CV Raman and KS Krishnan in liquid¹⁻³ and by GS Landsberg and LI Mandelstam in crystal⁴⁻⁶ that probes the vibrational energy levels of molecules in the ground and excited electronic state. For a molecule to exhibit a Raman Effect, there must be a change in its electric dipole polarizability on excitation. Energy level diagram showing the states involved in Raman spectra is shown in Fig. 6.2. Vibrational frequencies are a measure of the strength of different chemical bonds of the molecule, and thus can determine small changes in molecular structure. To get more information about confined liquid at the molecular level, the laser beam could be passed through fiber tip to excite the molecule and to record the vibrational signature of molecules in a confined liquid. A major challenge of integrating Raman spectrometer with shear force

measurement will be to get enough Raman scattered photons for an acceptable signal to noise in the obtained spectrum.

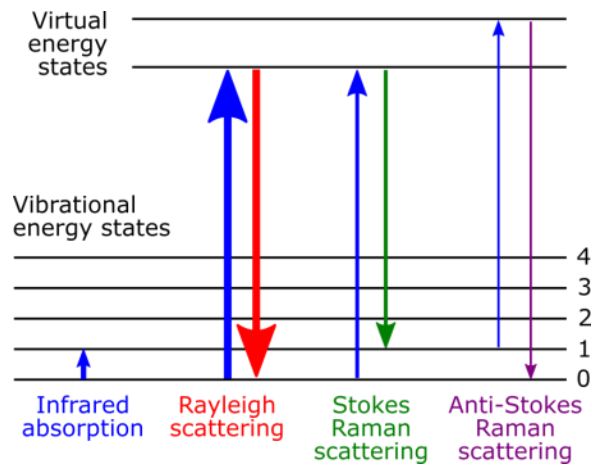


Fig. 6.2 Energy level diagram showing the states involved in Raman process

References

- (1) Raman, C. V. A Change of Wave-Length in Light Scattering. *Nature* **1928**, *121*, 619–619.
- (2) Raman, C. V. A New Radiation. *Proc. Indian Acad. Sci. - Sect. A* **1953**, *37*, 333–341.
- (3) V., R. C.; Krishnan, K. S. A New Type of Secondary Radiation. *Nature* **1928**, *121*, 501–502.
- (4) Landsberg, G. S.; Mandelstam, L. I. Eine Neue Erscheinung Bei Der Lichtzerstreuung in Krystallen. *Naturwissenschaften* **1928**, *16*, 557–558.
- (5) Landsberg, G. S.; Mandelstam, L. I. New Phenomenon in Scattering of Light (Preliminary Report). *J. Russ. Physico-Chemical Soc. Phys. Sect.* **1928**, *60*, 335.
- (6) Mandelstam, L. I.; Landsberg, G. S.; Leontowitsch, M. Über Die Theorie Der Molekularen Lichtzerstreuung in Kristallen (Klassische Theorie). *Zeitschrift fur Phys.* **1930**, *60*, 334–344.

